NATIONAL TECHNICAL UNIVERSITY
OF ATHENS
SCHOOL OF APPLIED MATHEMATICAL
AND PHYSICAL SCIENCE

INSTITUTE OF NANOSCIENCE AND NANOTECHNOLOGY
NCSR "DEMOKRITOS"

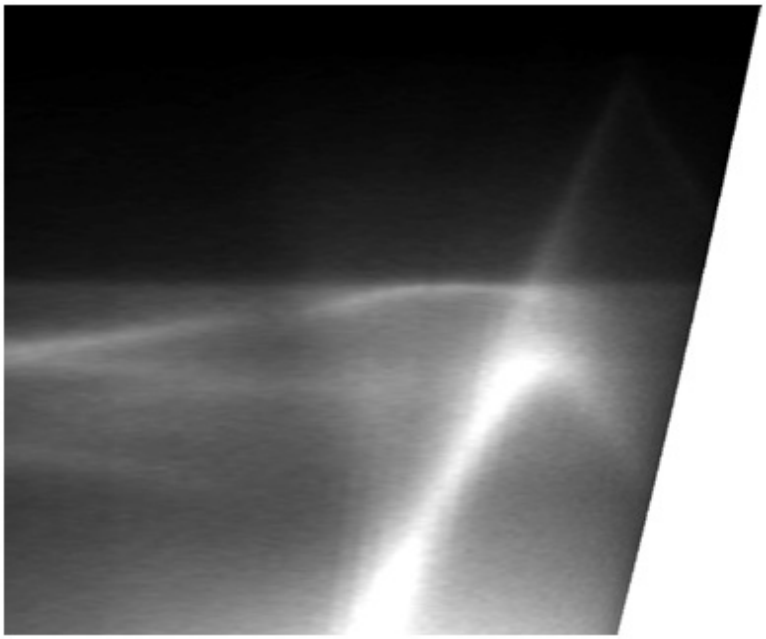

José Márquez Velasco

« Growth of Graphene and Combination with Dielectric Materials for New Electronic Devices »

DOCTORAL DISSERTATION

ATHENS JULY 2016

ΕΘΝΙΚΟ ΜΕΤΣΟΒΙΟ ΠΟΛΥΤΕΧΝΕΙΟ
ΣΧΟΛΗ ΕΦΑΡΜΟΣΜΕΝΩΝ ΜΑΘΗΜΑΤΙΚΩΝ
ΚΑΙ ΦΥΣΙΚΩΝ ΕΠΙΣΤΗΜΩΝ

«Ανάπτυξη Γραφενίου και Συνδυασμός με Διηλεκτρικά Υλικά για Νέες Ηλεκτρονικές Διατάξεις»

ΔΙΔΑΚΤΟΡΙΚΗ ΔΙΑΤΡΙΒΗ

JOSE MARQUEZ VELASCO

Διπλωματούχου Φυσικού
Σχολής Φυσικής
Πανεπιστημίου της Σεβίλλης

Ιούλιος, 2016

ΕΘΝΙΚΟ ΜΕΤΣΟΒΙΟ ΠΟΛΥΤΕΧΝΕΙΟ
ΣΧΟΛΗ ΕΦΑΡΜΟΣΜΕΝΩΝ ΜΑΘΗΜΑΤΙΚΩΝ
ΚΑΙ ΦΥΣΙΚΩΝ ΕΠΙΣΤΗΜΩΝ

«Ανάπτυξη Γραφενίου και Συνδυασμός με Διηλεκτρικά Υλικά για Νέες Ηλεκτρονικές Διατάξεις»

ΔΙΔΑΚΤΟΡΙΚΗ ΔΙΑΤΡΙΒΗ

JOSE MARQUEZ VELASCO

Διπλωματούχου Φυσικού
Σχολής Φυσικής
Πανεπιστημίου της Σεβίλλης

ΤΡΙΜΕΛΗΣ ΣΥΜΒΟΥΛΕΥΤΙΚΗ ΕΠΙΤΡΟΠΗ:
1. Α. Δημουλάς, Διευθ. Ερευνών ΕΚΕΦΕ (Επιβλέπων)
2. Ι. Ράπτης, Καθ. ΕΜΠ
3. Λ. Τσέτσερης, Καθ. ΕΠΜ

ΕΠΤΑΜΕΛΗΣ ΣΥΜΒΟΥΛΕΥΤΙΚΗ ΕΠΙΤΡΟΠΗ:
1. Ι. Α. Δημουλάς, Διευθ. Ερευνών ΕΚΕΦΕ (Επιβλέπων)
2. Ι. Ράπτης, Καθ. ΕΜΠ
3. Λ. Τσέτσερης, Καθ. ΕΠΜ
4. Δ. Τσουκαλά, Καθ. ΕΠΜ
5. Γ. Βαρελογιάννη, Καθ. ΕΠΜ
6. Ν. Μπούκο, Διευθ. Ερευνών ΕΚΕΦΕ
7. Ε. Ευαγγέλου, Καθ. ΠΙ

Αθήνα, Ιούλιος 2016

To my parents, José and Domi.

Caminante, son tus huellas
el camino y nada más;
Caminante, no hay camino,
se hace camino al andar.

Caminante, A. Machado

Κι αν πτωχική την βρεις, η Ιθάκη δεν σε γέλασε.
Έτσι σοφός που έγινες, με τόση πείρα,
ήδη θα το κατάλαβες η Ιθάκες τι σημαίνουν.

Ιθάκη, Κ.Π. Καβάφης

Acknowledgments

Firstly, I would like to express my sincere gratitude to my supervisor Dr. A. Dimoulas, research director and head of the MBE laboratory and Surface Analysis laboratory at the Institute of Nanoscience and Nanotechnology of the National Center for Scientific Research “Demokritos” for giving me the opportunity to work as a PhD student in his team and for his continuous support regarding my PhD study and all the related research throughout the four years of our collaboration.

I would also like to thank my co-supervisors, Prof. Y.S. Raptis and Prof. L. Tsetseris of the School of Applied Mathematics and Physics of the National Technical University of Athens. I specifically like to thank Prof. Y.S. Raptis for his guidance considering Raman spectroscopy but most of all for his interesting comments, encouragement and invaluable help. Special acknowledgements are also ought to Prof. L. Tsetseris for helping me with the first-principles calculations and for his patience, precious advices and help.

My sincere thanks also go to Prof. G. Kordas, who provided me the access to his laboratory and Raman equipment. Additionally, I am grateful to all my collaborators including Dr. P. Falaras, Dr. N. Boukos, Dr. A. Speliotis, Dr. G. Pilatos, Prof. E.K. Evangelou and Dr. V. Likodimos.

I would also like to thank my office mate, PhD fellow and friend S.A. Giamini for his invaluable support and help, Dr. P. Tsipas for his help, thoughtful advices and the improvement of my greek vocabulary and Dr. N. Kelaidis for his useful support and memorable jokes. I also own many thanks to my colleagues Dr. D. Tsoutsou, Dr. E. Xenogiannopoulou, K. Aretouli, and our students E.Vassalou, A. Kordatos and D. Manousou for their contribution to a nice work environment and their support . Sincerely, thanks to all of you for your help and our good moments. Many thanks should also go to D. Kaltsas, for his precious help during this thesis. I would also like to express my gratitude to the former members of the team, Dr. S. Kassavetis, the famous one and great captain of our football team, now at the Aristotle University of Thessaloniki. Specially thanks to Dr. E Golias, for his infinite help, patience, invaluable support and improvement of my general greek culture, now at the Helmholtz-Zentrum Berlin (BESSY II).

Finally, I would like to thank my family and friends, both in Greece and my country Spain. To Alexadra, my soul mate and my beloved partner, for her unconditional continuous support, help and infinite patience in everyday, and of course for her invaluable help during the writing of this dissertation. To my parents for raising me up, supporting me and trusting me in whatever I decided to do. To my sister for being there since my childhood, her husband and my lovely nieces. To Alexandra's parents, brother and family for taking me as one more of their owns and making me feel at home. To my friend Armando, for being a great man, for his help and support despite the great geographical distance between us. To Orestis, my friend, for his support, beers, cooking and great moments that we shared throughout all this time.

Abstract

Graphene is a two-dimensional material with very promising prospects for applications on electronic devices of new generation. In this work we have optimized the process to grow single layer graphene on copper substrates by chemical vapor deposition. Large areas of single layer graphene with low defect densities were certified by Raman spectroscopy.

Although Raman spectroscopy is widely used to study the number of graphene layers when the layers are AB stacked, the method has limitations when it deals with other stacking orders. We demonstrated that ARPES measurements can be used to determine the number of layers of non-AB stacked graphene grown on single crystal Cu(111). Thus, we found that we had three rotated graphene layers with a relative angle of ~4° between them.

Another approximation to the single layer graphene was tried. From a sample with AB stacked multi-layer graphene, the number of layers were reduced by etching the sample at hydrogen atmosphere while using mild temperatures during the annealing. However, we did not achieve our principal goal to reduce the sample to single layer graphene. Instead we managed to reduce the sample to AB-stacked few-layers graphene, which is also interesting since it is not easy to grow large areas of AB stacked few-layers graphene by chemical vapor deposition. It is worth mentioning that the process did not introduce noticeable defects on the lattice. The whole process was certified by Raman spectroscopy and XPS.

We achieved to encapsulate graphene in MIS device gates. The transfer method was optimized, as well as the Al_2O_3 deposition, to avoid graphene defects. C-V curves were measured on capacitors with and without graphene embed in order to analyze the effect of graphene in the structure. The results show a large enhancement of the total capacitance of up to 35% in the accumulation, above the geometrical capacitance. This was related to the negative quantum capacitance contribution of graphene by a theoretical model of the device.

Finally, the stability of graphene on different two-dimensional substrates such as h-AlN/Ag111, h-BN/Ni111, $HfSe_2$/Ni111 and $MoSe_2$/$TaSe_2$ was studied by density functional theory. Also, the study of the electronic properties of the structures mentioned before shows that dielectrics with a larger band gap (h-AlN, h-BN and $MoSe_2$) do not affect the electronic properties of graphene while the dielectric with smaller band gap ($HfSe_2$) clearly affect the graphene LDOS. From the point of view of metals, it is shown that Ag(111) alters more significantly the LDOS of graphene than Ni(111) or $TaSe_2$. Additionally, DFT method was used to analyze ARPES measurements of different two-dimensional transition metal dichalcogenides such as $TaSe_2$, $ZrSe_2$ and $HfSe_2$.

Περίληψη

Το γραφένιο είναι ένα δισδιάστατο υλικό με πολλά υποσχόμενες προοπτικές για εφαρμογές σε ηλεκτρονικές διατάξεις νέας γενιάς. Στο πλαίσιο αυτής της διδακτορικής διατριβής, βελτιστοποιήθηκε η διαδικασία ανάπτυξης μονοατομικού στρώματος γραφενίου σε υποστρώματα χαλκού, μέσω της μεθόδου Χημικής Εναπόθεσης από Φάση Ατμών (Chemical Vapor Deposition, CVD). Για τον έλεγχο των αποτελεσμάτων, μεγάλες επιφάνειες μονοατομικού γραφενίου με μικρή πυκνότητα ατελειών χαρακτηρίστηκαν μέσω της φασματοσκοπίας Raman.

Παρά το γεγονός ότι η φασματοσκοπία Raman χρησιμοποιείται ευρέως για την ανίχνευση του αριθμού των στρωμάτων AB stacked γραφενίου, η μέθεοδος δεν είναι επαρκής όταν χρησιμοποιείται σε άλλες στρωματικές δομές. Ως απάντηση σε αυτό το πρόβλημα, αποδείχτηκε ότι η μέθοδος ARPES μπορεί να χρησιμοποιηθεί για να προσδιοριστεί ο αριθμός των στρωμάτων του Non-AB stacked γραφενίου επί μονοκρυσταλλικου Cu(111). Το συμπέρασμα είναι ότι αυτές οι δομές αποτελούνται από τρία στρώματα γραφενίου, περιστραμμένα μεταξύ τους, ανά δύο, κατά ~4°.

Επιχειρήθηκε επιπλέον μία ακόμα προσέγγιση για την ανάπτυξη μονοατομικού στρώματος γραφενίου. Από ένα δείγμα AB stacked πολυστρωματικού γραφενίου, ο αριθμός των στρωμάτων μειώθηκε με διάβρωση του δείγματος σε ατμόσφαιρα υδρογόνου και με χρήση ήπιας θερμοκρασίας. Ωστόσο δεν καταφέραμε να επιτύχουμε τον αρχικό μας στόχο και να παράξουμε μονοατομικό στρώμα γραφενίου. Αντί αυτού καταφέραμε όμως να μειώσουμε το δείγμα σε AB-stacked ολιγοστρωματικό γραφένιο, κάτι το οποίο έχει επίσης ενδιαφέρον, δεδομένου ότι μέχρι τώρα ήταν δύσκολο να επιτευχθεί η ανάπτυξη μεγάλων επιφανειών AB-stacked γραφενίου μέσω της CVD. Αξίζει επίσης να σημειωθεί ότι η παραπάνω διαδικασία δεν προκάλεσε εμφανή ελαττώματα στο πλέγμα. Τα πειραματικά αποτελέσματα επιβεβαιώθηκαν μέσω της φασματοσκοπίας Raman και της XPS.

Σε συνέχεια των προηγούμενων, καταφέραμε να ενσωματώσουμε γραφένιο σε πύλες MIS. Τόσο η διαδικασία μεταφοράς του γραφενίου στις πύλες όσο και η εναπόθεση του Al_2O_3 βελτιστοποιήθηκαν προκειμένου να αποφευχθούν τα ελαττώματα στο γραφένιο. Στη συνέχεια μετρήθηκαν οι καμπύλες C-V των πυκνωτών, μέ και χωρίς γραφένιο, για να προσδιοριστεί η επίδραση του γραφενίου στη λειτουργία της συνολικής δομής. Τα αποτελέσματα έδειξαν μία μεγάλη αύξηση έως και 35% της συνολικής πυκνότητας στη συσσώρευση, πάνω από τη γεωμετρική πυκνότητα. Αυτή αποδόθηκε στην συμμετοχή της αρνητικής κβαντικής πυκνότητας του γραφενίου, μετά από θεωρητική αναπαράσταση του μοντέλου της εν λόγω διάταξης.

Τέλος, εξετάστηκε η σταθερότητα του γραφενίου επάνω σε διαφορετικά δισδιάστατα υποστρώματα όπως τα h-AlN/Ag111, h-BN/Ni111, $HfSe_2$/Ni111 και $MoSe_2$/$TaSe_2$, μέσω της θεωρίας συναρτησιακού της πυκνότητας (DFT). Επιπλέον, από τη μελέτη των

ηλεκτρονιακών ιδιοτήτων των δομών που αναφέρθηκαν παραπάνω, προέκυψε ότι τα διελεκτρικά υλικά με μεγαλύτερο ενεργειακό χάσμα (h-AlN, h-BN and $MoSe_2$) δεν επηρεάζουν τις ηλεκτρονιακές ιδιότητες του γραφενίου, ενώ αυτά με μικρότερο ενεργειακό χάσμα ($HfSe_2$) σαφώς επηρεάζουν περισσότερο σημαντικά την τοπική πυκνότητα καταστάσεων (LDOS) του γραφενίου. Ως προς τα μέταλλα, αποδείχθηκε ότι ο Ag(111) διαφοροποιεί πιο έντονα τα LDOS του γραφενίου σε σχέση με το Ni(111) ή το $TaSe_2$. Τέλος επισημαίνεται ότι η μέθοδος DFT χρησιμοποιήθηκε για να αναλυθούν οι μετρήσεις ARPES των διαφορετικών δισδιάστατων μεταβατικών μετάλλικών διχαλκογενίδων όπως τα $TaSe_2$, $ZrSe_2$ και $HfSe_2$.

Table of Contents

Chapter 1

Introduction

1.1 Meeting new challenges

Since the first bipolar transistor was manufactured in 1947 at the Bell Laboratories [**1**], the silicon-based technology has experimented a great advance. The well-known Moore's law [**2**], which predicts that the number of transistors in an integrated circuit doubles approximately every two years, has perfectly described this evolution the last decades. But this observation law latterly needs a continuous revision due to the limitation problems of going further with the silicon technology.

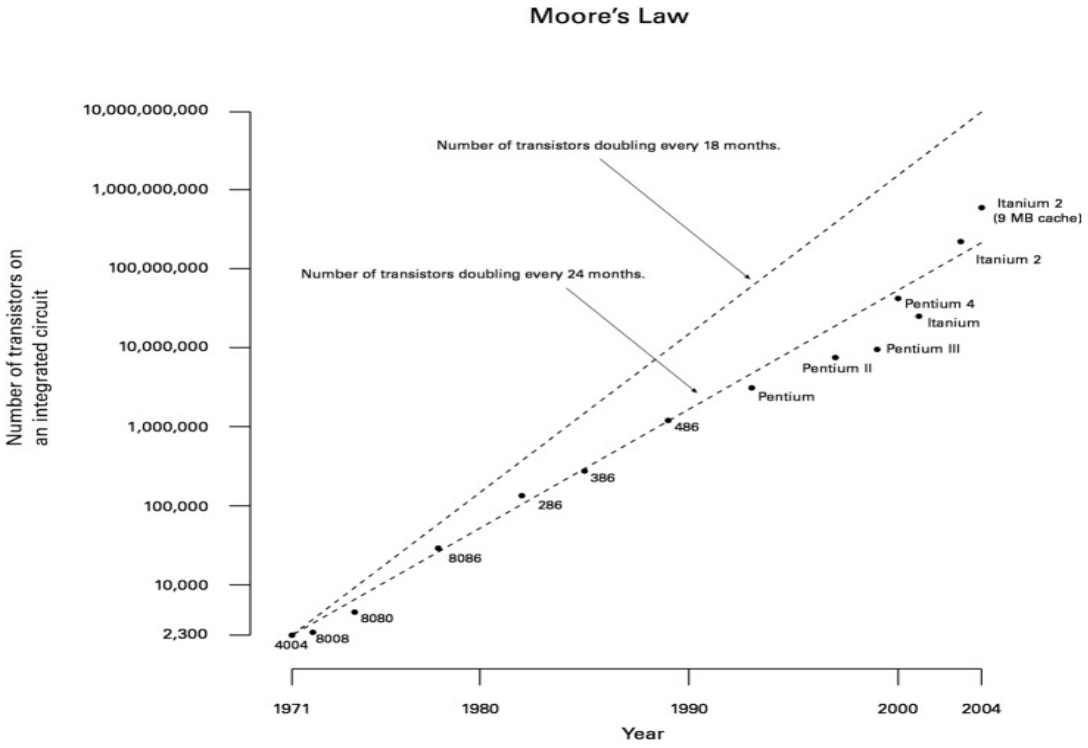

Figure 1. Moore's law.

Aspects such as the size of the channel, the materials that conform the gate, the oxide thickness or the architecture of the transistor have been the main factors that the scientific community has dealt with throughout this period, in order to build faster, more efficient and more powerful devices.

It is further known that the transistor speed depends on the current flowing through the channel, which depends on the materials that conform the gate, the geometry of the gate and the voltage applied. The relation between the current and these parameters in the saturation region is described as follows

$$I_d \propto \frac{W}{L}\mu C_{ox}\left(V_g - V_{th}\right)^2$$

where I_d is the current that flows through the channel, W is the width of the channel, L the length of the channel, μ the mobility of the charges, C_{ox} the capacitance of the oxide, V_g the voltage applied in the gate and V_{th} the threshold voltage.

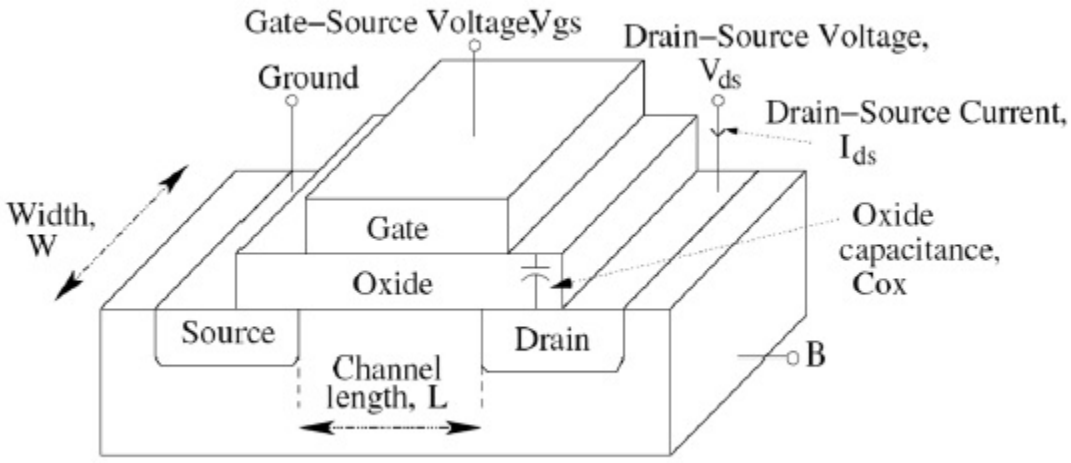

Figure 2. MOSFET structure.

The need for lower power consumption excludes the option of increasing the voltage applied to get a better current performance as this would also increase the leakage currents. Thus, other ways have been chosen.

The effort to decrease the channel size, which is the limitation parameter in the geometry, has currently reached the 22nm. However it is expected for this technology to stop working at channel lengths smaller than 10 nm, due to the increment of the tunneling and leakage currents as the devices become smaller. Furthermore, short channel transistors often meet with the well known problems of the velocity saturation effect, threshold voltage variations and hot carriers effect.

To this end, an effort has been made to search for other materials to achieve improvements at the mobility or the capacitance of the dielectric such as high-k dielectrics which allow a reduction in the oxide thickness. The use of such dielectrics became necessary since the thickness of the silicon dioxide had reached the 1.2nm, a thickness for which the leakage currents become dominants. New materials with a lower threshold voltage are also interesting. A decrease of the threshold voltage allows a decrease of the voltage applied. This means that the power consumption is reducing without losing performance.

The architecture of the transistors has also been studied as a way to overcome some of these problems. Transistors with vertical channel and multi channel transistors, such as FinFET, have been successfully designed. FinFET is a nonplanar transistor with two

gates where the conducting gate is wrapped by a thin silicon fin. The thickness of the fin (measured in the direction from source to drain) determines the effective channel length of the device. The wrap-around gate structure provides a better electrical control over the channel and thus helps in reducing the leakage current and overcoming other short-channel effects, but still has some limitations such the fabrication of a thin silicon fin. An alternative, ultra thin body transistors (UTB), has been also presented. On these UTB transistors it is used a thin silicon film with a thickness that is approximately one-half of the source-to-drain spacing. When a transistor is made with such a thin body, the gate potential controls all source-to-drain current paths—even the ones furthest away from the gate. As the gate modulates the potential of the channel region, it also modulates the potential of all the other sub-surface leakage paths, thus the UTB transistor does not rely on body doping to provide a potential barrier between the source and drain. As a result, the reduction in source-to-drain leakage is a promising method for controlling the leakage current in sub-20 nm transistors.

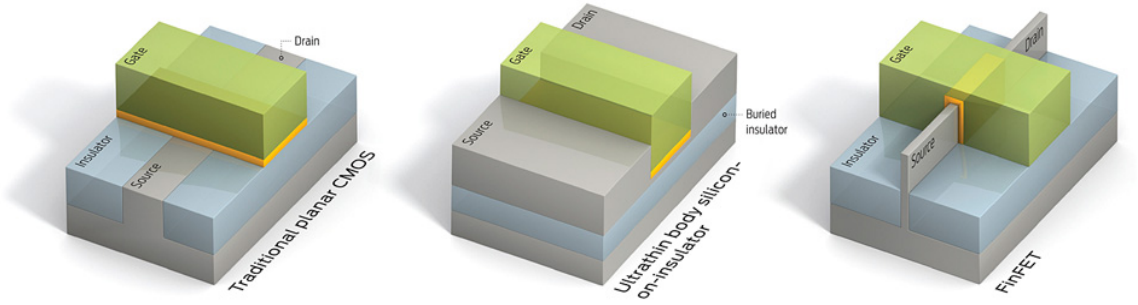

Figure 3. Traditional planar CMOS field-effect transistors, UTB and FinFET.

1.2 The 2D materials and graphene

Material science has been playing a major role in helping to overcome some of these problems, and after the graphene isolation on a SiO2/Si wafer by Geim at al. [**3**], 2D materials have opened a new opportunity to go further with the scalability. The main advantage of these new materials is their low dimensions, ideally the one atomic layer thickness in the case of graphene, silicene [**4**] or germanene [**5**]. Single layer of transition metal dichalcogenides are also interesting. Beside them it can be found metallic materials such as $TaSe_2$ [**6**] and dielectrics with a large gap such as $MoSe_2$ [**7**]. Furthermore, there are other materials with different surface topological order with respect to their bulk, as well as other edge topological order in the case of 2D materials, such as Bi_2Se_3 [**8**] and stanene [**9**] which are topological insulators. Thus, 2D materials can cover a wide range of needs. Among these 2D materials, graphene is one of the most studied and promising materials.

Graphene is defined as an one atomic layer of carbon with sp2 bonds in a honeycomb lattice. In other words is a single layer of graphite, and it is also the base to build other

graphitic materials such as carbon nanotubes. Due to its structure, graphene has extraordinary mechanical and transport properties. A suspended single layer of graphene is one of the stiffest known materials characterized by a remarkably high Young's modulus of 1TPa [**10**]. Regarding its transport properties, graphene shows outstanding electron transport properties due to its 2D hexagonal crystal structure and the presence of charge carriers behaving like massless particles. It is characteristic that a mobility of 200000 $cm^2V^{-1}s^{-1}$ for single layer suspended graphene has been reported [**11**].

The electronic structure of graphene presents a linear dispersion at the K point of the honeycomb lattice in the reciprocal space. This linear dispersion indicates that fermions behave like particles without mass. This behavior is responsible of the high mobility. It is worth noting that when graphene is placed on a substrate loses some of this ideal transport property; for example graphene on SiO2/Si is limited to 10000 $cm^2V^{-1}s^{-1}$ [**12**]whilst on hexagonal boron nitride it has a mobility up to 60000 $cm^2V^{-1}s^{-1}$[**13**].

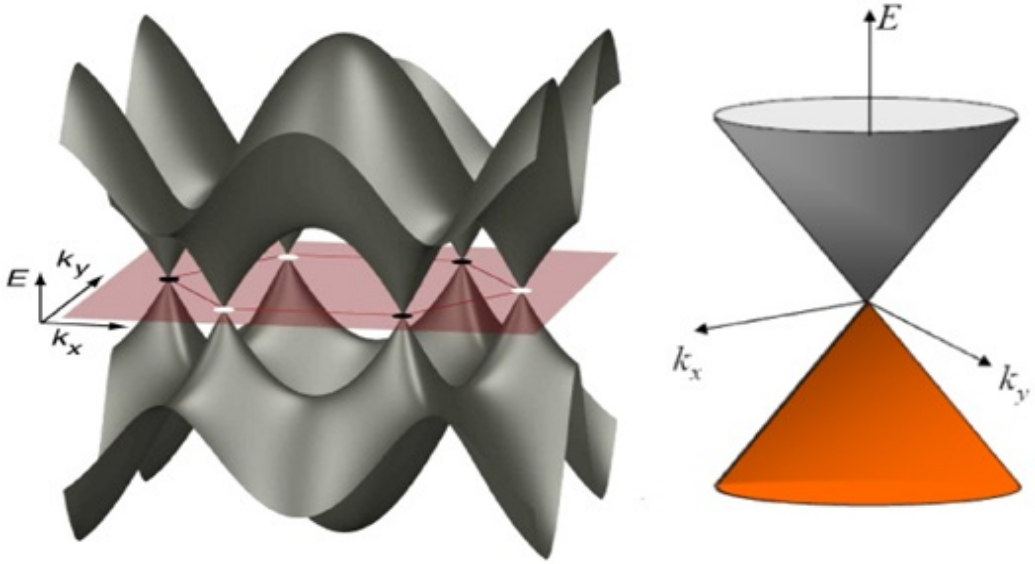

Figure 4. The energy dispersion E(kx,ky) of graphene

The band structure also shows that valance and conduction bands of graphene touch each other only at the K point. So graphene does not have a band gap and this is a major disadvantage for the use of graphene as a channel in transistors. However. it is possible to open a gap in the electronic bands of graphene by functionalization of graphene, by applying a strain or by using few layers graphene with an AB stacking. A gap can be also opened by cutting graphene in nanoribbons. Nonetheless, when we try to engineer the electronic bands of graphene its great transport properties are affected. To this end, other phenomena could be used for the application of graphene in electronics, such as the tunnel effect between two layers of graphene separated by a thin dielectric [**14**] or its negative quantum capacitance. In this last case embedding graphene can be used as a part of the dielectric of the gate, even at a room temperature [**15**].

In spite of the extensive study that has been performed on graphene there are still several open questions to be answered. Despite the effort made over the last decade on graphene there is still no absolute control of the quality of the graphene growth. Graphene is still grown in a polycrystalline form, which comes with many domain boundaries that introduce defects affecting its mobility.

The difficulty of growing graphene with an AB-stacking order is generally acknowledged, especially using chemical vapor deposition. Usually growing a few layers graphene with this technique leads to a non AB stacking order, which has different electronic properties from the one we are interested in. Regarding the characterization of graphene, micro-Raman spectroscopy has been proved a powerful tool. Ferrari et al. [**16**] has performed a great work in this direction. More importantly, it is possible using Raman characterization to discern between single layer graphene, bi-, tri-, four- and multi layer AB-stacked graphene. Even progress in characterization of non-AB stacked graphene has been made, but in this case Raman is not absolutely determinant due to the dependence of Raman signal with the substrate, the measurement conditions or the relative twisted angle between graphene layers [**17**]. Consequently, progress in the use of other techniques to characterize non-AB stacked graphene is needed.

In this dissertation I aim to present experimental and theoretical results and try to contribute in solving some of the problems commented above. In addition to this chapter there are other 4 chapters. More specifically, in chapter 2 it will be given a description of the main experimental and theoretical methods used during this research. In chapter 3 it will be presented a research on graphene growth on different substrates and its characterization by Raman spectroscopy. A special attention in this chapter is given to non-AB stacked graphene characterization using angle resolved photoemission spectroscopy. Additionally I will present results on how to achieve few-layer AB-stacked graphene after growing multi-layer AB-stacked graphene by chemical vapor deposition and treating it with the consequent annealing in hydrogenated atmosphere.

In chapter 4 will be presented a MIS capacitor, built using graphene embedded within the dielectric, a method that led to an enhancement of the total capacitance due to the negative quantum capacitance of graphene. In chapter 5 will be presented the theoretical results of graphene on different structures such as hexagonal aluminum nitride on silver, hexagonal boron nitride on nickel, hafnium selenide on nickel and molybdenum selenide on tantalum selenide. Also, it was presented a comparison between DFT calculations and ARPES measurements.

Finally, a summary of the conclusions is presented in chapter 6.

References

[1] J. Bardeen and W. H. Brattain, Phys. Rev. 74, 230 (1948)
[2] G. E. Moore, Proceedings of the IEEE, vol. 86, No. 1, 82-85 (1998)
[3] K. S. Novoselov, A. K. Geim, S. V. Morozov, D. Jiang, Y. Zhang, S. V. Dubonos, I. V. Grigorieva and A. A. Firsov, Science, Vol. 306, Issue 5696, pp. 666-669 (2004)
[4] P. Vogt, P. De Padova, C. Quaresima, J. Avila, E. Frantzeskakis, M. C. Asensio, A. Resta, B. Ealet, and G. Le Lay, Phys. Rev. Lett. 108, 155501 (2012)
[5] M E Dávila, L Xian, S Cahangirov, A Rubio and G Le Lay, New J. Phys. 16, 095002 (2014)
[6] A. T. Neal, Y. Du, H. Liu and P. D. Ye, *ACS Nano*, 8 (9), pp 9137–9142 (2014)
[7] X. Wang, Y. Gong, G. Shi, W. L. Chow, K. Keyshart, G. Ye, R. Vajtai, J. Lou, Z. Liu, E. Ringe, B. K. Tay and P. M. Ajayan, *ACS Nano*, 8 (5), pp 5125–5131 (2014)
[8] Y. Zhang, K. He, C.-Z. Chang, C.-L. Song, L.-L. Wang, X. Chen, J.-F. Jia, Z. Fang, X. Dai, W.-Y. Shan, S.-Q. Shen, X.-L. Qi, S.-C. Zhang, X.-C. Ma and Q.-K. Xue, Nature Physics 6, 584–588 (2010)
[9] F.-F. Zhu, W.-J. Chen, Y. Xu, C.-L. Gao, D.-D. Guan, C.-H. Liu, D. Qian, S.-C. Zhang and J.-F. Jia, Nature Materials, 14, 1020–1025 (2015)
[10] Lee, C.; Wei, X.; Kysar, J. W.; Hone, J. Science, 321, 385–388 (2008)
[11] K.I. Bolotin, K.J. Sikes, Z. Jiang, M. Klima, G. Fudenberg, J. Hone, P. Kim, H.L. Stormer, Solid State Communications, 146, 9-10, 351–355 (2008)
[12] K. Nagashio, T. Yamashita, T. Nishimura, K. Kita and A. Toriumi, J. Appl. Phys. 110, 024513 (2011)
[13] C. R. Dean, A. F. Young, I. Meric, C. Lee, L. Wang, S. Sorgenfrei, K. Watanabe, T. Taniguchi, P. Kim, K. L. Shepard, J. Hone, Nature Nanotech. 5, 722 (2010).
[14] L. Britnell, R. V. Gorbachev, R. Jalil, B. D. Belle, F. Schedin, A. Mishchenko, T. Georgiou, M. I. Katsnelson, L. Eaves, S. V. Morozov, N. M. R. Peres, J. Leist, A. K. Geim, K. S. Novoselov, L. A. Ponomarenko, Science, Vol. 335, Issue 6071, pp. 947-950 (2012)
[15] L. Wang, Y. Wang, X. Chen, W. Zhu, C. Zhu, Z. Wu, Y. Han, M. Zhang, W. Li, Y. He, W. Xiong, K. T. Law, D. Su and N. Wang, *Scientific Reports* **3**, Article number: 2041 (2013)
[16] A. C. Ferrari and D. M. Basko, Nature Nanotechnology 8, 235–246 (2013)
[17] A. Jorio and L. G. Cançado, Solid States Communications, 175-176, 3–12 (2013)

Chapter 2

Experimental and theoretical methods

2.1 Chemical Vapor Deposition (CVD)

Chemical Vapor Deposition is a method used for depositing thin films of a wide range of materials on different substrates [**1**]. In such process one or more volatile precursors are transported inside a reaction chamber where they decompose on a heated substrate and then they are deposited. Chemical reaction occurs on and near the hot surface. The hole process is followed by the production of chemical by-products that are exhausted out of the chamber along with unreacted precursor gases. One great advantage of CVD processing is that it can create coatings of uniform thickness even over complex shapes [**1**].

Among the variety of materials that can be deposited with this technique is the carbon using precursors such as methane or ethylene. CVD method has been lately chosen for graphene growth due to its possibilities for graphene mass production [**2**], which is of main importance to the future graphene-based fabrication by the industry.

CVD process can be categorized according to its application, the reaction chamber used or the precursor and the chemical reaction used. Regarding the reaction chamber, CVD systems can be separated in two different reactors; hot-wall reactor and cold-wall reactor. In hot-wall reactors the chamber is surrounded by a furnace that heats the system. These systems are often run at very high temperatures, limited only by the materials used in constructing the furnace, and at reduced pressures, on the order of Torr to tens of Torrs. In general, hot wall reactors have the advantages of being able to process large batches of substrates, and having relatively uniform substrate temperatures and thus coating thicknesses. Their primary disadvantages are that the walls get heavily coated, requiring frequent cleaning and causing particle problems, and that involves higher thermal loads and energy usage.

In cold-wall reactors, the substrate is heated while the walls are keeping cold. Cold-wall reactors can be run not only at low pressure but at relatively high pressures and usually have the reactive precursors diluted in a carrier gas. They also have the advantages of reduced deposition of material on the walls, which means less cleaning, lower thermal loads on the substrates because of faster heat-up and cool-down times, and lower energy consumption.

Their primary disadvantage is that, especially in the case of smaller batch sizes, the difference between the non-uniformed temperature areas over the substrate are bigger,

something that may lead to non-uniformities to the film's thickness. Nevertheless, non-uniformity problems can be avoided using a graphite box to achieve a uniform temperature in the vicinity of the sample.

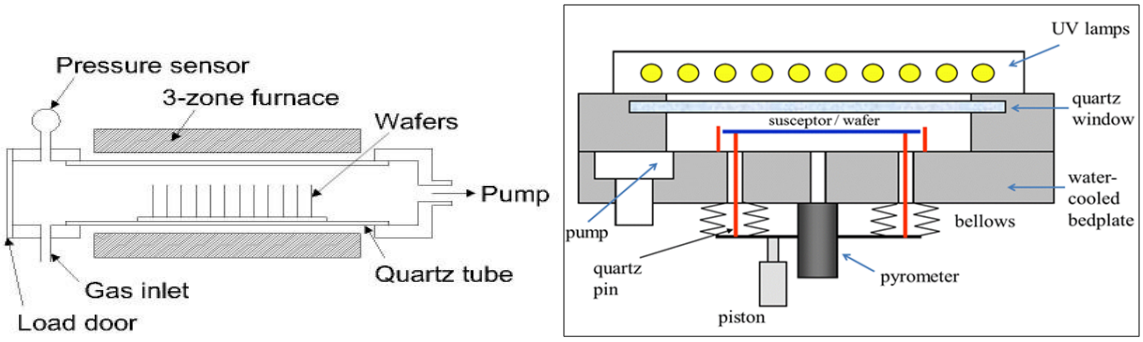

Figure 1. (**a**) a scheme of a CVD hot-wall reactor. (**b**) a scheme of a CVD cold-wall reactor.

In this research conducted at the MBE lab of the Institute of Nanoscience and Nanotechnology (INN) at Demokritos, it was used an AnnealSys AS-One Rapid Thermal Processor, which is a cold-wall reactor. The CVD system is basically composed of a reaction chamber and an external equipment to control the diverse parameters of the processes. A scheme of the reaction chamber is shown at **figure 1b**. As the very one shows, the system uses halogen lamps to heat up the samples. These lamps are separated from the chamber by a quartz window through which the sample is heated. The chamber is equipped by a cooling system that keeps the walls at low temperature.

The samples are placed into a graphite box, the susceptor, which is supported by quartz pins avoiding the contact with the base of the reactor. Below the susceptor a pyrometer is placed to control the temperature of the graphite box, separated from the chamber by a BaF_2 window. Thus the temperature of the sample can be externally controlled. For this purpose the temperature inside the susceptor is calibrated using a thermocouple. The samples can be heated up to 1250°C. The earlier heat up step is controlled by the power, because the pyrometer does not work properly below 200°C. Once the temperature is above 200°C the pyrometer can take the control of the heating. The maximum heat up rate that can be used in this system is 200°C/s and the slowest cool down that can be achieved is 0.01°C/s.

The reaction chamber is equipped with a pump system that allows the control of the pressure inside the chamber from 4.5x10-3 Torr to atmospheric pressure. This system can be also used to extract the unwanted products of the chemical reactions. There are also five different lines that introduce gases in the chambers. Four of them, argon, hydrogen,

methane and ethylene are equipped with a mass flow controller, and the fifth, nitrogen, is regulated with a needle valve. Hydrogen, methane and ethylene are used during the process, while nitrogen and argon are used to keep atmospheric pressure or to purge safely the gases to the atmosphere through an outline.

To control the pressure inside the chamber two different valves are used. A press air valve that simply closes and opens with a direction from the chamber to the pump system and a throttle valve that allows the control of the pressure by fixing a constant opening angle or setting a constant pressure. The pressure is measured with a vacuum gauge manometer at the high range pressures, and with a capacitance manometer that works at low pressure ranges.

The reactor chamber is shown in **figure 2a** where the sample is placed onto the susceptor. In **figure 2b** it is shown the control pressure system and the mass flow controllers. The graphene growing process by the CVD method will be described in detail in the next chapter (Chapter 3).

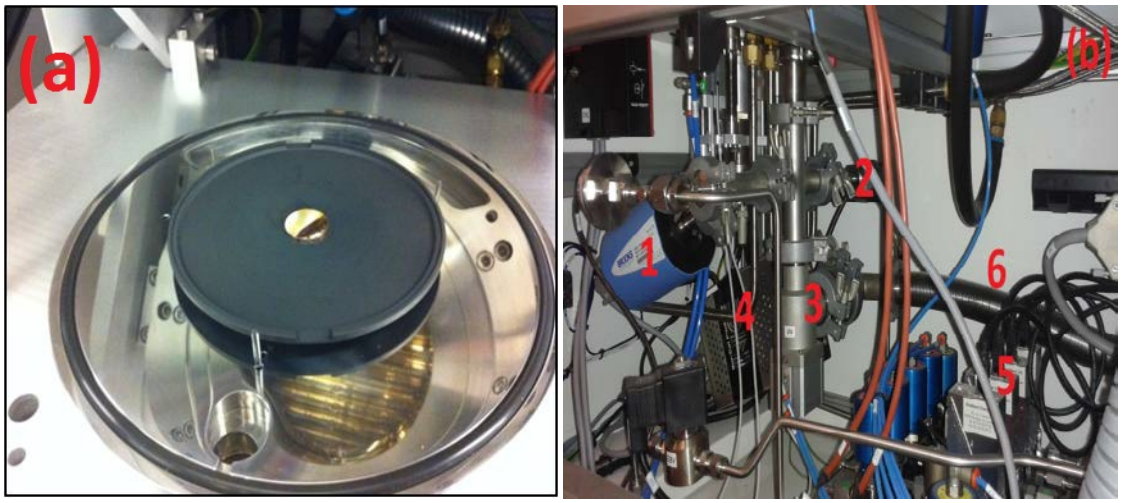

Figure 2. (**a**) it is shown the interior of the cold-wall reactor with the susceptor placed on the quartz pin. (**b**) We can see the different valves, gas lines and mass gas controllers.

1 Capacitance manometer

2 Vacuum gauge

3 Vacuum valve

4 Throttle valve

5 Mass flow controllers

6 Vacuum line

2.2 Micro-Raman spectroscopy

2.2.1 Introduction

Raman spectroscopy is a non-invasive technique based on inelastic scattering of monochromatic light [**3**], usually from a laser source, that can provide detailed structural information of a sample. Recently, the use of micro-Raman spectroscopy has been increased due to its efficiency at the study of 2D materials [**4,5**]. By micro-Raman characterization, information about the quality, number of layers and the structural order of these materials can be provided. Especially, micro-Raman analysis has been intensely used in the study of graphene. Ferrari et al.[**6**] has proved that micron-Raman spectroscopy is currently the most reliable characterization method to study quantitatively and qualitatively graphene samples.

2.2.2 Raman spectroscopy

Light scattering can be regarded as the redirection of light when electromagnetic waves interact with obstacles. As a consequence of the interaction between the sample molecules and electromagnetic waves, electrons within the molecules are disturbed periodically with the same frequency ν_0 as the electric field of the incident wave, creating an induced electric dipole moment. This disturbance of the electronic cloud is then propagated, thereby resulting in scattered light. The scattering processes can be classified in two categories. Elastic scattering at the same frequency ν_0 as the incident wave is called Rayleigh or Mie-Tyndall scattering. Inelastic scattering of light at the emitted radiation has a different frequency ν compared to the incident light, known as Raman and Brillouin scattering.

The phenomenon of inelastic scattering of light by matter was first observed experimentally by C.V. Raman and K. S. Krishnan in 1928 [**7**], a work that granted Raman the Nobel Prize in Physics (1930). The frequency shift compared to the incident light is known today as the Raman shift and can be calculated by the formula

$$\Delta(cm^{-1}) = 10^{-7}\left(\frac{1}{\lambda_{excitation}} - \frac{1}{\lambda_{Raman}}\right) \quad (2.1)$$

where $\lambda_{excitation}$ is the wavelength of the excitation source and λ_{Raman} is the corresponding Raman wavelength.

In classical interpretation Raman effect can be explained by interaction of incident radiation of electric field $\vec{E}$ with a molecule. The incident electromagnetic field induces an electric dipole moment P

$$P = \alpha E \quad (2.2)$$

where α is the electric polarizability of the molecule and E is the amplitude of the electric field corresponding to the incident electromagnetic wave. The polarizability represents an intrinsic property of the molecule and depends on the electronic structure and the nature of the chemical bonds.

A quantitative description of Raman scattering can be obtained using classical electromagnetic theory. Consider an electromagnetic wave defined by

$$E = E_0 \cos(2\pi\nu_0 t) \quad (2.3)$$

where ν_0 is the frequency of the incident light. So the time dependent induce electric dipole moment is

$$P = \alpha E_0 \cos(2\pi\nu_0 t) \quad (2.4)$$

The molecule is fixed in space in its equilibrium position and nuclei can vibrate around their equilibrium positions. Any disturbance in the electronic cloud caused by the incident electromagnetic wave will induce changes in the molecule polarizability. This variation of the polarizability during the vibrations of the molecule can be expressed by expanding the polarizability α in a Taylor series with respect to the coordinates x_i of vibration

$$\alpha = \alpha_0 + \frac{\partial \alpha}{\partial x_i} x_i \quad (2.5)$$

The coordinates of vibration x_i can be written as a sinusoidal function in terms of the vibration frequency ν_i

$$x_i = x_i^0 \cos(2\pi\nu_i t) \quad (2.6)$$

Combining equation 2.5 and 2.6 yields

$$\alpha = \alpha_0 + \alpha_1 x_i^0 \cos(2\pi\nu_i t) \quad (2.7)$$

where α_1 is the derivate with respect to the coordinates of vibration and α_0 is the initial polarization. Then the induced electric dipole moment can be expressed as

$$\vec{P} = \alpha_0 \overrightarrow{E_0} \cos(2\pi\nu_0 t) + \alpha_1 \overrightarrow{E_0} \cos(2\pi\nu_0 t) \cos(2\pi\nu_i t) \quad (2.8)$$

which by using a trigonometry identity for the product of two cosines with different angles can be transformed into

$$\vec{P} = \alpha_0 \overrightarrow{E_0} \cos(2\pi\nu_0 t) + \alpha_1 \overrightarrow{E_0} \frac{\cos 2\pi(\nu_0 + \nu_i)t + \cos 2\pi(\nu_0 - \nu_i)t}{2} \quad (2.9)$$

where the first term represents the Rayleigh scattering and the second term the Raman scattering.

First the polarization and scattering intensity have linear dependence on the laser intensity. It is also clear that only vibrations that change the polarizability of the molecule are Raman active, that is if $\alpha_1 \neq 0$. The changes in frequency, also known as Raman shift can be positive or negative in respect to the laser frequency. Because α_1 is smaller than α_0 the Raman scattering is much weaker than Rayleigh scattering.

The second term shows that there are waves with frequencies $\nu_0 + \nu_i$ which is known as anti-Stokes Raman scattering [**8**] and relates the outgoing scattered photons with an increase in frequency by an amount. This second term also shows that there are waves with frequencies $\nu_0 - \nu_i$ which is known as Stokes Raman scattering and it is associated with a decrease in frequency of resulting scattered photon.

The Stokes and anti-Stokes Raman scattering can also be explained using the Jablonski diagram [**9**], where the origin of inelastic scattering can be explained in terms of energy transfer between incident radiation and scattering molecule.

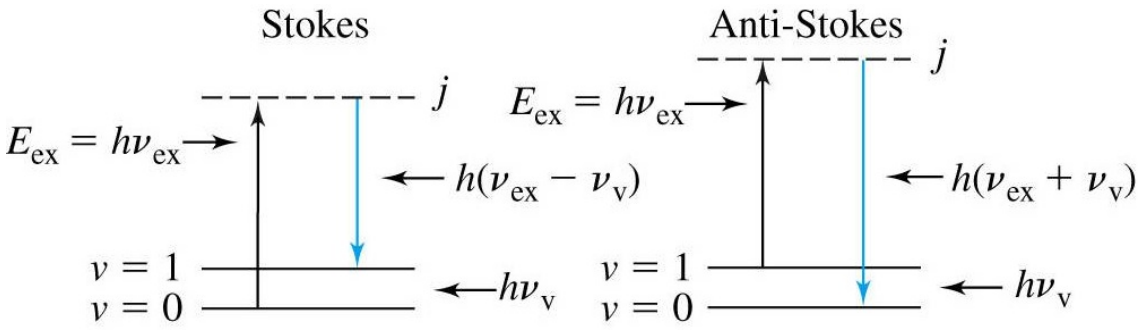

Figure 3. Jablonski energy diagram.

The molecules situated on the ground state are excited to a virtual state followed by relaxation to a vibrational level on ground state, resulting in an energy difference lost, process known as Stoke scattering. Alternatively if the molecule is already on an excited

vibrational level of the ground state, it will excite to a virtual state and relaxed back to the ground state, then the molecule will gain energy. This process is known as anti-Stokes scattering. At room temperature most of the molecules will be in the ground state, therefore it is expected that the majority of the Raman scattering will be dominated by Stokes Raman scattering.

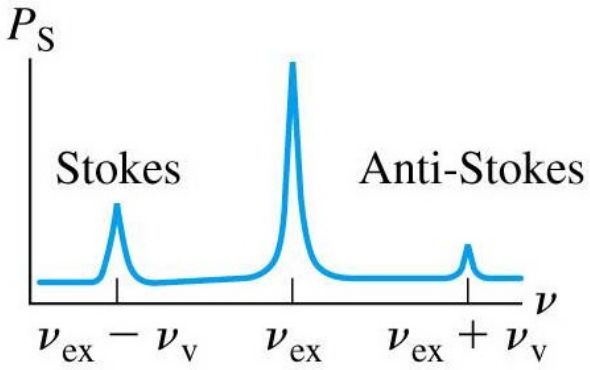

Figure 4. The scattering spectrum with the Stokes and anti-Stokes Raman scattering.

The energy of a vibrational mode depends on molecular structure and environment. Atomic mass, bond order, molecular substituent, molecular geometry and bonding, all effect the vibrational force constant which, in turn dictates the vibrational energy. Vibrational Raman spectroscopy is not limited to intramolecular vibrations. Crystal lattice vibrations and other motions of extended solids are Raman-active, such as vibration between different layers.

Intense Raman scattering occurs from vibrations which cause a change in the polarizability of the electron cloud round the molecule. Usually, symmetric vibrations cause the largest changes and give the greatest scattering. For any molecule with symmetry elements, it is possible to use symmetry to help understand molecular motion by applying group theory. Having assigned the molecule to a point group, group theory can be used to predict whether or not a band will be Raman or infrared active. It is particularly important to note that symmetry considerations allow us to determine whether or not a band is allowed in a Raman or infrared spectrum. This does not tell us how strong it will be; this would require a calculation. There is a group theory table for all point groups which defines the symmetry behavior of every vibration of a molecule belonging to that point group.

One type of vibration forms along the direction of propagation of the radiation (longitudinal or L modes) and the other forms at right angles to it (transverse or T modes). These modes form through the whole crystal and each one consists of a very large number of vibrations of similar energy which occupy a band of energies in the material. The band breadth varies depending on the material.

The Raman spectra of the crystals give information on the lattice modes and the behavior of the crystals. The vibrations of crystals used in semiconductors are reflected in the behavior of phonons. It is this behavior which is studied by Raman spectroscopy. The structural characterization can include the crystallinity, crystallographic orientation, superlattices of mixed crystals, defects, and stacking faults. Besides the structural characterization, electronic characterization can be carried out. Both bound and free charges can contribute to Raman scattering, through collective and single-particle excitation processes.

A typical Raman system consists of four major components. An excitation source, a sample illumination system and light collection optics, a wavelength selector and a detector that is usually a Charge-Couple Device (CCD) sensor.

A sample is normally illuminated with a laser beam. Scattered light is collected with a lens and is sent through interference filter or spectrophotometer to obtain Raman spectrum of the sample.

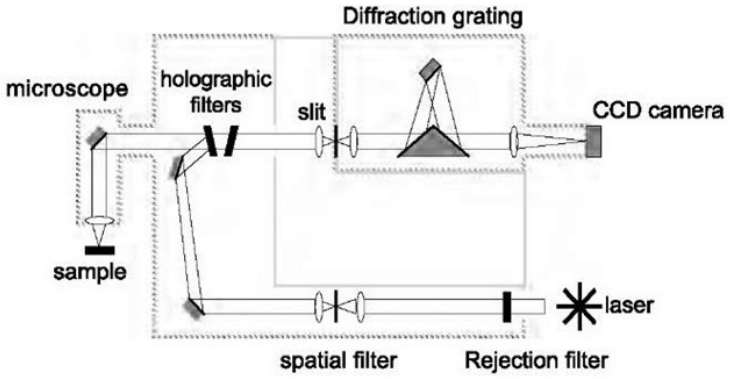

Figure 5. Schematic of a Raman equipment.

During this research two different Raman equipments were used. At micro-Raman Lab at the School of Applied Mathematical and Physical Sciences of the National Technical University of Athens a triple monochromator in subtractive mode was used, with optical microscope of magnification up to 100x, and a liquid nitrogen cooled CCD detector. The system is equipped with motorized stepping drive motors for the scanning of the sample area. For this series of measurements, an excitation Ar^{+} laser beam, at 514.5 nm. At the Sol-Gel-Pulsed EPR Lab at the National Center for Scientific Research "Demokritos" was used a Renishaw InVia Raman microscope using an Ar+ laser with 514 nm.

Figure 6 chapter 2. Raman spectroscopy equipment used, (a) at NTUA and (b) at Demokritos.

2.2.3 Raman spectroscopy in Graphene

Raman spectroscopy has historically played an important role in the study and characterization of graphitic materials [**10**], being widely used in the last four decades. Raman spectroscopy can give information about crystallite size, clustering of the *sp*2 phase, the presence of *sp*3 hybridization and chemical impurities, doping, defects and other crystal disorder, edge structure, strain and number of graphene layers. There is extensive bibliography on Raman spectrum of graphene that try to shade a light on the subject [**6,11-17**]. Raman spectroscopy is a powerful tool to study graphene samples as has been remarked by Ferrari et al. [**11**]. The Raman spectrum of graphene can be affected by the substrates [**12**], their number of layers [**13**], the stacking order [**14,15**], the relative twisted angle between nearby layers [**16**], the presence of defects on the sample [**17**] or even its edge termination [**18**].

As we can see in **figure 7** graphene has two main peaks, the G peak around 1590 cm^{-1}, a first Raman event peak for sp2 carbon bonds, and the 2D peak around 2700 cm^{-1}, which is a second order resonant Raman event due to the interaction of two phonons. Also other peaks can be observed. The D peak, relative to the defects in the lattice, around 1350 cm^{-1} appears due to the interaction between a phonon and a defect. The D' peak around 1620 cm^{-1} is relative to the edge defects of graphene. When it is present another peak around 2970 cm^{-1} appears, called the D+D'. The peak around 2450 cm^{-1}, which is almost present, is called D+D" and it is a result of the resonance between D-peak mode and other non Raman active mode, the D". Recently, it have been studied peaks related to the vibration between graphene layers [**19**]

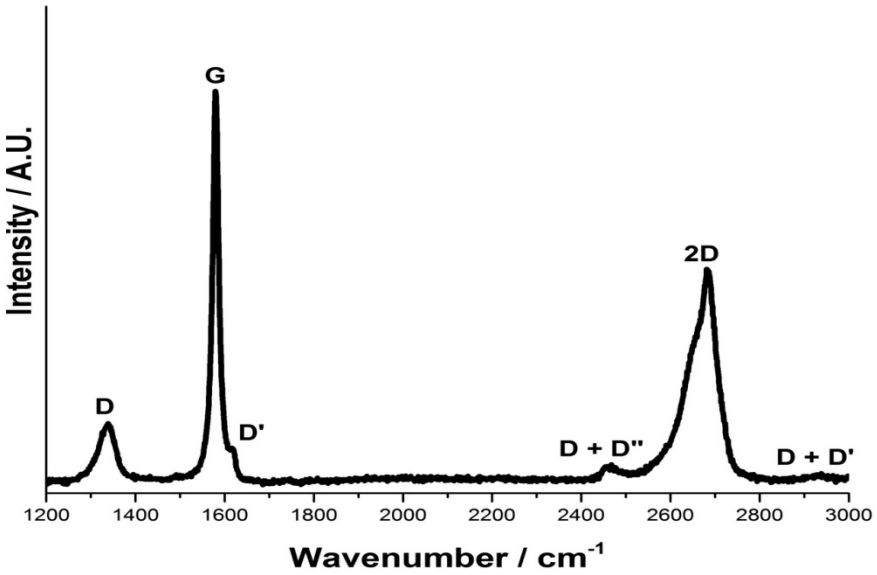

Figure 7. The Raman spectrum of graphene. The top spectrum is an example of single layer graphene without defects. The bottom spectrum is a Complete Raman spectrum with all the possible peaks[**20**].

The intensity of the peaks are defined by

$$I = \frac{A}{\pi * (FWHM)} \quad (2.10)$$

where A is the integrated area under the peak and FWHM is the full width at half maximum. To get A and FWHM the peak is fitted with one Lorentzian-shape band.

The ratio between the intensities of the 2D and G peaks, $\frac{I_{2D}}{I_G}$, the FWHM of the 2D peak and the number of lorentzian that is needed to fit the 2D peak are the main parameters to estimate the stacking order and the number of layers in the case of AB-stacked graphene.

Single layer graphene (SLG) is only fitted with a single lorentzian, its ratio between 2D and G peaks is usually $\frac{I_{2D}}{I_G} \geq 2$ and the $FWHM_{2D}$ is smaller than 39 cm^{-1}. However, the concrete values of $\frac{I_{2D}}{I_G}$ and $FWHM_{2D}$ strongly depend of the measurement conditions and the substrates that holds graphene. When graphene layers are added with an AB stacking order the Raman spectrum varies. The change in the intensity ratio between the 2D and G peaks and the shape of the 2D peak are shown in **figure 8**. For two layers of AB-stacked (BLG) graphene it is needed four lorentzians to fit the 2D peak, the ratio $\frac{I_{2D}}{I_G}$ is reduced approximately at 1.5 and $FWHM_{2D}$ is approximately 45 cm^{-1}. For three and four layers it is only needed two lorentzians with the most prominent peak at lower wavenumber, the

ratio decreases with respect to the SLG and the BLG and the $FWHM_{2D}$ increase. For more than four layers two lorentzians are needed but now the most prominent of the lorentzians is at higher wavenumber. The more layers are added the more similar is the spectrum to the graphite spectrum.

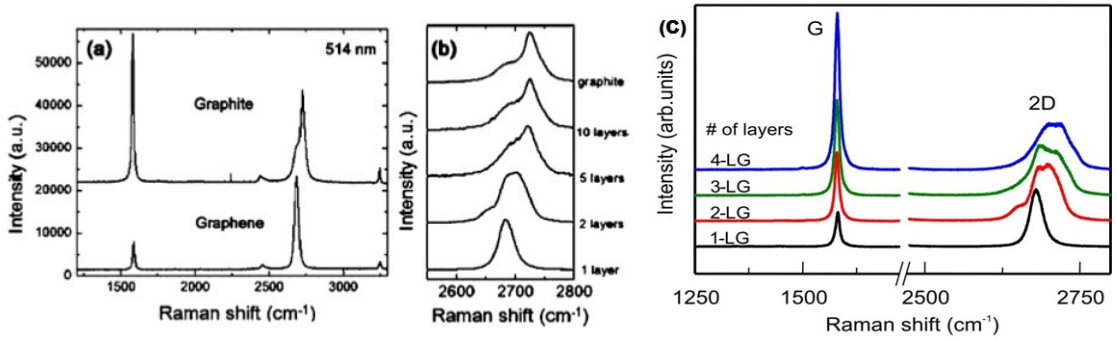

Figure 8. Graphene Raman spectra for different layers of AB-stacked graphene. (a) and (b) [**6**] and (c) [**14**]

It is also possible to discern SLG from non AB-stacked graphene. The 2D peak of graphene with a non-AB stacking order can be fitted with a single lorentzian but its $FWHM_{2D}$ it is usually wider than SLG but narrower than BLG. Also non AB-stacked graphene shows a wide range of intensities ratio between 2D and G peak due to its dependence to the relative twisted angle between graphene layers. Despite of the latest effort to study non AB-stacked graphene with other Raman modes [**19**] it is not always possible to estimate by Raman the number of layers for non-AB stacking order because these modes are not always present in the spectrum.

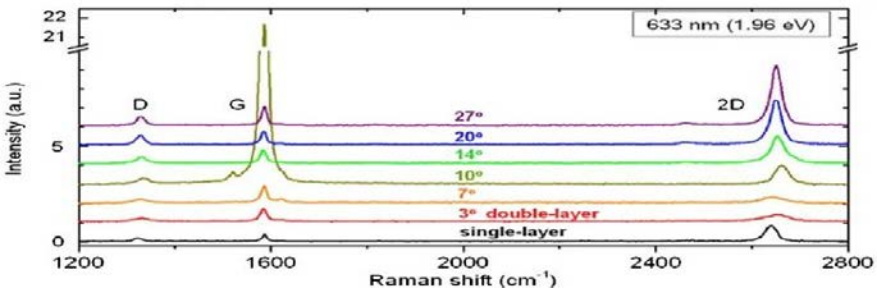

Figure 9. The dependence of the Raman spectrum of graphene with the relative angle between two adjacent graphene layers[**15**].

Graphene defects can be studied using the intensity ratio between D and G peaks, $\frac{I_D}{I_G}$. The larger the ratio is the more defective is the sample. It is also possible to estimate the defect's density [**21**] present in the sample. The distance between defects is defined by

$$L_D^2(nm^2) = (1.8 \pm 0.5) \times 10^{-9} \lambda_L^4 \left(\frac{I_D}{I_G}\right)^{-1} \quad (2.11)$$

where λ_L^4 is the laser wavelength in nanometers. The equation 2.11 is valid for Raman data obtained from graphene samples with point defects separated by $L_D \geq 10nm$ using excitation lines in the visible range. In terms of defect density

$$n_D(cm^{-2}) = \frac{10^{14}}{(\pi L_D^2)} \quad (2.12)$$

Thus the equation 2.11 becomes

$$n_D(cm^{-2}) = \frac{(1.8 \pm 0.5) \times 10^{22}}{\lambda_L^4} \left(\frac{I_D}{I_G}\right) \quad (2.13)$$

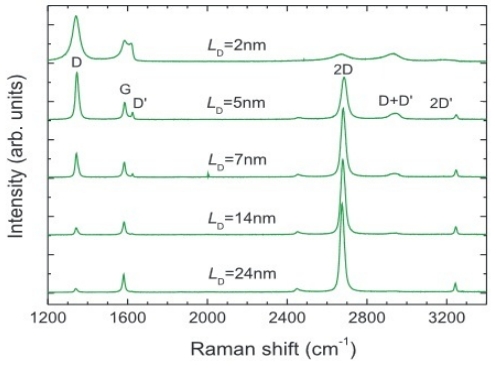

Figure 10. Raman spectra of SLG with different defect grades [**21**].

2.3 Molecular Beam Epitaxy (MBE)

Molecular Beam Epitaxy (MBE) is an Ultra High Vacuum (UHV) technique for producing high quality epitaxial growth, layer-by-layer, by the interaction of one or several molecular or atomic beams that occurs on a surface of a heated crystalline substrate, where they can diffuse and eventually be incorporated into the growing film [**22**].

A UHV system consists of a stainless-steel growth chamber connected to a preparation chamber and a load-lock module to transfer the sample inside and out of the chambers. The components of the growth chamber must be able to resist beak-out temperatures around 200°C for a large period of time, which is necessary to minimize outgassing from the internal walls. When the chambers is exposed to the air their walls become covered by a water film. In order to get rid off this water we needed to beak-out the system. The

UHV also has a pumping system to reduce efficiently residual impurities which practically means reducing the base pressure to $10^{-10} Torr$. This pumping system usually consists of turbo molecular, ion and cryogenic pumps. A pressure in the range of 10^{-2} to $10^{-4}\, Torr$ is needed to turn on the ion and the cryogenic pumps. Turbo molecular pumps can be started at atmospheric pressure and can continue working at UHV conditions but other assistant pumps such as rotary pumps are needed to help to rich the operative pressure. Once the pressure has reached the operative point for the main pump system the rotary pump must be isolated by a valve because at such pressure acts as a leak. A mass spectrometer is also attached to the chamber in order to monitor the residual gas. The entire regime from atmospheric pressure down to $10^{-10}\, Torr$ is actually controlled by two main types of manometer for different pressure ranges. Lastly, the UHV system is equipped with effusion cells that are placed on a source flange, and are co-focused on the substrate heater to optimize flux uniformity.

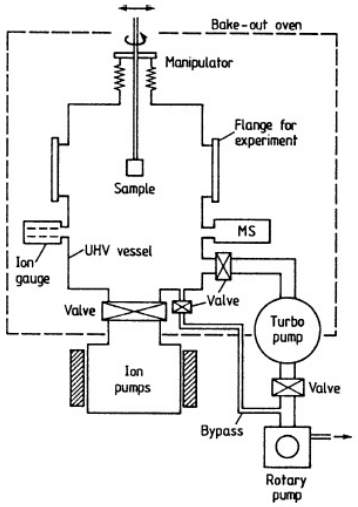

Figure 11. UHV scheme.

Different methods can be used to prepare metal films on a substrate. These methods depend on which materials will be deposited on the substrate. Polycrystalline metal films can be prepared by evaporation and condensation. Metals such as Pt, Pd and Ni can be evaporated from a suitable electrically heated filament. Other materials such as Au and Cu are usually sublimated from a tungsten crucible. In general, materials with a high melting temperature are most conveniently evaporated by electron bombardment. The usual way to control the thickness of a sublimated film is by means of a quartz balance which is mounted close to the sample. That way monocrystalline thin films can be achieved. In this case we talk about epitaxial films and the preparation method is called MBE. Knudsen-type crucibles are used as effusion cells for the evaporation. For most purposes these cells are tubular crucibles, open at one end and made from pyrolytic BN (boron nitride) or high purity graphite.

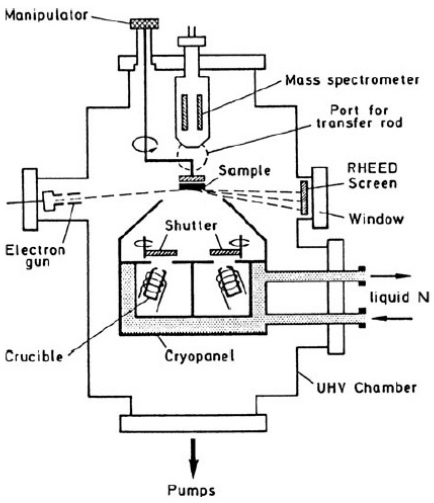

Figure 12. Schematic of the equipment for MBE method.

The MBE at the INN of Demokritos is equipped with three effusion cells and a three pocket electron gun for more refractory materials. A heater mounted in the holder is used to heat up the samples up to 900°C. The pressure is maintained under $10^{-10}\ Torr$ by a cryopump. There is a rotary and a turbomulecular pump in the pre-chamber. To control the epitaxial growth the evaporation rate is measured by a rate monitor and a quartz crystal placed at the sample. In order to grow oxides a RF plasma source of 600 W power and 12.56 MHz frequency is used. The system is also equipped with analysis tools which in the case of this research were a Reflection High Energy Electron Diffraction (RHEED), an XPS, an ARPES and a STM.

Figure 13. UHV system at the MBE lab in the INN Demokritos.

2.4 Reflection High Energy Electron Diffraction (RHEED)

Reflection High Energy Electron Diffraction (RHEED) technique [**22**] uses high energy electrons with primary energies between 10 and 100 keV that are incident under grazing angles (3◦–5◦) onto the sample surface, and the diffracted beams are observed at similar angles on a fluorescent screen. The screen is usually planar and is sometimes coated onto the inside of a window of the UHV system along with a conducting film to prevent charging. No energy filtering of inelastic and secondary electrons is necessary since the diffracted beams are much more intense than the background. The grazing incidence and detection angles mean that a long mean-free path through the sample is associated with penetration normal to the surface of only a few atomic layers. The diffraction pattern will usually consist not of spots, but of streaks corresponding to the sections of reciprocal lattice rod intersected. If there are crystalline islands or *droplets* on the surface, on the other hand, bulk scattering of the grazing beam can occur and the RHEED pattern may become dominated by spots rather than streaks due to transmission electron diffraction.

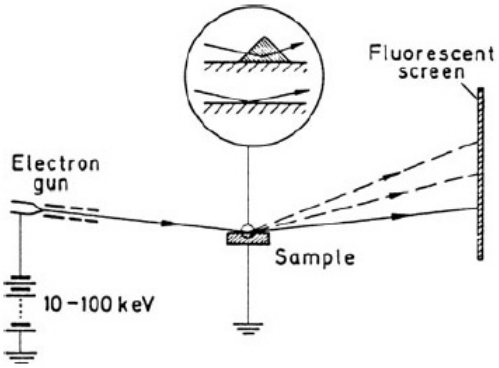

Figure 14. RHEED basic fundaments.

To find the crystallographic properties of the sample surface, Ewald's sphere is used. Ewald sphere is a geometric construct that shows the allowed diffraction conditions for kinematically scattered electrons in a given RHEED setup. The diffraction pattern at the screen relates to the Ewald's sphere geometry, so it can be directly calculated the reciprocal lattice of the sample with a RHEED pattern. The Ewald's sphere is centered on the sample surface with a radius equal to the reciprocal of the wavelength of the incident electrons

$$\kappa_0 = \frac{2\pi}{\lambda} \quad (2.14)$$

where κ_0 is the wave vector of the incident electron.

The diffracted plane wave has a wave vector

$$\kappa_i = \frac{2\pi}{\lambda} \quad (2.15)$$

Since the diffraction process is elastic, κ_0 and κ_i are equal in magnitude differing only in the direction.
An arbitrary vector, G, defines the reciprocal lattice vector between the ends of any two k vectors. Vector G is useful for finding distance between arbitrary planes in the crystal. Vector G is calculated using

$$\vec{G} = \overrightarrow{\kappa_0} - \overrightarrow{\kappa_i} \quad (2.16)$$

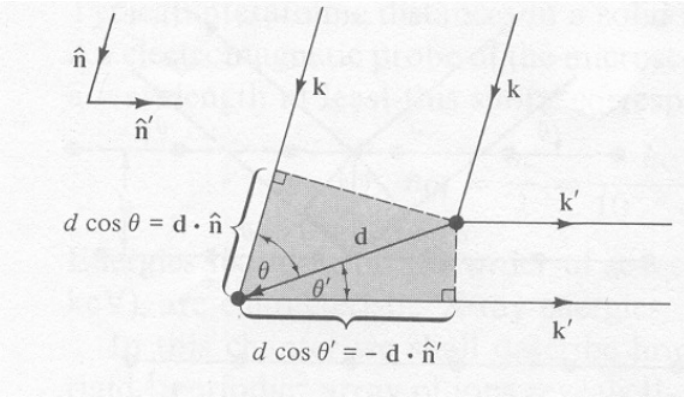

Figure 15. Constructive interface condition.

Then the condition for a constructive interference, as is shown in **figure 15**, from two sites separated a distance d is

$$dCos\theta + d'Cos\theta' = \vec{d}(\hat{n} - \hat{n}') = m\lambda \ (2.17)$$

where m is an integer and $\hat{n}$, $\hat{n}'$ are the unit vectors parallel to the incident and the reflected beams respectively, so the condition can be written as

$$\vec{d}(\overrightarrow{\kappa_0} - \overrightarrow{\kappa_i}) = 2\pi m \ (2.18)$$

The condition holds for all possible $\vec{d}$, so

$$\vec{R}(\overrightarrow{\kappa_0} - \overrightarrow{\kappa_i}) = 2\pi m \rightarrow e^{-\vec{R}(\overrightarrow{\kappa_0} - \overrightarrow{\kappa_i})} = 1 \ (2.19)$$

The relation, which is known as the Laue condition, defines that for a constructive interference it is need that the difference between the two wave vectors, one from the incident beam and the other from the reflected beam, to be equal with a vector of the reciprocal lattice .

The k vectors are labeled such that the k vector that forms the smallest angle with the sample surface is called 0th order beam. The 0th order beam is also known as the specular beam. Each successive intersection of a rod and the sphere further from the sample surface is labeled as a higher order reflection. The center of the Ewald's sphere is positioned in a way that the specular beam forms the same angle with the substrate as the incident electron beam. The specular point has the greatest intensity on a RHEED pattern and is labeled as the (00) point by convention. The other points on the RHEED pattern are indexed according to the reflection order they project.
Rows of reciprocal lattice rods actually intersect the Ewald's sphere as an approximate plane because identical rows of parallel reciprocal lattice rods sit directly in front and behind the single row shown.

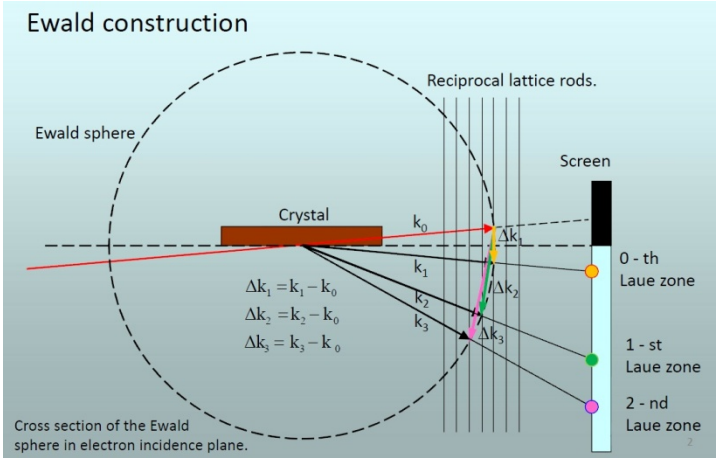

Figure 16. Cross sectional view of a single row of reciprocal lattice rods filling the diffraction conditions.

2.5 Photoelectron Spectroscopy

Photoelectron Spectroscopy (PES) is a general term used to describe the characterization techniques that study the surface of a material by using either X-rays or ultraviolet (UV) light as an excitation source to promote an electronic emission [**22**]. The physical effect upon which these techniques are based is the photoelectric effect. The theory underlying this effect was quickly established together with the quantum theory, being Rutherford and Einstein [**23**] two of the well-known scientists who worked on its development.

However it was not until the second half of the century that other researchers could develop some experimental devices that used the photoelectric effect to characterize the surface properties of materials. Those initial works culminated with a publication in 1957 by Kai Siegbahn [**24**], who explained how to obtain a spectrum by using X-rays as excitation source. At the same time, David W. Turner started to study free molecules in a gas phase by exciting them with ultraviolet light and collecting the emitted electrons. When X-ray excitation is used in PES, the technique is called XPS and it is used for the chemical analysis of the surfaces taken the information from the core levels of the materials. When UV excitation is used in PES, the technique is called UPS and it is used to get information from the valance band of a material.

In this technique the solid is irradiated by monochromatic photons which excite electrons from occupied states into empty states (within the solid) so that they are released into vacuum (free-electron plane-wave states) and detected by an electron-energy analyzer. Thus the kinetic energy of the emitted photoelectron is determined and its wave vector k^{ex} outside the solid is derived from its energy and the direction of the analyzer aperture with respect to the sample orientation.

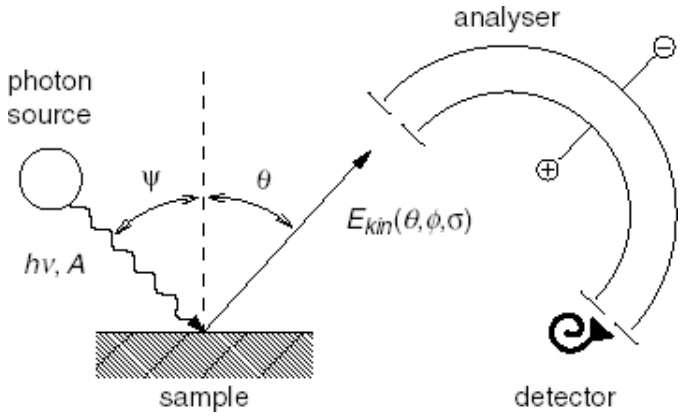

Figure 17. Basic principles of a photoemission spectroscopy measurement.

In photoemission process, an atom absorbs a photon of a known energy, hν, resulting in an ejection of a electron, which is detected and measured. The sample is in electrical

contact with the spectrometer so that both have a common reference for the measuring electron energy, called the Fermi level, E_F. Incoming photons create a photoelectron with kinetic energy E_k^1 relative to the vacuum level E_v of the sample. The kinetic electron energy at the sample surface, E_k^1, is determined by the kinetic energy of the electron E_k measured inside the spectrometer. The relation is given by

$$E_k = E_k^1 - (\varphi_{spec} - \varphi_s) \quad (2.20)$$

where φ_{spec} and φ_s are work functions of the spectrometer and sample, respectively. The binding energy may be obtained by

$$h\nu = E_b + E_k + \varphi_{spec} \quad (2.21)$$

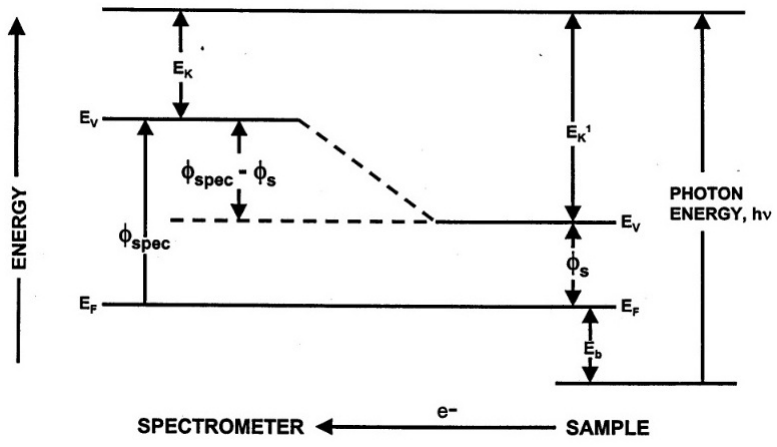

Figure 18. Energy level schematic for XPS binding energy measurements.

2.5.1 X-ray Photoelectron Spectroscopy (XPS)

X-ray Photoelectron Spectroscopy (XPS), as it is describe above, is a photoemission spectroscopy technique [**22**], used to study the core-level excitations which require high photon energies, in a range of 1000-1500 eV. Some of the most common sources are shown in **figure 19**. The anodes of X-ray sources are water cooled in order to enhance the maximum emission intensity. The linewidths of the characteristic X-ray emission lines are several hundred meV, such that fine-structure investigations or the analysis of chemical shifts, etc. are difficult if not impossible without the use of X-ray monochromators. Thus, for studies of core-level fine-structure, X-ray tubes are used in combination with an X-ray monochromator containing a crystalline mirror as a dispersive element.

Source	Energy [eV]	Relative intensity	Typical intensity at the sample [photons/s]	Linewidth [meV]
$MgK_{\alpha 1,2}$	1253.6	100	$1 \cdot 10^{12}$	680
Satellites $K_{\alpha 3}$	1262.1	9		
$K_{\alpha 4}$	1263.7	5		
$AlK_{\alpha 1,2}$	1486.6	100	$1 \cdot 10^{12}$	830
Satellites $K_{\alpha 3}$	1496.3	7		
$K_{\alpha 4}$	1498.3	3		

Figure 19. Table with most common XPS sources.

By collecting the emitted photoelectrons with an electron analyzer, counting them and studying the spectrum of the number of electrons versus its distribution of kinetic or binding energy, it is possible to recognize the material they come from. The analysis of a wide range of binding energies will provide unique signatures of the elements as a function of their atomic number, thus providing elemental analysis. Moreover, if a mixture of elements is present, binding energy information will be related to all the elements and to their concentration ratio (the spectrum of a mixture of elements is approximately the sum of the spectra of the individual components). In this case a new problem arises: to determine the element from which a specific electron belongs, because overlapping of orbital levels from different elements could appear. This difficulty can be solved by looking for all the other orbital levels to know if the element is present or not.

The typical main features of a XPS spectrum of a solid [**25**] that can be observed is shown in **figure 20**. XPS spectra are in general dominated by sharp peaks corresponding to core level photoemission. These peaks may contain chemically shifted components and be spin-orbit split. Their binding energies always incorporate the contribution of the relaxation shift and their linewidth can be affected by many-body effects, instrumental resolution and natural broadening. In many cases, from the relative intensity of core level peaks one can estimate semi-quantitatively elemental ratios, in order to assess the relative

surface coverage of adsorbents and contaminants or the stoichiometry of a compound. To this purpose it is necessary to correct the relative intensities by the respective photoionization cross-sections, which express the probability of creating a photoelectron in each core level at the photon energy $\hbar\nu$. Together with core level lines, electron emission from the valence band is also observed. This part of the spectrum thus represents a projection of the occupied electronic states to energy above the vacuum level, and the photoemission intensity drops to zero above the Fermi level.

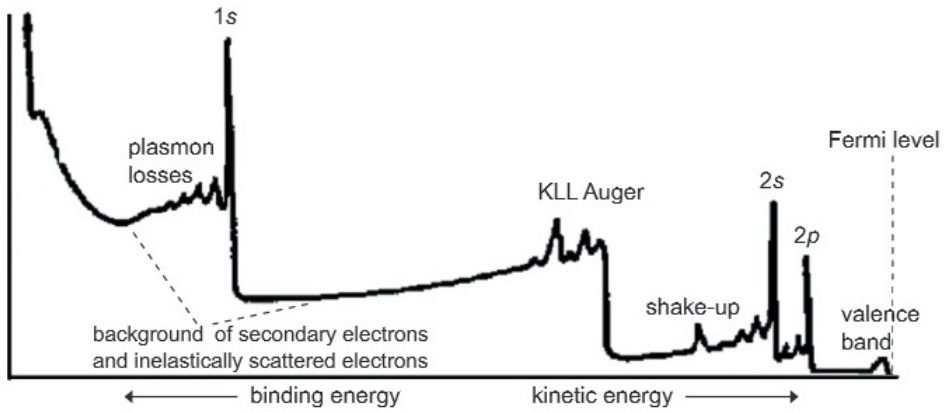

Figure 20. XPS overview spectrum from a solid surface.

Since Auger electrons are also detected by the electron energy analyzer, Auger lines are often observed. If it is possible to change the photon energy for the acquisition of the spectrum, an Auger line can be easily distinguished from a core level line, because the former appears at fixed kinetic energy regardless of the photon energy, while the latter moves linearly with the photon energy according to equation (**2.21**).

Satellites corresponding to multi-electron excitations, such as multiple plasmon losses and shake- up satellites, may also show up in the XPS overview spectrum. Finally, if X-ray emission lines corresponding to different photon energies are used for the excitation, replicas of the same core level peak at different kinetic energy will be observed. Note that all photoemission features appear superimposed on a featureless background, arising from inelastically scattered electrons, which undergo energy losses before escaping from the surface, and secondary electrons excited in "cascade" processes.

All these features can change dramatically the aspect of a high resolution (HR) spectrum for a selected binding energy window. Finally, it is known that the interactions between atoms which form the different types of chemical bonds in molecules and compounds depend only on the valance band levels, while the core levels are not directly involved in the bonding process. However, according to Koopmans' theorem, if the energy of the initial state of the atom changes by the formation of a chemical bond, the binding energy

of the core electrons will change in a fixed quantity equal to the difference in the two atom states

$$\Delta E_B = \Delta\left(E_{initial}\,(n) - E_{final}\,(n-1)\right) \quad (2.22)$$

being n the number of electrons that remains in the atom or ion. The fact that one type of bound or another is formed will affect slightly enough the electron bounded to the core level so as to observe changes when studying its energy at high enough resolution.

XPS equipment is connected with the UHV chamber by a valve in the MBE lab. This way, XPS measurements are performed in situ. The XPS is equipped with two different sources, the MgKα (1253.6 eV) and the AlKα (1486.6 eV).

2.5.2 Angle Resolved Photoemission Spectroscopy (ARPES)

Angle-resolved photoemission spectroscopy (ARPES) has emerged as the most powerful probe of the momentum-resolved electronic structure of materials [**22**]. The general idea of an ARPES experiment is illustrated in **figure 21a.** Monochromatic light of a given energy hν is absorbed by a crystalline material kept in ultra-high vacuum (pressure $<5\times10^{-11}$ Torr) and the intensity of the outgoing photoelectrons is measured as a function of their kinetic energy E_{kin} and emission angles. Via both energy and momentum conservation the measured quantities are directly related to the energy and momentum of the electrons inside the crystal.

An ARPES sensor collects the photoelectrons (**figure 21b)** which provide information about the photoelectron energy, applying conservation laws of energy and momentum, where the energy and the momentum is conserved before and after the photoelectric effect

$$E_{kin} = h\nu - \Phi - E_B \ (2.23)$$

The momentum of photoelectrons could be calculated by

$$p = \sqrt{2mE_{kin}} \ (2.24)$$

in which m is the mass of electron. The momentum components of parallel and perpendicular to sample surface are determined by the polar angle θ and azimuthal angle

Φ of the sample. In the process of photoemission, total energy and momentum parallel to the surface are conserved but the momentum perpendicular to the sample surface is not conserved because of the broken translational symmetry along this direction. For the light source (usually <1000 eV) used in ARPES experiments, the momentum of the photon is negligible comparing to that of electron, so the energy and momentum of photoelectrons, binding energy in solids, crystal momentum in solids could be related by

$$P_{\parallel} = \hbar K_{\parallel} = p \sin\theta = \sqrt{2mE_{kin}} \sin\theta \quad (2.25)$$

in which $\hbar K_{\parallel}$ is the component of electronic crystal momentum parallel to surface in the extended Brillouin zone. For large θ angle, the actual detection of the electron momentum may reach a high level of the Brillouin zone, and one can get reduced crystal momentum in the first Brillouin zone by subtracting the reciprocal lattice vector $\vec{G}$. Because of the breaking of translational symmetry perpendicular to the sample surface, the momentum component in this direction couldn't be directly obtained from regular ARPES experiments. A special situation is that the electronic dispersion perpendicular to the surface is negligible in low-dimensional systems in which the electronic structure is usually strongly anisotropic.

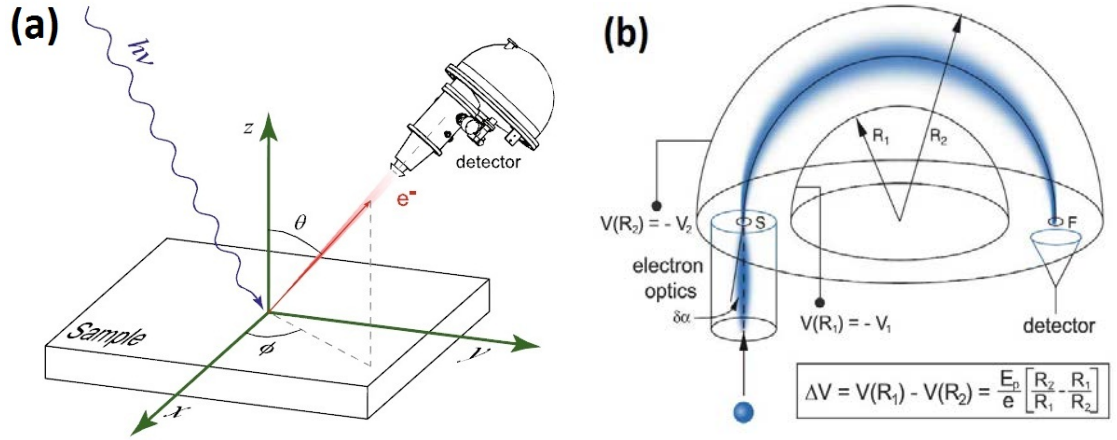

Figure 21. (a) ARPES measurements schematic. (b) Analyzer for ARPES measurements.

The analyzer is an electrostatic 180° hemispherical device. This electrostatic device, which consists of two metallic hemispheres concentrically arranged as in **figure 21**, enables to "disperse" the electrons as a function of their kinetic energy similarly to a prism that disperses light depending on its wavelength. For this purpose, a potential difference ΔV is applied between the inner and outer hemispheres, so that the trajectory of the incoming electrons is bent into a curve. An electrostatic lens between the sample and the entrance slit S of the analyzer focuses the photoelectrons from the sample onto S. At a given ΔV , ideally only the electrons with a well-defined kinetic energy E_p, which is called pass energy, are able to complete their path along the median trajectory of radius

$$R_0 = \frac{R_1 + R_2}{2} \quad (2.26)$$

where R_1 and R_2 are the radii of the inner and outer hemisphere, respectively and emerge at the exit slit F. The choice of the pass energy determine the energy resolution of the analyzer, which quantifies the ability to separate peaks that differ in energy by only small amounts. The lower the pass energy, the better the resolving power.

In the MBE lab, ARPES measurements are performed in the same chamber with the XPS. The ARPES is equipped with three different lines, He-I (energy eV), Ar-I (energy eV) and Ne-I (energy eV).

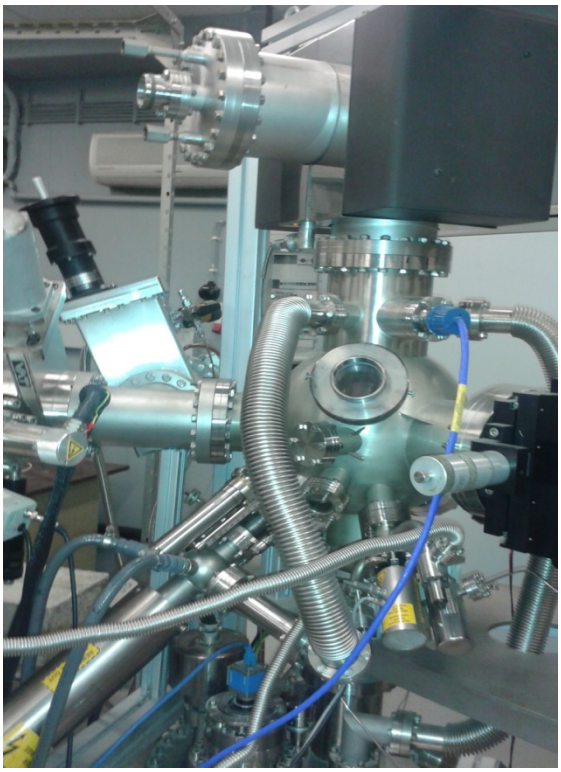

Figure 22. The chamber with the XPS and the ARPES equipment of the INN, Demokritos.

2.6 Electrical measurements

The advances in the new electronic devices require the improvement of the metal insulator semiconductor (MIS) structures since the MIS capacitor [**26**] conforms the central part of the gate of a transistor. A MIS capacitor consists basically of a metal layer on top of a dielectric grown or deposited on a semiconductor substrate.

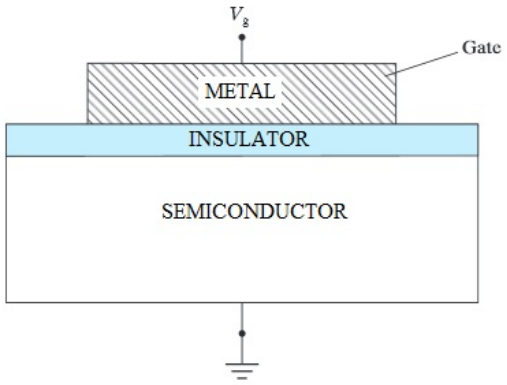

Figure 23. The cross section of a MIS capacitor.

The substrate is usually grounded and the gate can be biased with a voltage, V_G. The semiconductor can be doped n-type or p-type. MIS capacitors are relatively easy to fabricate and to measure which provides useful information about the properties of a gate stack and channel that would be obtained after a full transistor fabrication process.

The band diagrams of a MIS capacitor with n-type substrate and p-type substrate in flatband condition are shown in **figure 24**. The flatband is the condition where the energy band of the substrate is flat at the insulator-semiconductor interface. When the band is flat as shown in **figure 24**, the electric field in the substrate is zero. Therefore the electric field in the insulator is also zero.

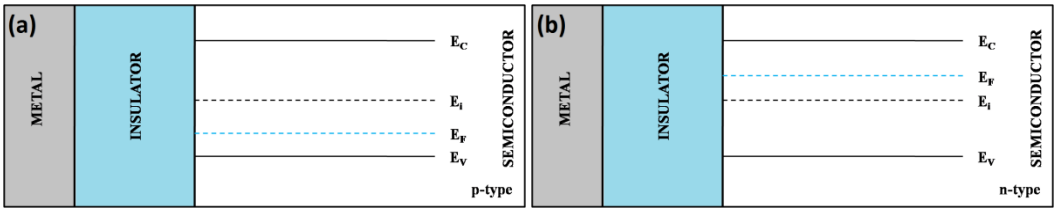

Figure 24. (**a**) flatband for MIS with p-type semiconductors and (**b**) for n-type semiconductors.

Usually when a semiconductor and an insulator are put together bending occurs, due to the difference in the work function of the materials band. The potential that has to be applied at the gate to counterbalance the difference in the work functions that make the bands to be flat is called flat band voltage

$$V_{FB} = \Phi_M - \Phi_S \quad (2.27)$$

where Φ_M and Φ_S are the metal work function and the semiconductor work function, respectively.

In the case of a p-type, if a bias $V_G < V_{FB}$ is applied, the band diagram in the interface would be pushed upward and if a bias $V_G > V_{FB}$ is applied the band diagram would be pushed downward. When the bias applied is $V_G < V_{FB}$ the electrons move and accumulate at the interface; this is the accumulation condition. If now the bias applied is $V_G > V_{FB}$, the valance band bends towards the Fermi level causing the electrons to be repelled from the interface; this is the depletion condition. If we increase the bias applied even more, the Fermi level would be closer to the conduction band and eventually reach the onset of inversion.

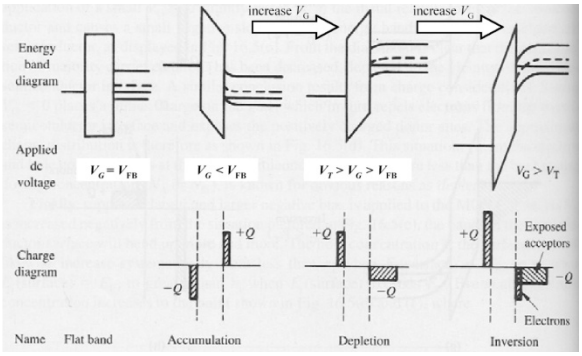

Figure 25. Band diagram of a MIS with p-type semiconductor for different bias conditions.

The ideal capacitance-voltage characteristic of a MIS capacitor with a p-type semiconductor is shown in **figure 26**. The curve can be divided in three regions, accumulation, depletion and inversion. In accumulation the capacitor behaves as a regular parallel plate capacitor, so the capacitance measured is the oxide capacitance. As the capacitor enters the depletion region the carriers are repelled away from the interface, so the oxide capacitance is in series with the depletion region capacitance. When the capacitor enters inversion region the carriers from the bulk cannot respond to a high frequency AC signal, so the curve remains constant at the bottom of the depletion region. At sufficiently low frequencies the carriers can respond to the AC signal and the capacitance becomes equal to the oxide capacitance again.

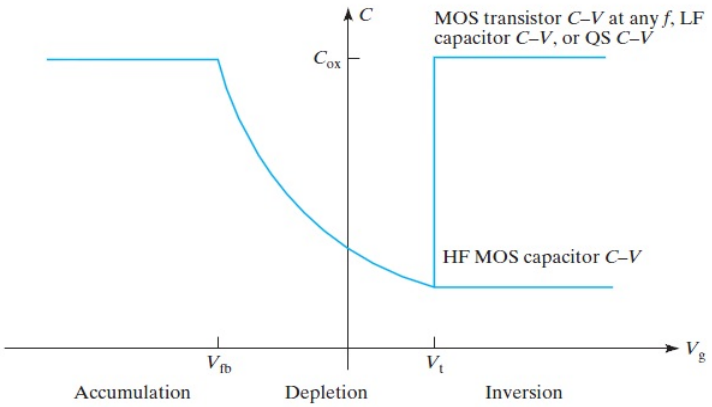

Figure 26. Ideal C-V characteristic of a MIS.

The capacitance at accumulation region is defined as

$$C = \varepsilon_r \varepsilon_0 \frac{A}{d} \quad (2.28)$$

where ε_r is the relative permittivity of the insulator, ε_0 is the vacuum permittivity, A is the area of the capacitor and d is the distance between the gate and the semiconductor.

For a different insulator than the silicon dioxide the equivalent oxide thickness (EOT) can be obtained from the C-V curve

$$C = \varepsilon_{SiO_2} \varepsilon_0 \frac{A}{EOT} = \varepsilon_r \varepsilon_0 \frac{A}{d} \rightarrow EOT = \frac{\varepsilon_{SiO_2}}{\varepsilon_r} d \quad (2.29)$$

Electrical measurements were performed in a Janis research ST-500 micromanipulated probe station. The system is equipped with a Helium liquid system and heaters that permit measurement at range temperatures from 4K to 475K.

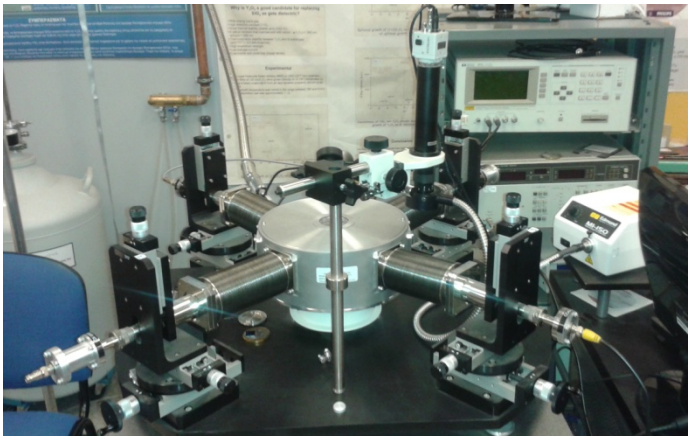

Figure 27. Electrical measurements equipment of the INN, Demokritos

2.7 Theoretical methods

2.7.1 Introduction

Many natural phenomena of interest in material science can be well explained by how electrons behave in the vast environment of other electrons, nuclei, electromagnetic fields and other fundamental forces. For this reason search for a solution of the many-body problem is one of the most important discussion in condensed matter.

The properties of the electrons are accurately described by the many body Hamiltonian of the Schrödinger equation

$$\hat{H} \cdot \Psi\left(\overrightarrow{R_I}, \vec{r_i}\right) = E \cdot \Psi\left(\overrightarrow{R_I}, \vec{r_i}\right) \quad (2.30)$$

where I,i are the nuclei and electron positions. The Hamiltonian associated with this system of N nuclei and n electrons is

$$\hat{H} = -\sum_{I=1}^{N} \frac{\hbar^2}{2M_I} \nabla_I^2 - \sum_{i=1}^{n} \frac{\hbar^2}{2m} \nabla_i^2 - \sum_{I,i=1}^{N,n} \frac{Z_I e^2}{\left|\vec{r_i} - \overrightarrow{R_I}\right|} + \frac{1}{2} \sum_{i \neq j}^{n} \frac{e^2}{\left|\vec{r_i} - \vec{r_j}\right|} + \frac{1}{2} \sum_{I \neq J}^{N} \frac{Z_I Z_J e^2}{\left|\overrightarrow{R_I} - \overrightarrow{R_J}\right|} \quad (2.31)$$

where M_I is the mass of the I-th nucleus, R_I is the position of the I-th nucleus, m the mass of the electron, r_i is the position of the i-th electron, Z_I is the atomic number of the I-th nucleus and e the charge of the electron. The first two terms correspond to the kinetic energy of the nuclei and the electron, and the other three describe the Coulomb interaction between nucleus-electron, electron-electron and nucleus-electron respectively.

A first simplification to the problem can be achieved applying the Born-Oppenheimer approximation [**27**] in order to separate the electronic and nuclear motions. In the Born-Oppenheimer approximation it is assumed that the nuclei are frozen at their positions. This hypothesis can be made because the mass of the electron is more than a thousand times smaller than the mass of the nuclei of the lightest element, then the electrons should move much faster than the nuclei. In other words the state of the electrons is described by the ground state of the many body Hamiltonian of the electrons

$$\hat{H}_e = -\frac{\hbar^2}{2m} \sum_{i=1}^{n} \nabla_i^2 - \sum_{I,i=1}^{N,n} \frac{Z_I e^2}{\left|\vec{R}_I - \vec{r}_i\right|} + \sum_{i \neq j}^{n} \frac{e^2}{\left|\vec{r}_i - \vec{r}_j\right|} = \hat{T} + \hat{V}_{ext} + \hat{V}_{ee} \quad (2.32)$$

Due to the large number of variable, 3n for n electrons, the problem after the approximation is not solvable. A first attempt to overcome this problem was the Hartree-Fock approximation [**28,29]** in which the many-body problem is separated in one-particle states. These states are chosen as the ones that minimize the expectation value of the Hamiltonian in

$$\hat{H} = \sum_{i=1}^{N} \hat{h}(i) + \sum_{i<j}^{N} \hat{V}_{int}(i,j) \quad (2.33)$$

where $\hat{h}(i)$ is the single-particle Hamiltonian for the particle i and $\hat{V}_{int}(i,j)$ is the part of the Hamiltonian describing the interaction between particles i and j. Single-particle Hamiltonian means the terms that would be present if there were only one particle in the system. A second attempt to approximate the many-body problem was the Thomas-Fermi model [**30**]. The Thomas-Fermi theory provides a functional form for the kinetic energy of a non-interacting electron gas in some known external potential $V(r)$ as a function of the density. It is a local density functional and is based on a semiclassical approximation.

2.7.2. Density Functional Theory (DFT)

The main idea of DFT is to describe a many-body interacting system via its particle density and not via its many-body wavefunction. Its significance is to reduce the 3N degrees of freedom of the many-body system to only three spatial coordinates through its particle density.

Hohenberg and Kohn [**31**] showed that the ground state energy of an inhomogeneous electron gas with density $n(r)$ in an external potential $V(r)$ can be written as

$$E[n] = \int d\vec{r}\, V(\vec{r}) n(\vec{r}) + \frac{1}{2} \int d\vec{r} d\vec{r}' \frac{n(\vec{r}) n(\vec{r}')}{|\vec{r} - \vec{r}'|} + G[n] \quad (2.34)$$

where the second term is the Hartree energy and $G[n]$ is an unknown universal functional of the electron density $n(\vec{r})$. The total energy $E[n]$ has a minimum for the correct ground state density.

It was later suggested by Kohn and Sham [**32**] that the functional $G[n]$ can be divided into the kinetic energy of the system of a non-interacting electrons, $T_S[n]$, with electron

density $n(\vec{r})$ and the exchange-correlation (XC) energy of the interacting system, E_{XC}, with electron density $n(\vec{r})$

Thus the equation (**2.34**) becomes

$$E[n] = T_S[n] + E_{XC}[n] + \int d\vec{r} V(\vec{r}) n(\vec{r}) + \frac{1}{2} \int d\vec{r} d\vec{r}' \frac{n(\vec{r}) n(\vec{r}')}{|\vec{r} - \vec{r}'|} \quad (2.35)$$

in which all terms can be determined exactly, except the exchange correlation energy E_{XC}, for which several approximations exist. The external potential $V(\vec{r})$ describes the interaction between the electrons and the nuclei of the system. In order to solve the equation we need to find the electron density that, that means to minimize the equation (**2.35**)

$$\frac{\delta E[n]}{\delta n(\vec{r})} = \frac{\delta T_S[n]}{\delta n(\vec{r})} + \varphi(\vec{r}) + \mu_{XC}(\vec{r}) = \mu \quad (2.36)$$

with

$$\varphi(\vec{r}) = V(\vec{r}) + \int d\vec{r}' \frac{n(\vec{r}')}{|\vec{r} - \vec{r}'|} \quad (2.37)$$

and

$$\mu_{XC}(n) = \frac{\delta E_{XC}}{\delta n(\vec{r})} \quad (2.38)$$

where μ_{XC} is the exchange correlation contribution to the chemical potential of an electron gas with density $n(\vec{r})$. Therefore, for given φ and μ_{XC}, one obtains the electron density n which fulfils (**2.36**) by solving the one-particle time-independent Schrödinger equation

$$\left\{ -\frac{1}{2} \nabla^2 + \left[\varphi(\vec{r}) + \mu_{XC}\left(n(\vec{r})\right) \right] \right\} \Psi_i(\vec{r}) = \varepsilon_i \Psi_i(\vec{r}) \quad (2.39)$$

with the electron density n given by

$$n(\vec{r}) = \sum_{i=1}^{n} |\Psi_i(\vec{r})|^2 \quad (2.40)$$

where n is the total number of electrons.

Equations (**2.37-2.40**) need to be solved self-consistently. One begins with an assumed electron density $n(\vec{r})$, from which $\varphi(\vec{r})$ and $\mu_{XC}\big(n(\vec{r})\big)$ are constructed using equations (**2.37**) and (**2.38**) respectively. A new electron density $n(\vec{r})$ is the found from equation (**2.39**) and (**2.40**). For each iteration the energy is calculates as

$$E = \sum_{i}^{n} \varepsilon_i - \frac{1}{2}\iint d\vec{r}d\vec{r}' \frac{n(\vec{r})n(\vec{r}')}{|\vec{r}-\vec{r}'|} + E_{XC}[n] - \int d\vec{r} n(\vec{r})\mu_{XC}\left(n(\vec{r})\right) \quad (2.41)$$

The self-consistent loop is interrupted when the energy is converged, for example when the difference in energy from two consequent iterations is less than a break condition. The energy given by equation (**2.41**) after the last iteration is the ground state energy for the specific configuration of the nuclei.

When the exchange-correlation potential is exactly known, $V_{XC} = \frac{\delta E_{XC}[n(\vec{r})]}{\delta n(\vec{r})}$, the equations Khon-Sham give an exactly description of the ground state of the interactive electrons system. Unfortunately the exact value of the exchange-correlation potential is unknown. In DFT it is only possible to use an approximation. The better approximation the better result. The most common approximation used are the Local Density Approximation (LDA) and the Generalized Gradient Approximation (GGA).

For LDA the exchange-correlation is

$$E_{XC}^{LDA}[n(\vec{r})] = \int n(\vec{r}) \cdot \varepsilon_{XC}\big(n(\vec{r})\big)d\vec{r} \quad (2.42)$$

where $\varepsilon_{XC}\big(n(\vec{r})\big)$ is the exchange-correlation energy per electron of an homogeneous electron gas.

For GGA the exchange-correlation is

$$E_{XC}^{GGA}[n(\vec{r})] = \int n(\vec{r}) \cdot \varepsilon_{XC}\big(n(\vec{r})\big)d\vec{r} + \int F_{XC}[n(\vec{r}), |\nabla n(\vec{r})|]d\vec{r} \quad (2.43)$$

2.7.3. Program and equipments

To perform the DFT calculation was used the Vienna Ab initio Simulation Package 5.3 (VASP) [**33**] All manuals on how to use this package can be found in the VASP web site [**33**].

The calculations were performed in four different systems. It was used the HellasGrid infrastructure [**34**], the Bibliotheca Alexandrina high-performance computing [**35**] and the high-performance computing system ARIS of the Greek Research and Technology Network [**36**] where many jobs can run simultaneously in a large number of CPU. It was also used the workstation of the MBE Lab which has four processors intel Xeon with eight cores per processor and 256 Gbyte of memory RAM.

References

[1] C.E. Morosanu and G. Siddall, Thin Films by Chemical Vapor Deposition, Elsevier B.V (1990)
[2] E. S. Polsen, D. Q. McNerny, B. Viswanath, S. W. Pattinson and A. J. Hart, Scientific Reports 5, Article number: 10257 (2015)
[3] John R. Ferraro, Kazuo Nakamoto and Chris W. Brown, Introductory Raman Spectroscopy, Academic Press (2003)
[4] P. Hajiyev, C. Cong, C. Qiu and T. Yu, Scientific Reports 3, 2593 (2013)
[5] D. Nam, J.-U. Lee and H. Cheong, Scientific Reports 5, 17113 (2015)
[6] A. C. Ferrari, J. C. Meyer, V. Scardaci, C. Casiraghi, M. Lazzeri, F. Mauri, S. Piscanec, D. Jiang, K. S. Novoselov, S. Roth, and A. K. Geim, Phys. Rev. Lett. 97, 187401 (2006)
[7] Raman, C.V. and K.S. Krishnan, Nature, 1928. 121: p. 501-502.
[8] Turrell, G., The Raman Effect in Raman Microscopy, T. George and C.
Jacques, Editors. 1996, Academic Press: London. p. 1-25.
[9] Jabłoński, Aleksander, Nature 1933, volume 131, pp. 839-840
[10] F. Tuinstra and J. L. Koenig, J. Chem. Phys. 53, 1126 (1970)
[11] A. C. Ferrari and D. M. Basko, Nature Nanotechnology 8, 235–246 (2013)
[12] Y. Y. Wang, Z. H. Ni, T. Yu, Z. X. Shen, H. M. Wang, Y. H. Wu, W. Chen and A. T. S. Wee, J. Phys. Chem. C, 112, 10637–10640 (2008)
[13] D. Graf , F. Molitor , K. Ensslin , C. Stampfer , A. Jungen , C. Hierold and L. Wirtz, Nano Lett., 7 (2), pp 238–242 (2007)
[14] Y. Hao, Y. Wang, L. Wang, Z. Ni, Z. Wang, R. Wang, C. K. Koo, Z. Shen and J. T. L. Thong, Small, 6, 2, 195–200 (2010)
[15] K. Kim, S. Coh, L. Z. Tan, W. Regan, J. M. Yuk, E. Chatterjee, M. F. Crommie, M. L. Cohen, S. G. Louie, and A. Zettl, Phys. Rev. Lett. 108, 246103 (2012)
[16] A. Jorio and L. G. Cançado, Solid States Communications, 175-176, 3–12 (2013)
[17] A. Eckmann, A. Felten, A. Mishchenko, L. Britnell, R.Krupke, K. S. Novoselov, C. Casiraghi, Nano Lett., 12 (8), pp 3925–3930 (2012)
[18] C. Casiraghi, A. Hartschuh, H. Qian, S. Piscanec, C. Georgi, A. Fasoli, K. S. Novoselov, D. M. Basko and A. C. Ferrari, Nano Lett., 9 (4), pp 1433–1441 (2009)
[19] P. H. Tan, W. P. Han, W. J. Zhao, Z. H. Wu, K. Chang, H. Wang, Y. F. Wang, N. Bonini, N. Marzari, N. Pugno, G. Savini, A. Lombardo and A. C. Ferrari, Nature Materials 11, 294–300 (2012)
[20] C. Sole, N.E. Drewett and L.J. Hardwick, Faraday Discuss.,172, 223-237 (2014)

[21] L.S. Cançado, A. Jorio, E. H. Martins Ferreira, F. Stavale, C. A. Achete, R. B. Capaz, M. V. O. Moutinho, A. Lombardo, T. S. Kulmala and A. C. Ferrari, Nano Lett., 11 (8), pp 3190–3196 (2011)
[22] H. Lüth. Surfaces and Interfaces of Solid Materials. 3rd edition Springer.
[23] Photoelectric effect Einstain 1905.
[24] C. Nordling, E. Sokolowski, and K. Siegbahn, Phys. Rev. 105, 1676 (1957)
[25] L. A. Carlsson, D. F. Adams, R. B. Pipes, Experimental Characterization of Advanced Composite Materials, CRC Press (2002)
[26] Sze, S.M.; Physics of Semiconductor Devices, 2nd Ed., John Wiley & Sons, 1981, p. 368.
[27] M. Born and R. Oppenheimer, Annalen der Physik, 389, 457 (1927)
[28] D.R. Hartree, Proc. Cambridge Phil. Soc. 24, 89 (1928)
[29] V. Fock, Z. Phys. 61, 126 (1930)
[30] N. H. March, Advan. Phys. 6, 1 (1957)
[31] P. Hohenberg andW. Kohn, *Inhomogeneous Electron Gas*, Physical Review 136, B864–B871 (1964).
[32] W. Kohn and L. J. Sham, *Self-Consistent Equations Including Exchange and Correlation Effects*, Physical Review 140, A1133–A1138 (1965).
[33] https://www.vasp.at/
[34] http://www.hellasgrid.gr/
[35] http://www.bibalex.org/
[36] https://hpc.grnet.gr/

Chapter 3

Graphene growth by Chemical Vapor Deposition (CVD)

3.1 Introduction

In order to take advantage of the magnificent electronic properties of graphene we need to produce it in large quantities and place it on different kind of substrates to build up electronic devices. One of the techniques to produce large amounts of graphene is the Chemical Vapor Deposition (CVD) [**1**]. To grow graphene by CVD one should need a metal substrate [**2,3**] which will work as a catalyst, a carbon source [**4**] which could be an hydrocarbon gas usually methane or ethylene and a heat source to provide the sufficient energy to trigger the catalysis of the gases. **Figure 1** shows a schematic of a typical CVD process to grow graphene. The process consists of an annealing step to prepare the substrate, in which the substrate is cleaned up or in the case of copper film is treated as to increase the size of the copper grains. Afterwards a growth step follows, where the carbon source is heated near a catalyst surface and the carbon atoms form the lattice on top of the substrate. Finally follows a cool down step where the sample is cooled to room temperature. This step could play a major role in substrates with a high carbon solubility [**5**].

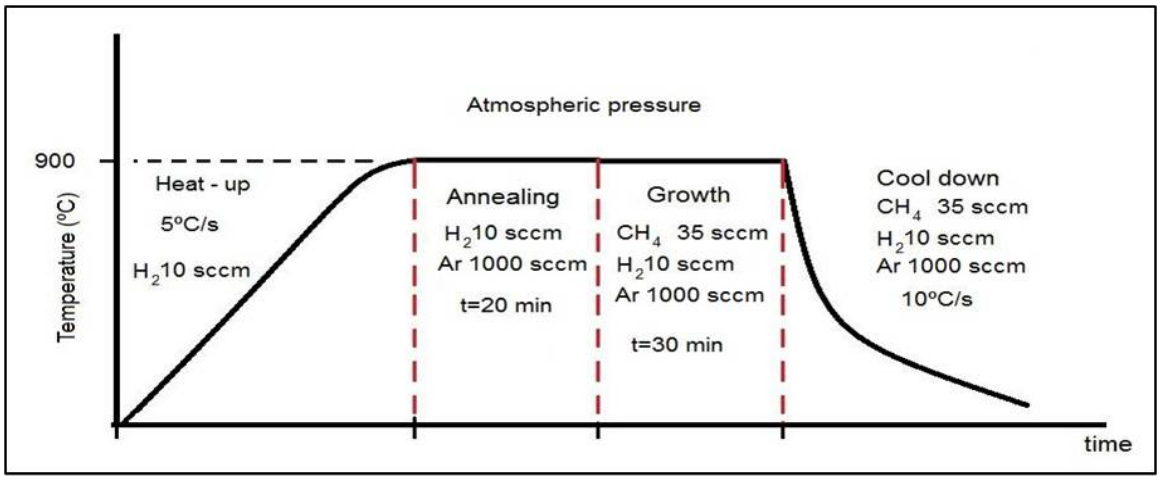

Figure 1. Schematic of a typical CVD process to grow graphene on a metal substrate.

It has been demonstrated that graphene can be grown on different metal substrates such as Cu, Ni, Ir, Ru, Rh [**2,3,6-8**] etc…However, the most common substrate is Cu due to its relative ease to grow single layer graphene [**9**] on it and due to its relative low price regarding other metals such as Ir. That is why copper has been largely studied in general and for the same reason it is mainly used during the experiments of this study, as our main goal is to achieve single layer graphene. Copper was also used in this study to grow non-AB stacked graphene for characterization purposes, since it lacks an extensive study as far as the determination of its number of layers is concerned. Non-AB stacked graphene can offer different but interesting properties than single layer graphene such as photocurrent enhancement [**10,11**].

A second kind of catalyst, nickel, was used for two purposes in this study, the first of those being to be used as a reference towards copper something that also proved how difficult it is to deal with substrates with a larger carbon solubility like nickel. Secondly, we used nickel to grow AB-stacked multilayer graphene as a start point to achieve AB-stacked few layers graphene.

Depending on the metal used, graphene can grow on it through different mechanisms. Metals with low carbon solubility usually catalyze the carbon source and the free carbon atoms lie on the surface, building the lattice with the sp2 carbon bonds. This mechanism stops when the surface is completely covered with carbon and new catalysis of the source is not possible. Metals with high carbon solubility do not have a self-limited mechanism such as the previous one. On these metals, after the catalysis of the carbon source, carbon atoms are absorbed into the bulk metal. When the metal is cooled down the carbon solubility usually changes and carbon atoms are precipitated on the metal surface. Thus, on these metals, graphene not only grows by deposition of the atom in the surface but by atoms that come up from the bulk making it more difficult to control the number of layers. As it was mentioned before, the cooling down would be crucial for these metals, since the number of the carbon atoms precipitated on the surface would depend on the cool down rate [**12]**.

Among the possible carbon sources it can be used a solid, a liquid or a gas [**13-16**]. As a solid carbon source there can be used different polymer films deposited on the metal substrate [**13**] or some carbon paste [**14**] but they both usually grow defective graphene. Liquids such as methanol, ethanol or propanol have been used in previous works [**15**]. However, this kind of source is not possible to be used in our CVD system. Gas sources are the most common for graphene growth by CVD, as we can find within the literature [**4**,**16**]. Methane, ethylene, ethane, propylene are examples of gases often used. In this research, the carbon source used was methane, because it is a source easy to be catalyzed by copper without producing a large amount of carbon atoms that eventually could be difficult the control such as a larger number of graphene layers.

During the growth step, there are many parameters that can play an important role. Parameters such growth duration, temperature, carbon source flow rate, pressure, partial pressure of the different gases or if hydrogen is either used or not, can be changed in order to control the growth process. Temperature is probably the most important of them because without a proper temperature the catalysis of the carbon source could not occur. Even if the temperature is sufficient to catalyze the source, it would not be sufficient to produce carbon atoms completely free of radicals that can be the origin of defects or sp3 bonds [**17**]. Thus, it is important to choose a proper temperature, which will also depend on the metal substrates. Once the temperature of the process is chosen, the duration of the process and the quantity of the carbon atoms available in the chamber are very

determinant parameters. Playing with these parameters is possible to cause either a non full covered surface or even many graphene layers.

Since we want to control the number of layers at the degree of growing only a single layer, there is something that needs to be extensively studied in each CVD equipment. Beside the source flow rate, the other parameters have an influence on the amount of carbon atoms. Especially, the use of hydrogen in the growth step, which usually helps in the catalysis [**18**] or the partial pressure of the carbon source [**19**]. In this research, since temperature was set by the election of the metal, the duration, the flow rate of the source and the partial pressure were the parameters more extensively studied.

The annealing step, which is initially used to clean the substrate, can be used to affect the size of the metals grains. For instance, in substrates such as the thin metal films on dielectrics the grain size could be really important. Grain boundaries and steps are usually sites where the catalysis process is strong, so they work as nucleation points from where graphene is grown [**20**]. Thus, the larger the grain the less grain boundaries are in the film so the less nucleation points. Additionally, since these films are polycrystalline, each grain has a different crystal orientation and so the graphene grows with different orientation too. When graphene islands, with different crystal orientations meet, defects are created and that is something we want to avoid. Thus, preparing a substrate with larger grains can help us grow well-oriented graphene with less defects and better transport properties.

Since graphene grown by CVD is usually on a metal substrate, we need to transfer it on a substrate such as silicon dioxide [**21**], some other dielectric or semiconductor [**22**] in order to build a device. For this purpose it is usually used a polymer thin film, spin-coated on graphene, that will serve as material support for graphene. Polymethyl methacrylate (PMMA) is the most common among other polymer films such as Polystyrene (PS) or Polydimethylsiloxane (PDMS) [**23-25**]. The spin-coated polymer is baked on a hot plate until the polymer becomes solid. Consequently, the sample is placed into a proper chemical to etch away the metal substrate. Then, the polymer film with the graphene layer attached to it is rinsed with deionized water to be cleared of any chemical residues and the film is placed in the final target substrate. Finally the polymer is etched using a solvent solution. Usually, polymers lead to undesirable residues on graphene. It is crucial to work in the manner that the polymer it will be etched. More details of our transfer will be given below.

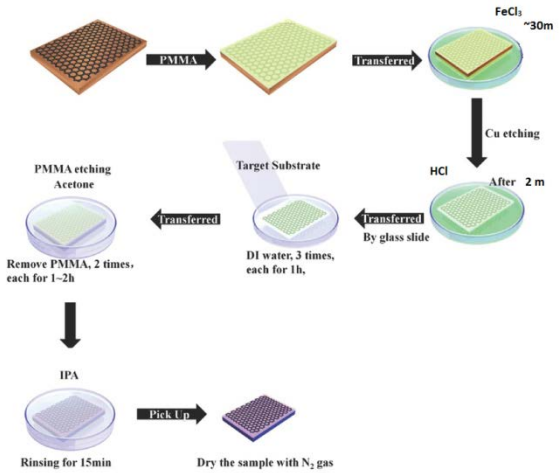

Figure 2. Schematic of a CVD graphene transferred on a target substrate.

3.2 Graphene grown on copper

3.2.1 Introduction

As I said before, copper is one of the most common metal substrates used for graphene growth by CVD. Its low carbon solubility helps to limit the graphene growth on it, since graphene only grows on copper by deposition. This subchapter will mainly focus on the necessary conditions to achieve single layer graphene in order to use it for electronic devices. Moreover, a method will be proposed to study the number of graphene layers and the stacking order by ARPES which is complementary to micro-Raman spectroscopy, since the number of layers' estimation is not possible by the usual Raman measurements. As mentioned before, in this series of experiments methane was used as the carbon source.

3.2.2 Graphene on different copper substrates

The copper substrate is placed in the reactor chamber, in our case inside the susceptor to achieved an homogeneous temperature around it, and then heated at a certain temperature that permits copper to catalyze the methane when the gas gets in touch with the metal. The reaction that occurs is

$$Cu(bulk) + CH_4 \leftrightarrows C_{atoms} + H_2 \quad (3.1)$$

The temperature needed to catalyze methane on copper is 900°C but in order to achieve a better quality this temperature could be increased, keeping in mind not to exceed the melting point of copper which is 1084.62°C.

For transfer purposes it is better to grow graphene on copper thin film or copper foils. Monocrystalline bulk copper (111) is used only to characterize graphene by ARPES due to the well ordered graphene growth on it, as will be described below. To emphasize the difference of the graphene growth on different types of copper substrates, the same starting point process was applied on: a Cu thin film of 2μm deposited on a 300 nm SiO_2/Si wafer, a copper foil (99.5%, Alfa Aesar) 25μm and on bulk Cu (111) (Alfa Aesar).

The growth process was similarly set as indicated in **Figure 1**. The temperature of the annealing step that cleans the copper surface is set to 900°C during 10 minutes at atmospheric pressure, which is reached with an argon (Ar) flow rate of 1000 sccm. In this step, are also used 10 sccm of H_2 to help clean the native oxide of the copper that could block the catalysis and the graphene growth. The growth temperature is set at 950°C to assure the proper catalysis of the methane. The growth process is performed at atmospheric pressure, using 1000 sccm of Ar and 35 sccm of methane as a carbon source during 15 minutes. Hydrogen has not been used in the growth step to keep the carbon atom production low. Since copper has low carbon solubility, the cool down does not play an important role and the sample was cooled naturally ($20°C/s$) to room temperature, at atmospheric pressure, with a continuous flow of Ar.

After growth the samples were characterized by micro-Raman spectroscopy using an Ar+ laser with a wavelength of 514.4nm and a laser power of 1 mW with an objective lens of 100x. In **Figure 3** are presented the characteristic Raman spectra of graphene on the different substrates mentioned before. The background was subtracted from all spectra to better analyze the characteristic peaks of graphene.

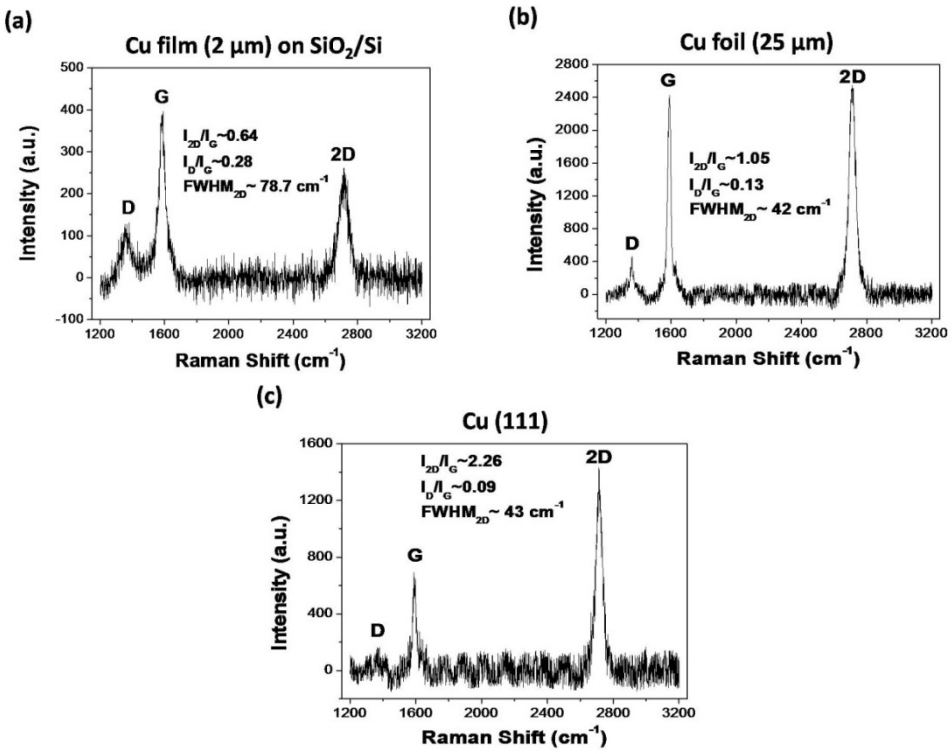

Figure 3. Raman Spectra of Graphene on (**a**) Cu film (2µm) on SiO2/Si, (**b**) Cu foil (25µm) and (**c**) bulk Cu (111) for the same growth conditions.

The graph on **Figure 3 (a)** corresponds to non-AB stacked few layers graphene on Cu film. The ratio $\frac{I_{2D}}{I_G} \sim 1.14 < 2$ with a $FWHM_{2D} \sim 64\ cm^{-1}$ could belong to AB-stacked few layers graphene, but the analysis with the number of lorentzians that can be used to fit the 2D peak clearly fits only with a single Lorentzian, so the only possibility is that this sample belongs to non-AB stacked graphene. The ratio between the intensity of the D peak and the intensity of the G peak, which is relative with the density of defects in the lattice near the measurement, is $\frac{I_D}{I_G} \sim 0.26$ which is noticeable. As will be mentioned below, it is possible to achieve graphene by CVD with no evidence of D peak.

The graph on **Figure 3 (b)** corresponds to graphene on Cu foil. The ratio $\frac{I_{2D}}{I_G} \sim 1.05 < 2$ with a $FWHM_{2D} \sim 42\ cm^{-1}$ besides the analysis of 2D peak which can be fitted with a single Lorentzian is sufficient to estimate that the sample belongs to non-AB stacked graphene. Now the $\frac{I_D}{I_G} \sim 0.13$ is smaller than that of the Cu film. In principle, this is something that can be expected since the surface of Cu foil is normally smoother and with larger grains than the Cu film. However, Cu films are of our interest because they can macroscopically offer less rough surfaces than Cu foils.

Finally, the Raman spectrum of graphene on bulk Cu (111) is presented in the graph on **Figure 3 (c)**. In this case, it has a ratio $\frac{I_{2D}}{I_G} \sim 2.26 > 2$ but with a $FWHM_{2D} \sim 43\ cm^{-1}$ which corresponds again to a non-AB stacked few layers graphene. Now the analysis of the 2D peak would not reveal something of interest due to the fact that both single layer graphene and non-AB stacked graphene are fitted with a single. The key here is that the FWHM of the 2D peak is wider than the expected for a single layer graphene, even for graphene on a copper substrate. As it is expected graphene on bulk Cu (111) presents the lowest intensities' ratio between the D and the G peaks with that being $\frac{I_D}{I_G} \sim 0.09$.

According to the findings above, it is demonstrated how important the substrate is in the quality of the graphene. In spite of the better results for bulk Cu (111), this kind of substrate is not suitable for transfer so it will be used only to characterize graphene by ARPES. Potentially, Cu film as well as Cu foil are substrates suitable to grow graphene for transfer and for that reason they will be both studied for different conditions. By adjusting the different parameters of the process, we can achieve low defective single layer graphene, as will be analyzed further below.

3.2.2.1. Decrease of the methane flow rate

The initial recipe, used above to show the difference between the different substrates, is easy to be improved. Starting with the annealing step, the recipe can be improved by increasing the temperature of the annealing which can be set at 950°C, still far from the melting point. With this increment it is expected an improvement at the grains' size and a smoother surface. The duration of the annealing can also be changed, but it was not observed any difference for periods of more than 10 minutes.

Additionally, further improvements can be made in the growth step. Temperature can be changed in this step, as it did in the previous one. A higher temperature can help to catalyze methane better with a larger amount of sp2 carbon bonds than lower temperatures. At this point the temperature was set at 1000°C, which is still reasonably far from the melting point. Regarding the duration, the growth step has been split in two. A first sub-step has a low methane flow rate and a short duration, and the second one with a larger amount of methane and a longer duration. It is known that graphene on copper growth starts from nucleation points, which are usually arisen on surface steps and grain boundaries where the carbon atoms' adsorption is energetically favorable. After these nucleation points are formed, the new carbon atoms that have been catalyzed tend to bond with them. Thus, the graphene sheet grows from these sites. The aim of this first sub-step is to decrease the density of these nucleation sites so that a lower amount of carbon is deposited on the metal surfaces. Moreover, the carbon atoms created in the

second sub-step tend to bond with the carbon atoms that already form the nucleation points. This, together with the reduction of the grain boundaries during the annealing, will help to grow larger graphene domains and therefore less defective. Furthermore, during the second sub-step a reduction of the amount of methane is also expected to reduce the amount of carbon available in the chamber.

In order to specify the effect of the methane's flow rate reduction into the chamber, the following experiment was carried out. The growth temperature. the duration of the growth step and the argon flow rate (1000 sccm) were held constant while all the samples were prepared with different flow rates, as shown in **Table 1**. The methane flow rate was initially set at 35 sccm and kept reducing until 20 sccm where no graphene growth was observed.

		Duration (minutes)	Temperature (°C)	H_2 (sccm)	Ar (sccm)	CH_4 (sccm)
annealing		10	950	10	1000	0
growth	a	2	1000	0	1000	10
	b	10	1000	0	1000	x

Table 1. Graphene growth conditions for different methane concentrations.

Raman spectroscopy was applied for the characterization of the grown graphene before and after the transfer onto a SiO_2 (300nm)/Si**.** In **Figure 4** are presented the Raman spectra for graphene grown on Cu film for methane flow rates of (**a**) 35 sccm, (**c**) 30 sccm and (**e**) 25 sccm. Since no growth was achieved for 20 sccm methane flow rate, no graph for this case is shown. In the same figure are presented the Raman spectra for the relative graphene transfer on silicon dioxide, (**b**) 35 sccm, (**d**) 30 sccm and (**f**) 25 sccm respectively.

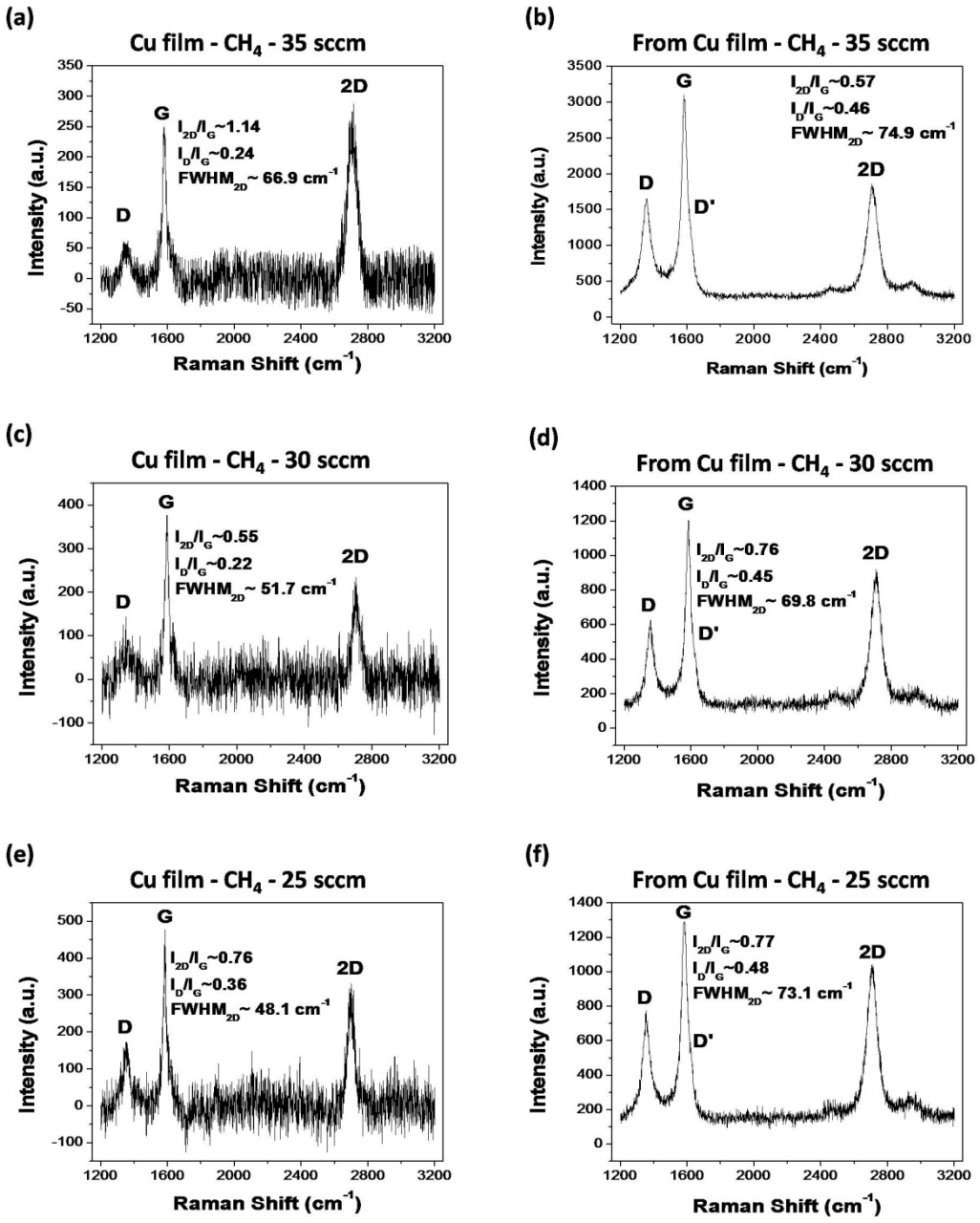

Figure 4. Raman spectra after growth for (**a**) 35sccm, (**c**) 30sccm and (**e**) 25sccm. Raman spectra after transfer for (**b**) 35sccm, (**d**) 30sccm and (**f**) 25sccm.

Graphene can grow on Cu film until a methane flow rate of 25sccm, with the argon flow rate fixed at 1000 sccm, as it was concluded after this series of experiments. Below this value graphene did not grow due to the low methane partial pressure

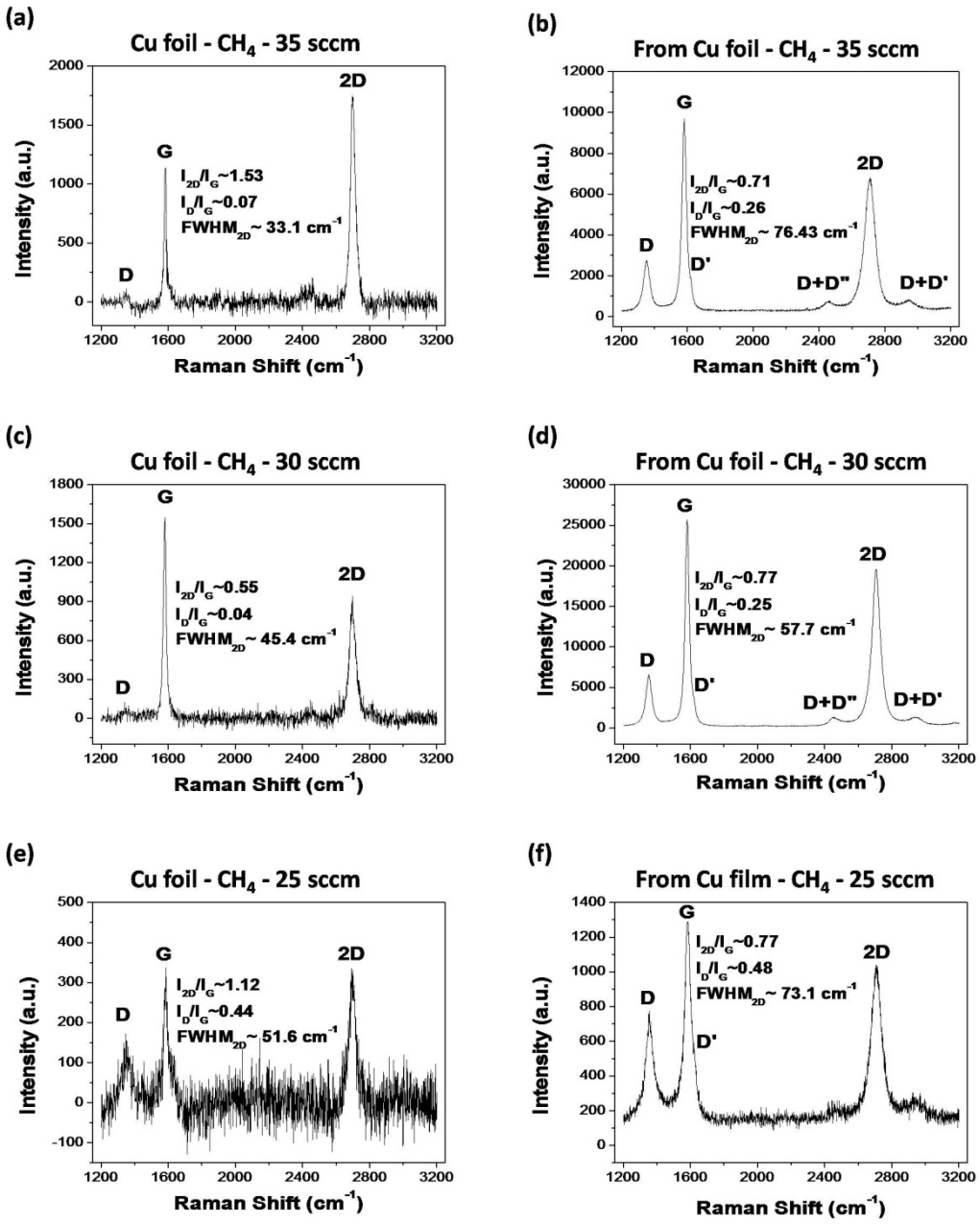

Figure 5. Raman spectra of graphene grown on Cu foil for (**a**) 35sccm, (**c**) 30sccm and (**e**) 25sccm and their transfer onto silicon dioxide substrates, (**b**), (**d**) and (**f**), respectively. Graphene growth was not observed for a 20 sccm methane flow rate, for the same reasons the same thing happened in the case of Cu film.

This set of experiments led us believe that the methane flow rate cannot be reduced below 25 sccm, maintaining the argon flow rate constant, for the graphene to grow on copper. It can be also observed that except for the 25sccm, an improvement of the

graphene growth was achieved due to the higher temperature used during the annealing and the growth step in relation to the initial recipe. However, even for the smallest amount of methane used, single layer graphene was not achieved as it can be seen in the Raman spectra. All Raman spectra were well-fitted by a single Lorentzian and both the $\frac{I_{2D}}{I_G}$ ratio and the $FWHM_{2D}$ differ from the respective values of a single layer graphene ($\frac{I_{2D}}{I_G} > 2$ and $FWHM_{2D}$<39 cm^{-1}). Furthermore, it was noticed that the graphene growth was all together better on copper foil than on copper film when the initial recipe and the new one are compared. Moreover, the improvement of the initial recipe itself has been better demonstrated in the case on the copper foil in relation to the copper film.

The higher D peak observed in figure 5 (e), corresponding to 25 sccm, could be explained by the incomplete catalysis that results from this low partial pressure. A large amount of carbon atoms must still have bonds with some hydrogen atoms and that leads to an increment of the number of the sp3 bonds. It is worth noticing that the higher D peak was present even before the transfer onto the SiO_2.

The transfer of the graphene onto the SiO_2 surface was similarly performed to the one described in **Figure 2**, although a thermal tape was used instead of PMMA and the HCl step was not used to clean the film of the $FeCl_3$ residues either. Due to the transfer process, many defects and cracks were induced in the graphene, as seen in figures 5(b), 5(d) and 5(f). We can clearly notice an increment of the D peak as well as the appearance of the D' peak which is relative to the presence of graphene edge. As a result, some improvements in the transfer method will be attempt in the next experimental series.

3.2.2.2. Decrease of both methane and argon flow rates

Since there was no single layer graphene growth observed for the lowest amount of methane flow rate (25sccm) tried yet, the next attempt involved a further reduction in the methane flow rate keeping constant the partial pressure of methane, ergo reducing the argon flow rate (table 2). This modification aimed to allow the catalysis to develop properly.

		Duration (minutes)	Temperature (°C)	H_2 (sccm)	Ar (sccm)	CH_4 (sccm)
annealing		10	950	10	1000	0
growth	a	2	1000	0	1000	10
	b	10	1000	0	y	x

Table 2. Graphene growth conditions for different methane/argon ratios.

The reduce of the methane and argon flow rates was meant to keep their ratio constant at $\frac{x}{y} = 0.035$. Raman spectroscopy was applied for the characterization of the grown graphene before and after the transfer onto a SiO_2 (300nm)/Si, as it can be seen on figure 6.

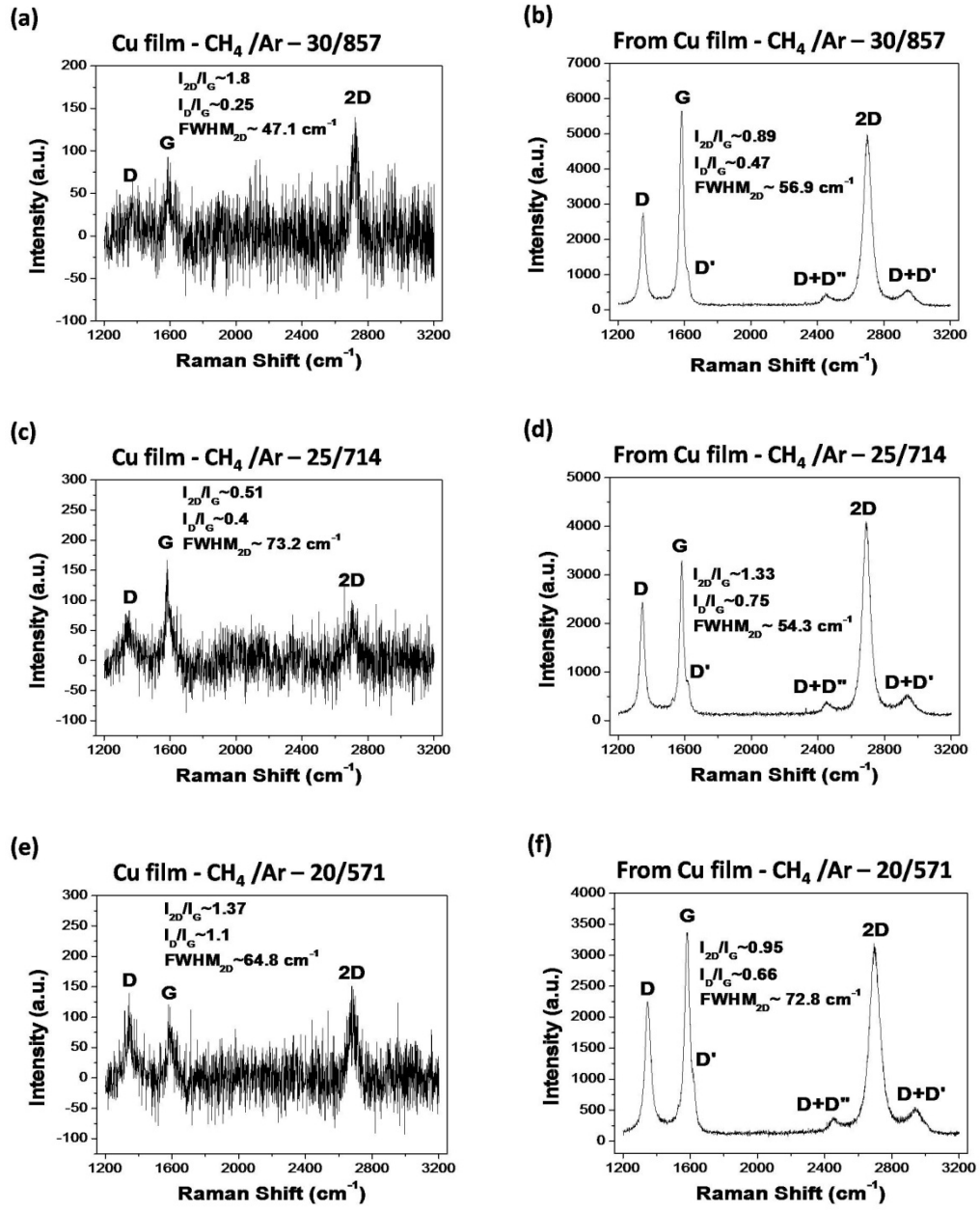

Figure 6. Raman Spectra of graphene grown on Cu film for CH_4/Ar (**a**) 30/857, (**c**) 25/714 and (**e**) 20/571. Graphs (**b**), (**d**) and (**f**) correspond to the respective graphene transferred to SiO_2.

Graphene growth was achieved for 20sccm of methane when the respective argon flow rate was 571sccm, equal to a ratio of 0,035. However, when the same ratio was kept with

a methane flow rate of 15sccm and a argon flow rate of 428sccm, graphene failed to grow. It is worth mentioning that similar results were achieved when the same experiment was conducted for copper foil substrates (**Figure 7)**.

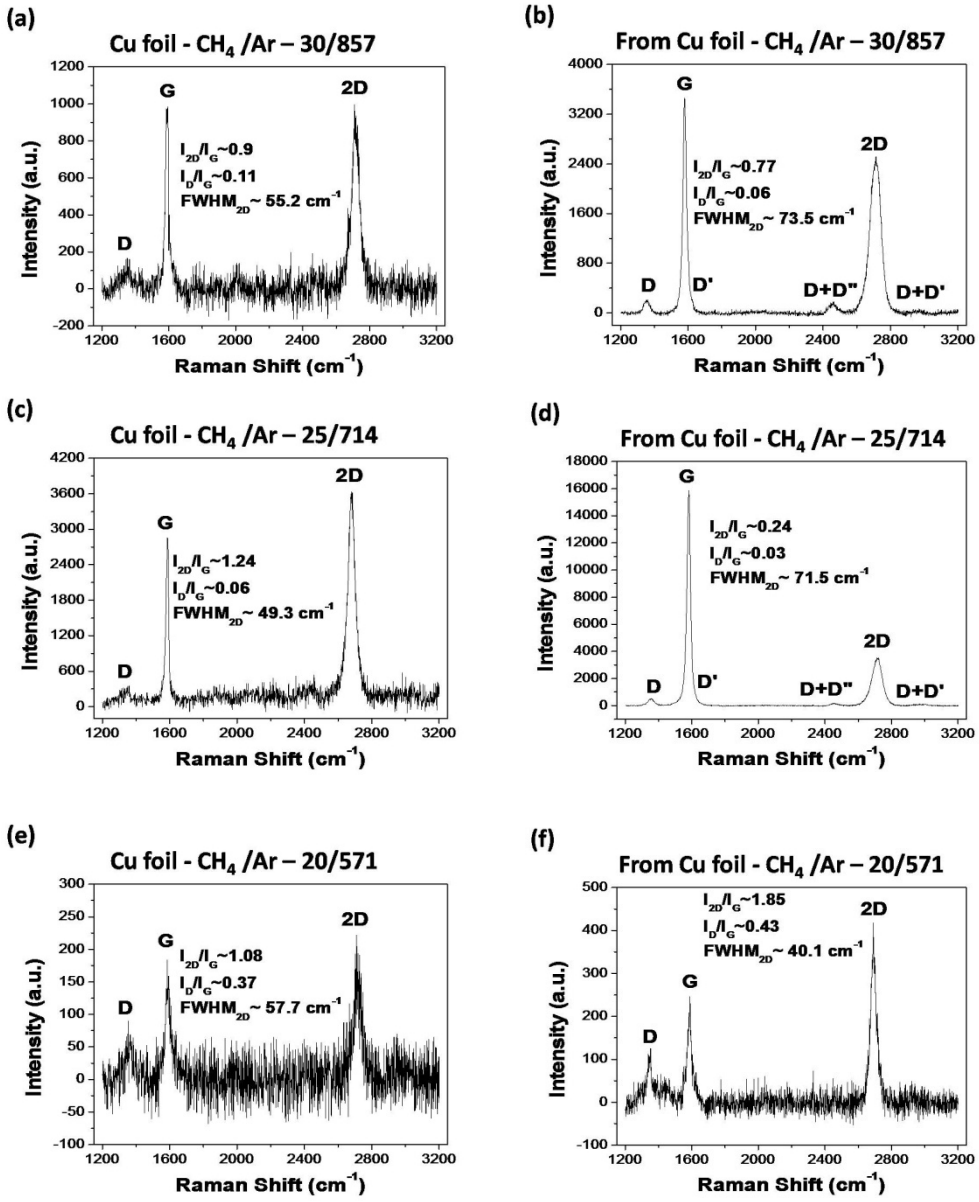

Figure 7 Raman Spectra of graphene grown on Cu foil for CH_4/Ar (**a**) 30/857, (**c**) 25/714 and (**e**) 20/571. Graphs (**b**), (**d**) and (**f**) correspond to the respective graphene transferred onto SiO_2.

In this set of experiments characterized by a further reduction of the methane flow rate, single layer graphene was not achieved and no significant improvement of the graphene quality was observed, as it can be seen in the Raman spectra. However, some

improvement was achieved regarding the quality of the transfer mainly by the use of PMMA instead of thermal tape, the introduction of the HCl step for the cleaning of the $FeCl_3$ residues and the better rinsing of the sample on every step of the process.

The most remarkable advance was achieved during the transfer from copper foil and it is interesting to note that transfer from copper film was generally more difficult than from copper foil, during all sets of the experiments. Regarding the presence of the D peaks, it is clear from the Raman spectra that the ones of **Figure 7** are lower than those of **Figure 6**, a fact that supports the easiest transfer capacity from copper foils. Additionally, we can observe from the Raman spectra that the D peaks of **Figure 7** are lower than those of **Figure 5**. Furthermore we can see that in **Figure 7** the D' peaks are far lower than those of **Figure 5**. Both facts suggest that there has been an improvement of the transfer method throughout the experiments.

Conclusively, there are some main points coming from the present experimental results that need to be underlined. First of all, it could be safely stated that only the reduction of the methane flow rate is not enough a measure in order to achieve growing single layer graphene. Furthermore, such a reduction is not always good for the quality of the graphene. Secondly, it should be noted that copper foil was proved a better substrate not only for the growth but also for the transfer of the graphene as well.

As a matter of fact, as growth temperatures rise close to the melting point of copper, copper evaporates from the sample surface. Although this fact occurs with both copper foil and copper film, for the latter this effect is crucial because the evaporation leaves voids in the surface of the copper film, as **Figure 8** shows. This is another serious drawback regarding the use of copper film for graphene growth and thus in the next experiments only copper foil was used.

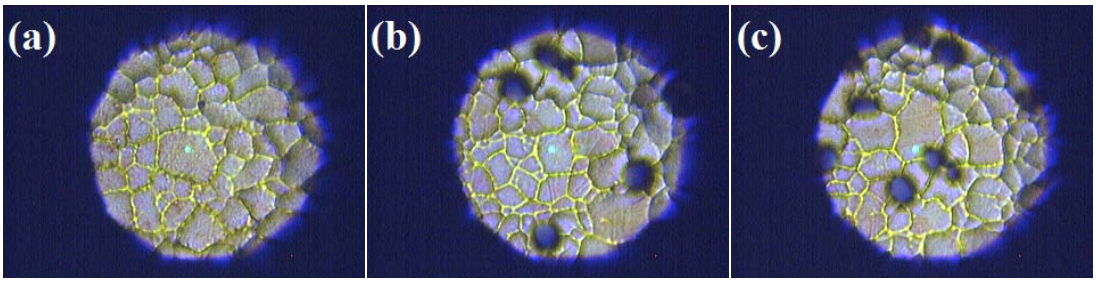

F**igure 8** Images of copper film taken through optical microscope for increasing growth temperatures: (**a**) 950°C, (**b**) 1000°C and (**c**) 1030°C.

3.2.2.3. Adjustment of the growth duration

To achieve good quality single layer graphene transferred onto a dielectric, a new set of experiments with the growth duration as the main variable parameter, were carried out.

The duration of the second growth sub-step was initially set to ten minutes and was being reduced until a large coverage of single layer graphene was achieved. The growth duration that gave the best results was that of two minutes. However some interesting notes were made until this result was achieved, most important of those being that despite that some single layer areas were achieved even for a duration time of 5 minutes, the duration had to be reduced to two minutes for the metal surface to have a large percentage of single layer graphene.

		Duration (minutes)	Temperature (°C)	H_2 (sccm)	Ar (sccm)	CH_4 (sccm)
annealing		10	950	10	1000	0
growth	a	2	1000	0	1000	10
	b	x	1000	0	1000	30

Table 3. Growth conditions varying the duration of the growth step b.

All the other parameters of the experiment were fixed to the best result achieved until this moment (CH_4/Ar ratio of 30/1000) except for the annealing temperature which was increased to 975°C as a new attempt to improve the substrate.

Raman spectroscopy was applied for the characterization of the grown graphene before and after the transfer onto a SiO_2 (300nm)/Si, as it can be seen above on **Figure 9**.

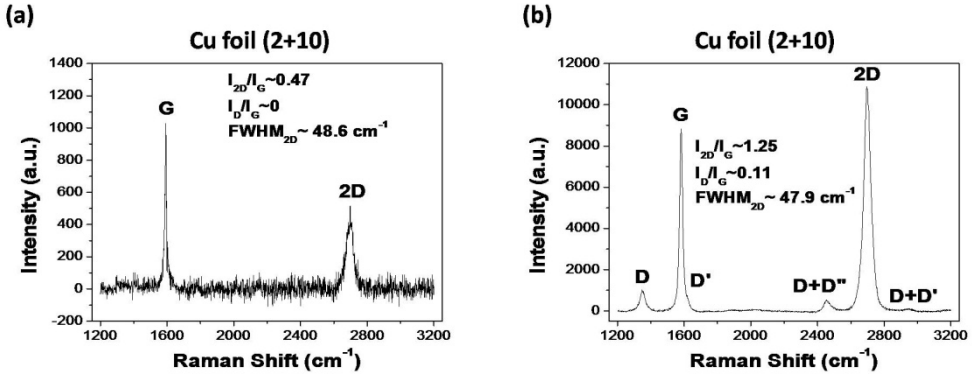

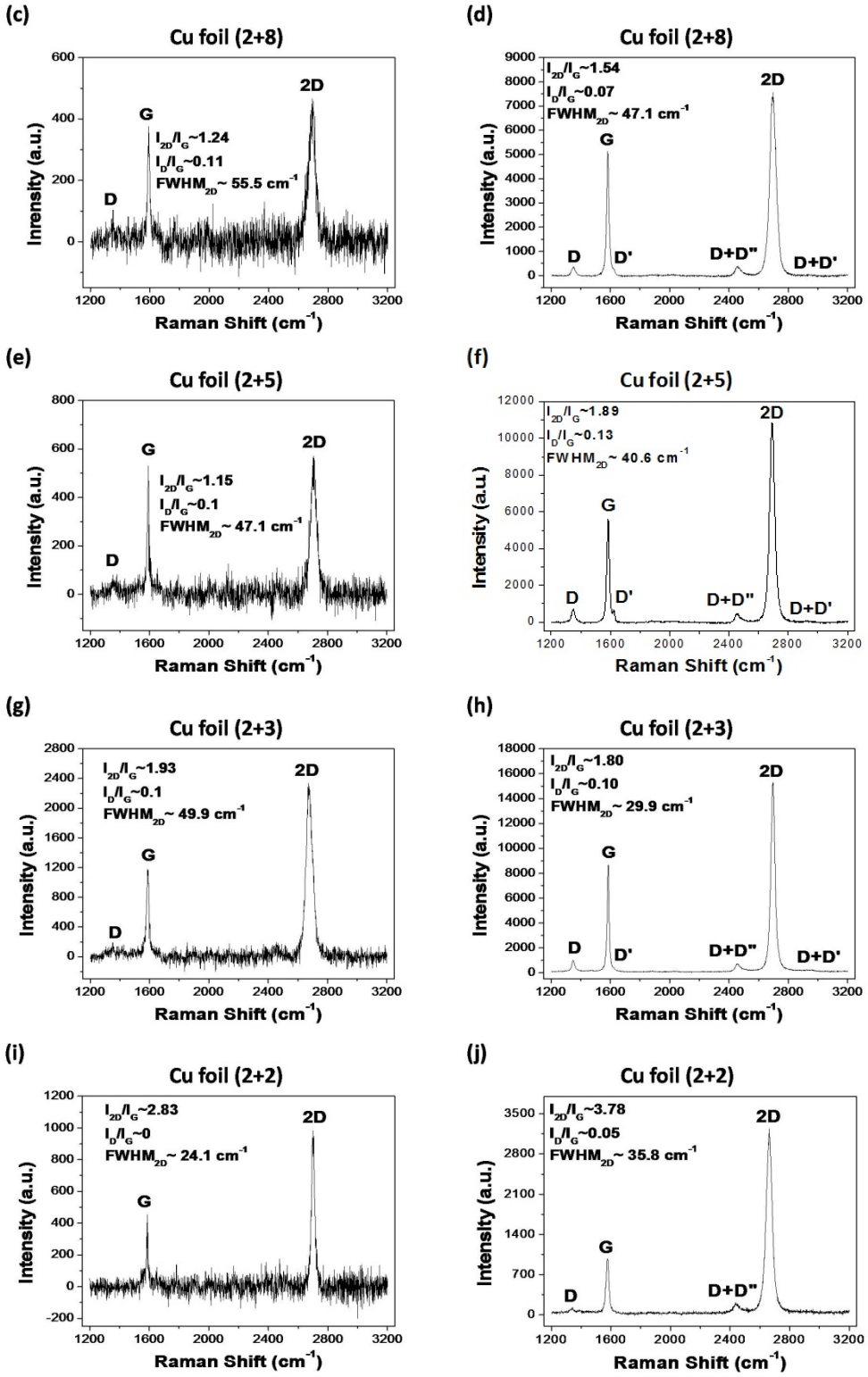

Figure 9. Raman Spectra for different durations of the second growth step. (**a**) 10 min, (**c**) 8 min, (**e**) 5 min, (**g**) 3 min and (**i**) 2 min. . Their respective Raman spectra after the transfer on SiO_2 are (**b**), (**d**), (**f**), (**h**) and (**j**) respectively.

Observing the spectra of **Figure 9(i)** where the second growth sub-step has been 2 minutes it can be clearly concluded that single layer graphene is present since both the $\frac{I_{2D}}{I_G}$ ratio and the $FWHM_{2D}$ do not differ from the respective values of a single layer graphene ($\frac{I_{2D}}{I_G} > 2$ and $FWHM_{2D}$<39 cm^{-1}) and the 2D peak was well-fitted by a single Lorentzian. The mono-layer graphene presence was also confirmed by the spectra of **Figure 9(j)** that corresponds to graphene after its transfer on SiO_2.

The results of this set of experiments led us to conclude that large areas of single layer graphene can be achieved by reducing the duration of the second growth step down to 2 minutes whilst the increase of the temperature of the annealing step seems to result successfully. Raman spectra clearly confirm that both the growth step as well as the transfer of the graphene were all together improved, as the D peaks are absent or very low in the majority of the samples.

Once the good quality single layer graphene on SiO_2 was achieved, the building of electronic devices with graphene could be realized and it is presented on Chapter 4.

3.2.3 Non AB-stacked graphene characterization

Raman spectroscopy, as it has been shown, is a powerful tool to characterize graphene. Using it makes it easy to detect single layer graphene on different kind of substrates while it can also give us an estimation about its quality. The presence and the height of the D and D' peaks stand for point defects and deformation in the lattice, whereas the width of G and D peaks can give information about the sp3 bonds that can be originated from residues attached to the graphene layer.

The determination of graphene stacking order can also be revealed by Raman measurements. Basically Raman can discern between AB stacking (or Bernal stacking) and non-AB stacking graphene (arbitrarily twisted layer graphene). The AB stacking, which is the stacking order of graphite, is the most favorable configuration for graphene layers. Under this stacking the interlayer interaction becomes stronger relatively to other stacking orders and it is reflected on the Raman spectrum of the few layer graphene, as it was previously described. However, the estimation of the number of layers by Raman spectroscopy becomes hard when the stacking order differs from the AB stacking. Thus, for non AB stacked graphene complementary characterization techniques are needed. Using ARPES characterization method, the energy bands of the graphene can be imaged giving information about the number of layers and their doping from the substrate.

Arbitrarily twisted layer graphene is not so rare. A random angle distribution of rotation angles results in the so called turbostratic graphene, which is the building block of several forms of highly disordered graphite. Graphene grown by Chemical Vapor Deposition (CVD) on copper substrates is mainly in this form. Twisted graphene with commensurate angle is not so easily obtained, often prepared by transferring [**26, 27**] one layer of graphene on top of another. Alternatively, using suitable substrates, one can influence the stacking order as for example in the case of Si-face SiC substrate [**28**] , where bilayer epitaxial graphene can be typically obtained in the AB stacking arrangement corresponding to a 60° rotation between the layers and with a modified Dirac cone due to interlayer coupling. On the other hand, on a C-face SiC substrate, twisted multilayer graphene can be obtained behaving as a set of independent graphene layers with no interlayer interaction [**28**].

Single crystal (111)-oriented transition metal substrates [**29**] often used for the catalytic growth of graphene by CVD offer a suitable template to produce highly ordered graphene layers. Ni, Rh, Ru interact strongly with graphene modifying the electronic structure which is not desirable for this study. Cu(111) on the other hand is an interesting case since it interacts weakly with graphene offering the prospect for a well oriented graphene multilayer without undesirable influence from the substrate.

Graphene is prepared by CVD method on Cu(111) bulk catalyst substrates using methane as the carbon source. The substrate was heat-up to a temperature of 900°C with 5°C/s ramp-up rate at low pressure of 8 Torr under a flow of 10 sccm H_2. Once the temperature was reached, the sample was annealed at the same atmospheric condition than the heat-up during 20 minutes. After that, graphene was grown using a constant methane flow rate of 35 sccm during 30 minutes. Finally, the sample was cooled down until temperature reached 250°C holding the 35 sccm of methane and the 10 sccm of H_2.

Raman spectroscopy was applied for the characterization of the grown graphene. For the micro-Raman measurements, a triple monochromator in subtractive mode was used, with optical microscope of magnification up to 100x, and a liquid nitrogen cooled CCD detector. The system is equipped with motorized stepping drive motors for the scanning of the sample area. For this series of measurements, an excitation Ar^+ laser beam, at 514.5 nm, with power of 1 mW, was used, in order to minimize heating effects.

Typical Raman spectra taken from different locations on the substrate (**Figure 10**) generally show an inhomogeneous layer. Graphene layers have few or no defects at all, depending on the location on the substrate as indicated by the D peak in **Figure 10 (a)**. The top spectrum in **Figure 10 (a)**, representative of about 25% of the measured area, is characteristic of monolayer graphene, as it can be inferred from the relatively high

I2D/IG (>2) ratio and the sufficiently low ($< 40cm^{-1}$) full width at half maximum ($FWHM_{2D}$) of the 2D peak (**Figure 10 (b)**). The middle and bottom spectra of **Figure 10 (a)** showing large ($> 40cm^{-1}$) $FWHM_{2D}$ (**Figure 10 (c)** and **(d)**) are indicative of few (non-interacting) layer graphene in non-AB stacking arrangement and they are representative of the largest portion (75%) of the measured area.

Standard analysis is based on the 2D peak line shape and position and the I2D/IG ratio for an estimate of the number of layers, however, newer evidence [**30**] suggests that Raman signal characteristics do not only depend on the number of layers but also on the twist angle, the stacking order, and eventually, the interlayer interaction. According to this reference [**30**], the dependence of the 2D Peak frequency and the FWHM on the twist angle is non-monotonic for interacting layers, while the integrated intensity is monotonically dependent on the twist angle. Since the Raman integrated intensity is a quantity very sensitive to the experimental conditions, the assignment of a single rotation angle between the two graphene layers by means of the Raman characteristics, should be cross-checked by an independent method, able to distinguish between interacting or independent layers, especially in graphene directly measured on Cu, where sufficient data are lacking. As shown below, ARPES provides additional information complementing Raman for the purpose of estimating the number of layers and drawing conclusions about the interlayer coupling.

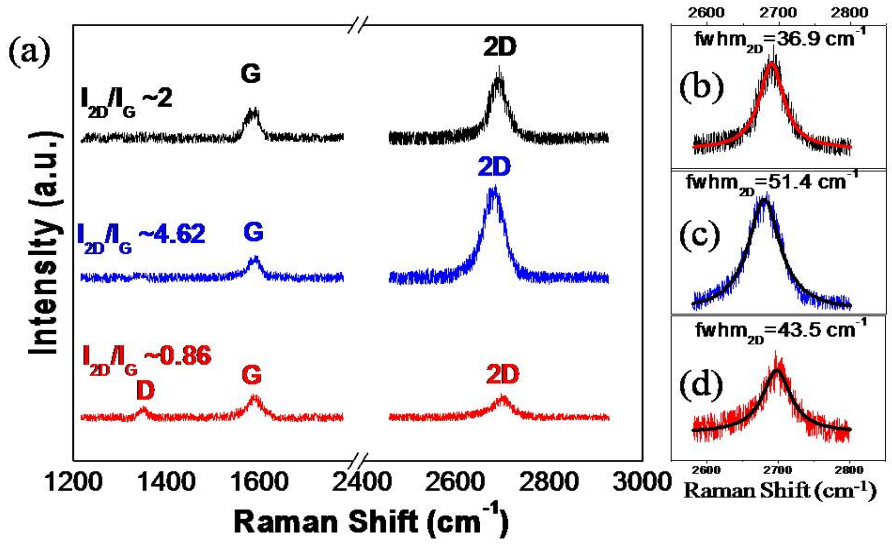

Figure 10. (**a**) Three representative Raman spectra of graphene on copper measured on our sample. The top spectrum is characteristic of single layer graphene, and the middle and bottom spectra are indicative of few layer non-AB stacked graphene. (**b**)–(**d**) 2D peak detail and corresponding single Lorentzian fitting curves for single and few layer graphene, respectively.

The sample was also characterized by RHEED, the results are shown in **Figure 11**. The RHEED diffraction pattern of Bare Cu at **Figure 11 (a)**, and for graphene on copper at **Figure 11 (b)**, both for the $\bar{1}\bar{1}2$ direction. The diffraction pattern of Cu, is marked with the red arrows and the corresponding pattern of graphene is marked with the solid blue arrows. Marked with the dashed blue arrows two of the four streaks that belong to a 30^0 or 90^0 rotated pattern of graphene. Since we can see these two patterns of graphene in the $\bar{1}\bar{1}2$ direction we can conclude that we have graphene rotated domains in our sample.

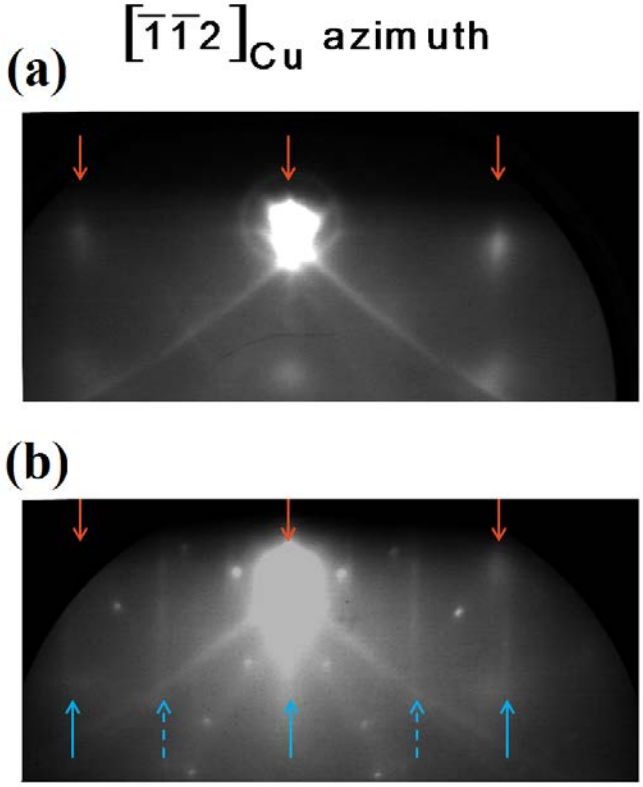

Figure 11. (**a**) The RHEED diffraction pattern of Bare Cu and (**b**) for graphene on copper, both for the $\bar{1}\bar{1}2$ direction.

The electronic band structure of graphene on Cu(111) was studied by ARPES in a μ-metal analytical chamber at room temperature using a 100 mm hemispherical analyzer equipped with a 2D CCD detector. The total energy resolution of the system was better than 40 meV. The excitation was made by a He–I source with 21.22 eV photon energy. For each azimuth angle φ of the sample, the polar angle θ varied from 0° to 80° with step angle of 1° and tilt window of 29.5°. Measurements were made for five different azimuth angles φ covering total azimuth range of 120°. The sample was introduced in the UHV system immediately after the CVD growth and annealed at 420°C for 5 min prior to ARPES measurements.

The energy dispersion of graphene on Cu(111) along the $\overline{\Gamma K}$ direction of Cu(111) obtained by ARPES is given in **Figure 12**. On top of the Cu d bands with a weak dispersion, the linear strongly dispersing π bands of graphene are faintly visible crossing at the $\overline{K}$ point of graphene around 1.703 $Å^{-1}$ and near E_F forming the Dirac cone. In addition, a brighter highly dispersing band is the π band along $\overline{\Gamma M}$ direction of graphene peaking at $\overline{M}$ point ~1.47 $Å^{-1}$ and $E_B \sim -2.9\ eV$ indicating 30° rotational domains in agreement with Reflection High Energy Electron Diffraction (RHEED) data that we have showed before.

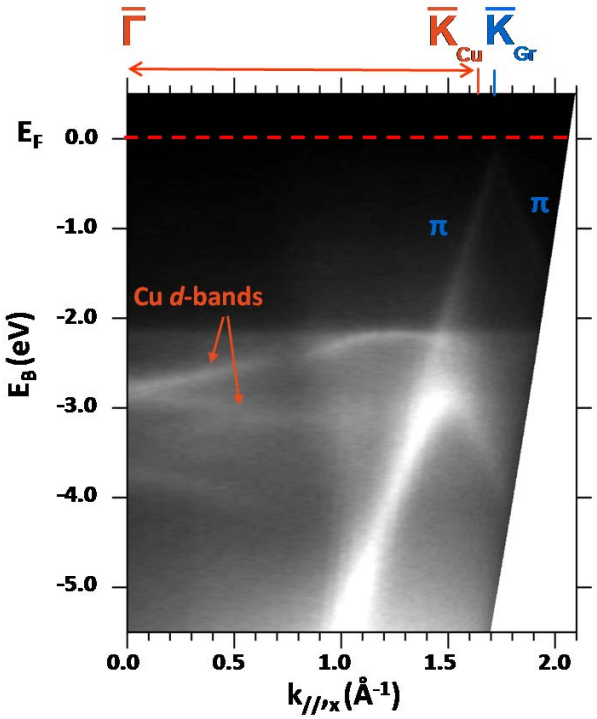

Figure 12. Electronic band structure ARPES imaging of Graphene/Cu(111) along the $\overline{\Gamma K}$ direction of Cu(111) surface Brillouin zone (SBZ). The faint bands crossing near E_F at the $\overline{K}$ point of graphene (1.703 $Å^{-1}$) are attributed to the π-bands of graphene forming a Dirac cone, which is characteristic of their linear dispersion along $\overline{\Gamma K}_{grap\ hene}$ direction, indicating alignment with the $\overline{\Gamma K}_{Cu}$. The band presenting a maximum at $-2.9\ eV$ and k_x~1.47 $Å^{-1}$ ($\overline{M}$ point of graphene) is attributed to the π-band of graphene dispersing along $\overline{\Gamma M}_{grap\ hene}$ direction, which is visible here due to the presence of 30° rotational domains.

By probing a larger portion of the k-space as seen in the constant energy contour plots $k_x - k_y$ at 0.18 eV below the Fermi surface as it is shown in **Figure 13**, a less ideal

situation is observed. The circular bright traces at ~1.703 $Å^{-1}$ from the center are formed by the projection of the Dirac point (DP) on the $k_x - k_y$ space spreading essentially over all azimuthal angles and indicating a polycrystalline material.

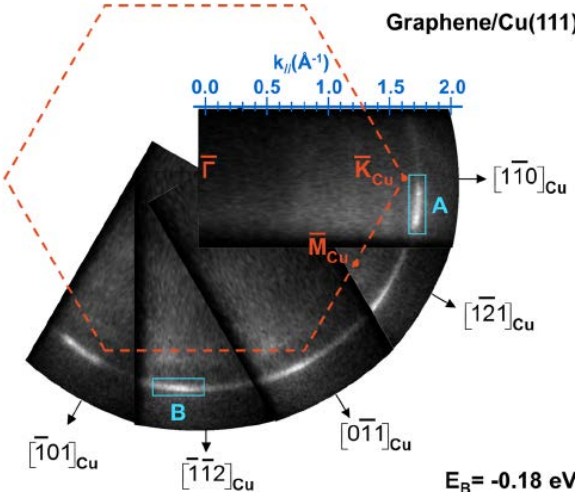

Figure 13. APRES constant energy contour $k_x - k_y$ of Graphene/Cu(111) near Dirac cone apexes ($E_B = -0.18\ eV$). Cu(111) SBZ is indicated by the dashed hexagon. $\overline{\Gamma}$, $\overline{K}_{Cu}$ and $\overline{M}_{Cu}$ symmetry points of the SBZ are also shown. The ring-like bright trace at $k_{\parallel}$~1.7 $Å^{-1}$ is attributed to randomly oriented domains of polycrystalline graphene. A signal enhancement near $\overline{K}_{Cu}$ (area A marked by rectangle) indicates a preferential in-plane alignment of graphene with Cu(111) SBZ.

Note however that near the $\overline{K}$ points of Cu(111), there are small brighter sections of graphene k-space, marked by rectangle A. Bright sections (although not as bright as in the A regions) marked by B are also seen along the $\overline{\Gamma M}$ direction of Cu due to 30° rotational domains as noted above when discussing the **Figure 12**. The detailed structure of the selected k-space region A is clearly visible in the contour plot detail obtained at $E_B = -0.5\ eV$ seen in **Figure 14 (a)**. In this figure, three circular features are imaged corresponding to the projections of three distinct cones on the $k_x - k_y$ plane rotated to each other by about 4°. More precisely, cones 1 and 2 are rotated by $\theta_{12} = 4.64°$ and cones 2 and 3 by $\theta_{23} = 3.93°$. We attribute these observations to the Dirac cones of three different, non-interacting, graphene layers placed one on top of the other and rotated to each other by about 4°. Remarkably, θ_{12} and θ_{23} are near the commensurate rotation angles 4.4° and 3.89° obtained from

$$\cos\theta = \frac{(4mn + n^2 + m^2)}{2(m^2 + n^2 + mn)} \quad (3.2)$$

for (m,n) pairs equal to (8,7) and (8,9), respectively [**31,32]**.

It is important to note that the cone structure is not resolved in the bright B areas of k-space (**Figure 13**) at $E_B = -0.5\ eV$; rather a diffused intensity is observed, probably as a result of the increased rotational disorder of graphene domains alongside the $\overline{\Gamma M}$ direction of Cu.

The three-cone picture claimed in the $k_x - k_y$ plot in **Figure 14 (a)** is further supported by the energy dispersion along k_y shown in **Figure 14 (b)**, where three Dirac cones are clearly observed despite the limited resolution due to large thermal line broadening ($\sim 110\ meV$) at room temperature. However, the cut along k_y in **Figure 14 (b)** is made through a circular arc rendering the direct comparison of the three cones difficult. The Dirac cones are better resolved by plotting the cut for each one of them along a diameter as shown in **Figure 14 (c)**. The bands vary linearly with $k_{\|}$, crossing only 0.1–0.15 eV below the EF while there is eventually no gap at the DP. The position of the DP slightly below E_F is an indication of n-type doping from the substrate [**33,34**].

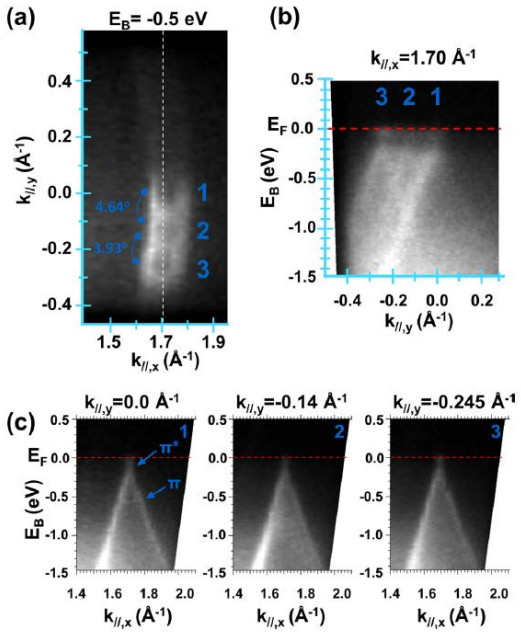

Figure 14. (**a**) Details of the APRES constant energy contour $k_x - k_y$ of Graphene/Cu(111) at $E_B = -0.5\ eV$, showing three Dirac cones at $k_x \sim 1.7$ Å^{-1}. Cones 1 and 2 are rotated by $\theta_{12} = 4.64°$ and cones 2 and 3 by $\theta_{23} = 3.93°$. Each cone corresponds to a respective rotated graphene layer. (**b**) Energy dispersion along the $k_{\|,y}$ direction marked by the dashed line in (**a**) for fixed $k_{\|,x} = 1.70$ Å^{-1}. Three Dirac cones are observed at different $k_{\|,y}$ positions. (c) Energy dispersion along the $k_{\|,x}$ direction of the three cones. Each image shows a cut along the diameter of each cone at $k_{\|,y}$ values 0.0 Å^{-1}, -0.14 Å^{-1}, and -0.25 Å^{-1}for cones 1, 2 and 3, respectively. The Dirac point is located at ~ -0.1 to 0.13 eV from E_F.

The nearly ideal Dirac cone indicates that the Cu substrate has little or no influence on the electronic band structure of graphene. The Fermi velocity v_F estimated from the slope of the linearly varying p-bands near the Fermi surface is found between 1 and 1.2×10^6 $m/_S$, very close to the ideal value of free-standing graphene. This is an indication that each layer behaves as an independent graphene with little interaction with the rest of the graphene layers and the Cu substrate.

From **Figure 14 (b)**, it can be inferred that the p-bands from adjacent graphene layers cross each other at about $E_B = -0.5\ eV$ showing no evidence of minigap formation in contrast to previous observations in twisted bilayer graphene on Si-face SiC [**26,28**]. This, in turn, means that a saddle point and associated Van Hove singularity at the cone intersection are absent, further supporting our conclusion that the three graphene layers are essentially non-interacting. It should be noted that a minigap, if it existed, it would be expected to be 500 meV or larger based on what is reported [**26**] in 11.6°-twisted graphene and it should have been observed given that such a minigap is considerably higher than the estimated 110 meV resolution in our ARPES due to thermal broadening.

FLG on Cu(111) looks more like multilayer epitaxial graphene (with number of layers >3) on C-face SiC [**28**]. In this case, the layers are twisted in an ordered manner adopting commensurate twist angles; nevertheless, they do not interact, behaving as independent graphenes. We speculate that unlike the case of bilayer twisted graphene where commensurate twisting could give rise to Moire pattern and interlayer coupling [**26**], when more than two layers are involved (as in our case here), the Moire becomes more complex with larger period weakening the coupling as also previously suggested [**28**]. It is anticipated that twisting of graphene layers comes as a result of energy minimization since perfectly aligned AA stacking is energetically less favored. It cannot be excluded that the twisting is thermally activated, and in this case, the activation is expected to occur during the high temperature growth step, rather than the low temperature (420°C) post deposition annealing step in UHV prior to ARPES.

It should be noted that the ARPES intensity is about the same for all three layers (**Figure 14 (b)**). A possible explanation is that, due to significant inhomogeneity, graphene is in a single layer form over a significant portion of the sample (as indicated by Raman) and therefore the bottom layer is directly exposed to the energy analyzer yielding an intense ARPES signal. In other places of the sample covered by a second and third layer, the intensity of the bottom layer may be attenuated although not significantly. This could be due to the sufficiently large photoelectron inelastic mean free path *l* compared to the FLG thickness. Indeed, *l* is estimated to be $l \sim 9$ Å in graphite [**36**] for the excitation energy of 21.22 eV used in the present work. Given that the separation between graphene layers is

estimated ~3.4 Å (taken from graphite data), our total three layer graphene thickness of 6.8 Å is smaller compared to *l*. Summarizing, due to thickness inhomogeneity and the small number of layers, no significant intensity variations between the top and bottom graphene layers are observed.

It is worth noting that if a fourth or fifth graphene layer existed in significant quantities on the sample area, then at least two additional layers should be still detectable albeit with lower intensity in case they are residing at the bottom near the interface with Cu(111). In fact, it has been demonstrated [**28**] that it is possible to detect at least 4 graphene layers using 36 eV light excitation even though the corresponding $l \sim 6.2$ Å [**36**] is markedly smaller than that in the present work.

Based on the analysis above, it could be concluded that the maximum number of graphene layers is only three (as many as detected by ARPES), although the presence of more layers in much lower quantities (e.g., small flakes covering only small part of the surface) cannot be totally excluded. The uniform ARPES intensity does not allow for an unambiguous assignment of the three cones to the corresponding graphene layers. As already commented above, micro Raman indicates that the sample is rather inhomogeneous at the few micron scale with some areas covered by monolayer graphene and some other areas covered with FLG. Therefore, ARPES probing a large area on the sample detects the maximum number (three in our case) of twisted graphene layers present in significant quantities and gives no information about the spatial distribution.

An alternative interpretation of the three Dirac cones shown in **Figure 14** could be the presence of replica bands in the ARPES measurements. Previously, there have been reported works where, due to an electron-phonon coupling [**37**] or due to the existence of a Moiré periodic potential [**38**] such as in the case of graphene grown on a Ir(111) metal substrate, the formation of replica bands appears. These replicas are fainter than the actual bands and appear in specific positions of the k-space. Additionally, when replicas intersect with the primary bands, a minigap shows up. The presence of the minigap is considered an evidence of the existence of a Moiré periodic potential.

On the other hand, in our experimental ARPES measurements (**Figure 14**) it is clearly shown that the three Dirac cones have similar intensities and any minigap is open in their intersections. Similar intensities are expected since the ARPES measurements over a relatively large area of the sample are represented by an average and given that the existence of large areas with different number of layers was previously demonstrated by Raman spectroscopy. In addition the different Dirac cones move away from the Fermi level, possibly due to the increase of the charge transfer from the substrate, as the distance of the graphene layer with respect to the substrate decreases. Because of all the above, we think that the only possible explanation for these three Dirac cones is that each cone represents a different non-interacting graphene layer.

In summary, the electronic valence band structure of three layer CVD graphene on single crystal Cu(111) has been imaged by ARPES over a large area in k-space. It is found that graphene essentially grows polycrystalline with rotational domains oriented along the $[1\bar{1}0]_{Cu}$ and $[\bar{1}\bar{1}2]_{Cu}$ crystallographic directions. Along the $[1\bar{1}0]_{Cu}$ direction, or equivalently the $\overline{\Gamma K}$ direction of Cu in k-space, we obtain evidence of twisted three layer graphene with a twist angle of ~4°. Three nearly perfect Dirac cones indicate that there is no interlayer interaction in such a way that the three layers behave as independent graphenes. More generally, our results suggest that ARPES can directly measure the number of layers, the stacking order, and the degree of interlayer interaction complementing Raman for a full characterization of FLG.

3.3 Graphene grown on nickel

3.3.1 Introduction

Nickel catalyzes hydrocarbons more efficiently than copper, which allows a larger carbon atoms production in first instance. Another important difference with copper is the carbon solubility. This quantity is relative to how carbon can be absorbed by the metal. The carbon solubility on nickel is around 0.6 weight % at high temperatures while in copper is 0.008 weight % which makes a great difference between how many carbon atoms can be stored in these metals. In addition, carbon solubility depends on the temperature and more specifically it decreases with the temperatures.

Therefore, graphene grows on nickel in a different manner than on copper. At a high constant temperature graphene grows on nickel by precipitation and while the temperature decreases, it grows by segregation due to the change in the carbon solubility on nickel. The excess of carbon atoms is pulled out of the bulk towards the nickel surface. Because of these phenomena it is difficult to grow single layer graphene. On the other hand, these mechanisms can yield in AB-stacked graphene, which can also be interesting.

3.3.2 Graphene on nickel foils

Multi layer graphene predominantly grows on nickel due to the different mechanisms that have been shown above. One of these mechanisms, segregation, take place when the sample is cooled down and therefore, the cool down rate becomes important in this process. A fast cool down generally leads to disordered graphene, and a too slow rate can trap the carbon atoms inside [**5**]. On the other hand, a proper cool down rate can lead to a high ordered multilayer graphene [**39**].

To illustrate the importance of the cool down, graphene on nickel was grown with two different cool down rates and the substrates used were Ni foil 25 μm (Alfa Aesar 99%).

A first sample was annealed at T=900°C during 5 minutes at low pressure ($5 \times 10^{-2}\ Torr$) with a constant hydrogen flow rate of 100 sccm. Consequently, at the same temperature and pressure, the hydrogen was cut off and was introduced in the chamber an ethylene flow rate of 5 sccm, combined with a 40 sccm of argon, during 3 minutes. After the growth step, the ethylene flow was turn off and the sample was cooled down at a natural rate by switching off the halogen lamps. The cool down rate was estimated to be $14\ °C/s$ from 900°C to 600°C, with a faster rate of $20\ °C/s$ for the first 100°C.

For the micro-Raman measurements, an excitation Ar^+ laser beam, at 514.5 nm, with power of 1mW, was used, in order to minimize heating effects optical microscope of magnification up to 100x.

In **Figure 15** is shown a typical Raman spectrum of this sample. The ratio between the intensities of the 2D and the G peaks was $\frac{I_{2D}}{I_G} \sim 0.96$ and $FWHM_{2D} \sim 61.8\ cm^{-1}$. As it is shown in **Figure 15 (b)** the 2D peak was well-fitted with a single Lorentzian curve, which clearly indicates multi layer graphene with non-AB stacking.

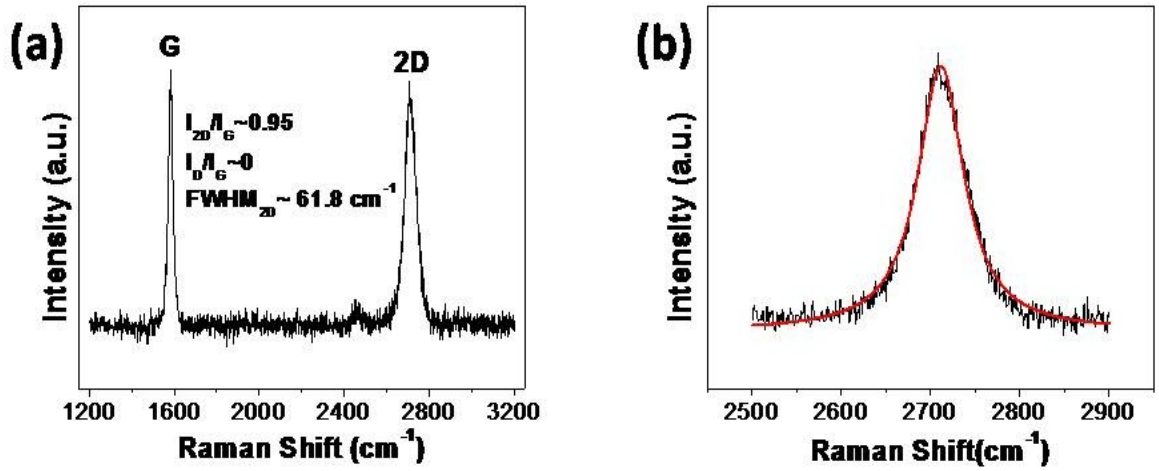

Figure 15. (**a**) Raman spectrum of graphene on nickel with a fast cool down. (**b**) 2D peak.

A second sample was annealed at T=900°C during 5 minutes at a low pressure ($5 \times 10^{-2}\ Torr$) and with a constant hydrogen flow rate of 100 sccm, as was did before. Consequently. the growth step was performed, using the same temperature and pressure

but without any hydrogen. Ethylene and argon were introduced in the chamber with a flow rate of 5 sccm and 40 sccm respectively, during 3 minutes. After the growth step, the ethylene flow was cut off and the sample was cooled down at a constant rate of $3\,°C/s$.

The Raman spectrum of this sample is shown in **Figure 16**. The ratio between the intensities of the 2D and the G peaks was $\frac{I_{2D}}{I_G}$~058 and $FWHM_{2D}$~70.3 cm^{-1}. In **Figure 16 (b)** it is shown the 2D peak, whose shape is different from the one of **Figure 15**. Since this time two Lorentzians were needed to properly fit the peak, whilst the most prominent peak was located at higher wavelength we can conclude that the graphene grown was multilayer, with an AB-stacking order.

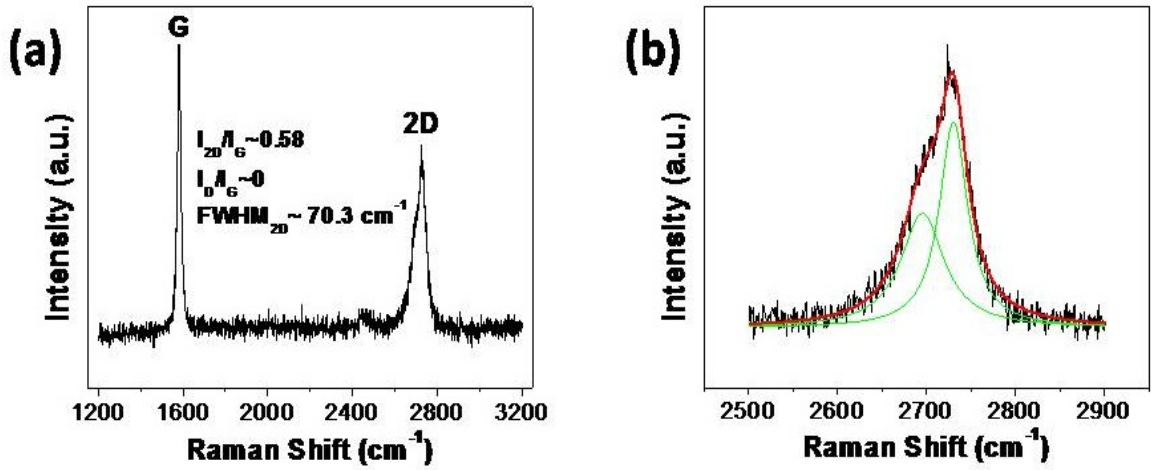

Figure 16. (**a**) Raman spectrum of graphene on nickel with a fast cool down, (**b**) 2D peak.

More generally, our results suggest that the cool down holds a main role in the growth of graphene on nickel. For the same reasons that renders it very difficult to achieve single layer graphene on nickel, it is also difficult to control the number of graphene layers.

Since few layers AB-stacked graphene could be interesting for possible electronic device uses, a further study is needed. Therefore, this study was extended in the direction of trying to achieve few layers graphene from a multilayer sample, by etching the graphene with hydrogen. On the next subchapter there are presented the published results of this work.

3.3.3 Graphene etching by hydrogen annealing on nickel foil

Nickel has a high carbon solubility which induces growth not only by segregation on the surface but also by precipitation. This is caused by the diffusion of the atomic carbon, created by the catalytic reaction and its subsequent reemergence on the surface, a process which strongly impedes the control on the number of graphene layers produced [**40,41**].

A lot of work has focused on controlling the growth process on Cu by carefully adjusting its parameters, such as the precursor concentration in the reactor, the hydrogen flow rate, the duration and the cool down rate [**3,42**]. Ni has been studied too but not so thoroughly. This subchapter aims to making a contribution to the problem of controlling the layer number of grown graphene on Ni by CVD etching, in much lower temperatures than previously demonstrated [**3,18,42]**.

Therefore, a post-growth etching process was examined, using hydrogen annealing under mild conditions, in order to reduce the number of graphene layers while avoiding the introduction of new defects in the crystals. After each graphene etching process, Raman characterization was performed to assess the quality and the number of layers of the graphene samples. In addition, scanning tunneling microscopy (STM) images were acquired to assess the surface quality and characteristics. Transmission electron microscopy (TEM) diffraction images were taken to probe the stacking of graphene, and x-ray photoelectron spectroscopy (XPS) measurements were taken to investigate the effect of our process on the graphene's quality.

Hydrogen, as a control parameter of the number of layers, is often used during the growth step [**43**] or during the cool down [**44**]. It has been proposed that hydrogen can play an etching role for graphene in the presence of a metal catalyst [**18**]. The method that we present here is a novel procedure in which the post-growth etching of graphene is performed in a separate process while the graphene is still on the metal substrate. Other studies have investigated the stability of graphene on SiO2 during an annealing step (in different conditions including an H_2/Ar atmosphere), a procedure which introduces defects in the crystals [**45,46**]. It is anticipated that applying a similar annealing procedure in the presence of a metal catalyst may be beneficial for the etching of graphene.

Considering the experimental details, firstly graphene was grown on Ni foil $2 \times 2\ cm^2$ (Alfa Aesar 25 μm thick 99%) by CVD within a cold-wall reactor chamber, as previously (**Figure 1**). The graphene growth process consisted of an initial annealing step of 5 min in a pressure of $5 \times 10^{-2}\ Torr$, at a temperature of T=900°C with a hydrogen flow rate

of 100 sccm. The annealing serves to clean the surface from the native oxide and any other possible contaminants and is followed immediately by the growth step.

Our objective was to produce samples with several graphene layers ordered in AB stacking, and therefore the growth was performed with a relatively high precursor flow (5 sccm ethylene diluted in 40 sccm Ar) for the given time of 5 min. Graphene layers grown by CVD on Ni have been reported [**39**] to self-organize in AB stacking at growth conditions similar to the ones we use here. In our study AB ordering of graphene is vital, because contrary to non-AB graphene, Raman characterization on AB-stacked graphene allows the distinction between multilayer-AB-stacked-graphene (MLG) and few-layer-AB-stacked-graphene (FLG) as demonstrated by Ferrari et al [**47**]. This ability to detect the transition from MLG to FLG allows us to verify and control the etching procedure.

After the graphene growth on Ni, the sample was characterized by Raman. Raman spectra were acquired using a Renishaw InVia Raman microscope using an Ar+ laser with 514 nm at room temperature and a laser power of 0.5 mW. As previously shown, a single layer graphene on Ni cannot be measured by Raman due to the strong interaction of graphene with the substrate [**48**]. However, in our case due to the large number of layers, we were able to take measurements since there is little or no influence from the metal substrate. Thus we can expect only slight variations from the spectra found in the literature where graphene on SiO_2 is typically reported [**47,49-53**]. Taking advantage of this fact, the transfer of graphene on other substrates such as SiO_2 or Al_2O_3, simply for measurement purposes, is avoided. However, the main reason for not transferring the graphene onto another substrate is to take advantage of the influence of the metal on the graphene etching process, as shown below.

TEM characterization followed the Raman measurements to probe the entirety of the samples' layering, utilizing an FEI CM20 TEM operating at 200 kV. Through selected area electron diffraction (SAED) and the produced diffraction patterns it is possible to make conclusions about the stacking order of the graphene layers. A perfect AB stacking will produce a single inner hexagon such as in graphite, which is essentially the extreme case of AB stacking concerning layer number [**54-56**]. On the other hand, a non-AB (twisted/turbostratic) ordering will produce diffraction rings consisting of multiple spots, indicative of the random orientation of many layers.

Finally, the sample's surface was also characterized by STM. The instrument used was an Omicron large-stage scanning probe microscope operating at room temperature. STM imaging on AB-stacked graphene produces a characteristic hexagonal pattern in which only one of the two atoms of graphene's unit cell are observed, resulting in the imaging of one of graphene's sublattices [**57**]. The same behavior is exhibited in graphite.

Contrary to this, single layer and non-AB graphene produce a typical honeycomb pattern [**58-62**]. Finally, etching cycles were performed by annealing the sample in a H_2/Ar atmosphere. As previously mentioned, it is known that hydrogen in the presence of a metal catalyst (Ni in our case) can etch away graphene [**18,43,63**]. Thus, we take advantage of the beneficial catalytic role the Ni substrate plays during the process to facilitate etching at a relatively low temperature. After each etching cycle, measurements of Raman spectroscopy and STM were taken again to assess the results.

Extensive Raman measurements were taken to characterize the samples before and after etching. A high degree of homogeneity was observed since the different spectra show only slight variations across the surface. A representative Raman spectrum is shown in **Figure 17 (a)**. The measurements were analyzed, and the G and 2D peaks were fitted with Lorentzian curves. The I_{2D}/I_G ratio, full width at half maximum of the 2D peak ($FWHM_{2D}$) and the center of the 2D peak (X_{2D}) were calculated. The measured values for these parameters are strongly indicative of MLG in the majority of cases. The statistics of the measurements are presented in **Table 4**.

	Mean	Std dev
I_{2D}/I_G	0.55	8.7%
$FWHM_{2D}$	56 cm^{-1}	10.2%
X_{2D}	2720 cm^{-1}	4.2 cm^{-1}

Table 4. Statistics of the I_{2D}/I_G ratio, $FWHM_{2D}$ and X_{2D} of Raman measurements for samples after growth. The quite low value of the I_{2D}/I_G ratio and the high values for $FWHM_{2D}$ and X_{2D}, along with their low standard deviations, strongly indicate an overall MLG surface.

Figure 17 (b) shows the fitting of the 2D peak with two Lorentzians from a characteristic spectrum. Such lineshape analysis has been thoroughly investigated by Ferrari et al [**47**] and others [**52**]. The best fitting here is achieved by the deconvolution of the 2D peak in two curves, a main and a secondary. In the case of MLG, as reported by Ying et al [**49**] and others [**50-52**], the main Lorentzian has its peak at a higher wavenumber, while in the case of FLG the main Lorentzian has its peak at a lower wavenumber. Our data and the specific fitting with two Lorentzians for the 2D peaks are in the majority of spectra in good agreement with what is reported [**50**] for MLG. Therefore, Raman characterization strongly indicates MLG.

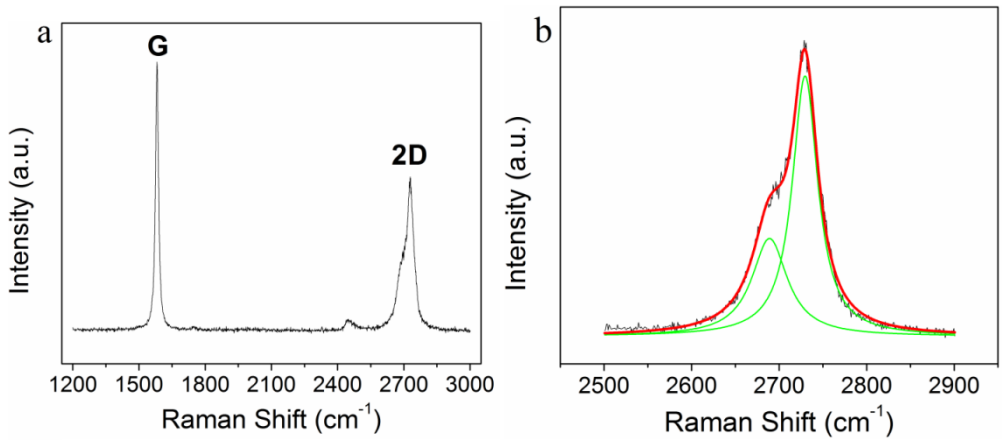

Figure 17. (**a**) Raman spectrum of an MLG, representative of the samples at the first stage before any etching treatment. The D peak is not present in any of our spectra. (**b**) A detail of the 2D peak is shown, which is best fitted by two Lorentzians with the main peak at the higher wavenumber.

Figure 18 shows a mapping of the I_{2D}/I_G ratio across an area of $125x125\ \mu m^2$ where only slight variations are observed, mainly at a few areas where Raman spectra are more consistent with FLG. An estimation from all the Raman measurements is that 100% of the total area in the sample is graphene with an AB stacking order. Of this, 88% is MLG and 12% is FLG.

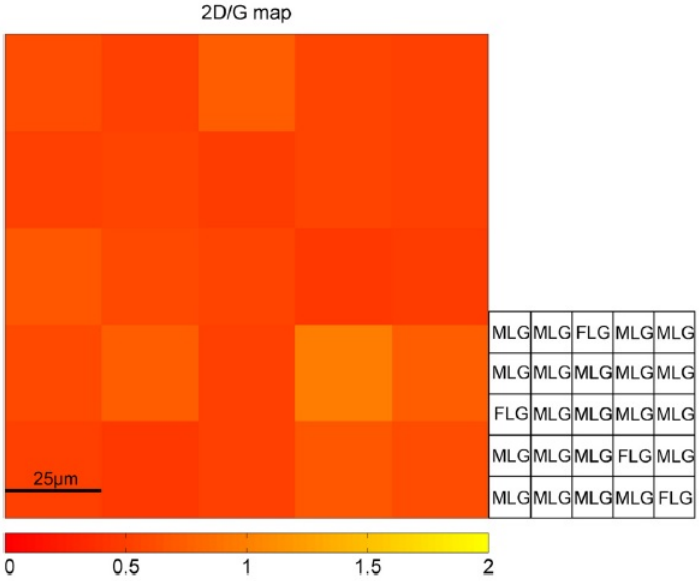

Figure 18. Mapping of I_{2D}/I_G intensity ratio in an as-grown sample. MLG and FLG denote multilayer graphene and few layer graphene, respectively.

Finally, it is worth noting that no D peak was detected in any of these measurements. This is very important for an assessment of the effect of our etching process on the quality of the graphene crystals. An etch step that deteriorates the graphene quality is not

desirable, limiting its use. As will be shown later, even after etching, no D peak was observed, indicating that our process does not affect the quality of the MLG.

Following the Raman characterization of the as-grown graphene, samples were transferred on TEM holey carbon grids and SAED patterns were obtained, as shown in **Figure 19**. These SAED patterns correspond to the [0001] zone axis of graphene. The samples show AB stacking in their majority, evident in the dominant {10–10} diffraction spots exhibiting the characteristic hexagonal symmetry of [0001] crystal axis. Such symmetry appears in the case of single layer graphene, AB-stacked graphene and graphite, which is also formed in an AB stacking configuration. **Figure 19** shows typical SAED patterns taken from various sites of the samples. In **Figure 19 (a)** all layers are arranged in AB stacking from top to bottom, while **Figures 19 (b)** and **(c)** offer some additional information.

Apart from the dominant spots related to AB, two more configurations appear. **Figure 19 (b)** suggests the existence of some layers being arranged in non-AB (turbostratic/twisted) order as evidenced by the less bright diffraction rings in addition to the dominant spots. Secondly, in **Figure 19 (c)** while there are no non-AB diffraction rings, the dominant spots have ‘satellite’ or secondary spots near them, indicative of small deviations from the perfect AB stacking within the layers. As it is shown below, these two types of deviation from the perfect AB arrangement are also verified by Raman and STM after the performed hydrogen etchings. It is evident from the above discussion that the vast majority of the samples’ graphene layers shows strong evidence of being arranged in AB stacking order.

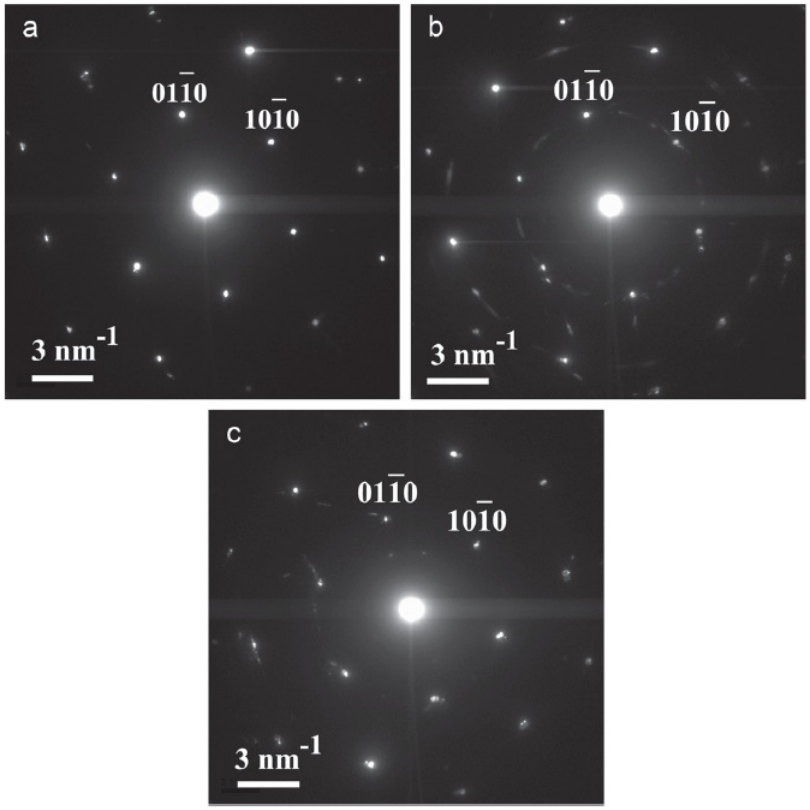

Figure 19. TEM–SAED diffraction images taken from an as-grown sample. The clearly visible hexagonal diffraction pattern indicates that the layers are predominantly arranged in AB stacking order. (**a**) AB stacking order across the sample thickness. (**b**) A complex diffraction pattern consisting of dominant hexagonal arrangement and superimposed faint circles which are attributed to non-AB layers arranged at random orientations relative to each other. (**c**) Spots very close to the dominant hexagon, forming a slightly rotated hexagon attributed to layers with a very small deviation from the perfect AB stacking.

Finally, to further corroborate the existence of AB stacking order, at least for the top layers, STM measurements were also taken from the sample. While STM scans a small area, images from many regions were taken to obtain a broader picture of the surface. In all cases the characteristic
hexagonal pattern that is attributed to AB stacking was observed. **Figure 20 (a)** shows a typical high-resolution STM image of the as-grown graphene on Ni. The hexagonal pattern is clearly observed. This happens when only one of the two atomic sub-lattices of graphene is imaged, characteristic of AB stacking. **Figure 20 (b)** shows a profile along the line drawn on **Figure 20 (a)**, where a periodicity of 2.48 Å is measured, which is in agreement with the graphene lattice constant of 2.46 Å.

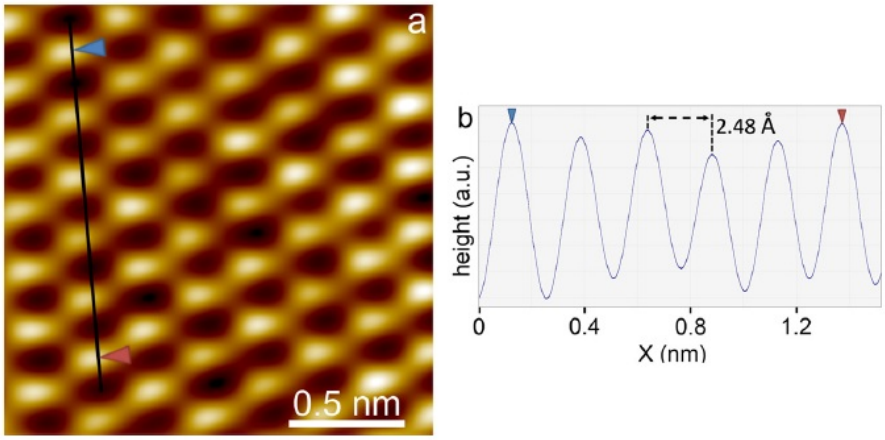

Figure 20. (**a**) A typical STM image of graphene on Ni showing AB stacking. $size = 1.9nm \times 1.9nm$. (**b**) Profile along line drawn on (**a**), showing the lattice periodicity measured at 2.48 Å.

Following the characterization of the as-grown graphene, the samples were placed again inside the reactor. Initially, the control of the graphene etching rate was studied, adjusting two basic parameters—the annealing temperature and the hydrogen-to-argon ratio. Three main temperatures of 400 °C, 450 °C and 500 °C, and three H2/Ar ratios of 5%, 15% and 25%, were tested. For all H2/Ar ratios the total flow rate was kept constant at 200 sccm. The process duration remained fixed at 10 min.

As in other studies [**3,18,42**], we expect that the presence of a metal substrate facilitates the etching of graphene. Taking into account that Ni is a stronger catalyst than copper, we use a lower temperature to perform the etching. Without exhausting all possible mechanisms we expect that graphene edges and defects play a vital role since in these sites C atoms are more chemically active than C atoms in the basal plane. It has been demonstrated [**64**] that graphite edges can dissociate hydrogen and form highly reactive atomic hydrogen. This atomic hydrogen can in turn attack not only the edge and defects, but also atoms in the basal plane. This can lead to a weakening of the C–C bonds, and therefore etching can occur both at the edges and the basal plane, as described in other studies [**65-66**].

Figure 21 presents a schematic of the etching process in which the H_2 gas in the presence of Ar reacts with the C atoms of the graphene layer to form CH_x.

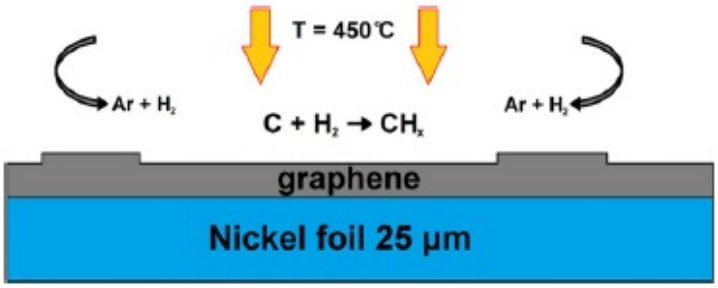

Figure 21. The sample is annealed for 10 min in a H_2/Ar atmosphere with a total flow rate of 200 sccm in order to etch graphene layers.

After each etching combination the samples were again characterized by Raman spectroscopy. All the 2D peaks from multiple measurements were fitted with Lorentzian curves to identify spectra indicative of FLG. The criterion for a successful etching was the frequency of occurrence of such spectra in the etched samples. Specifically, having started with MLG samples, a higher number of FLG spectra implied a more successful etching. As already mentioned, the 2D peak in FLG is best fitted with two Lorentzians, with the main one having its peak at a lower wavenumber. **Figure 22** shows a typical spectrum from etched samples. The results for each combination of the etching parameters are presented in **Table 5**.

Temperature	H_2/Ar: 5%	H_2/Ar: 15%	H_2/Ar: 25%
400 °C	No etching	No etching	No etching
450 °C	Little or no etching	Etching (selected)	Etching
500 °C	Little etching	Etching	Etching

Table 5. Results for different temperatures and H_2/Ar ratios combinations used in the etching process. T_1=400°C yielded no notable etching while T_3=500°C showed no improvement over T_2=450°C. Similarly an H_2/Ar ratio of 5% proved insufficient while a ratio of 25% did not improve the process over the ratio of 15%. Hence the combination of T_2=450°C with a 15% H_2/Ar ratio was selected as optimal.

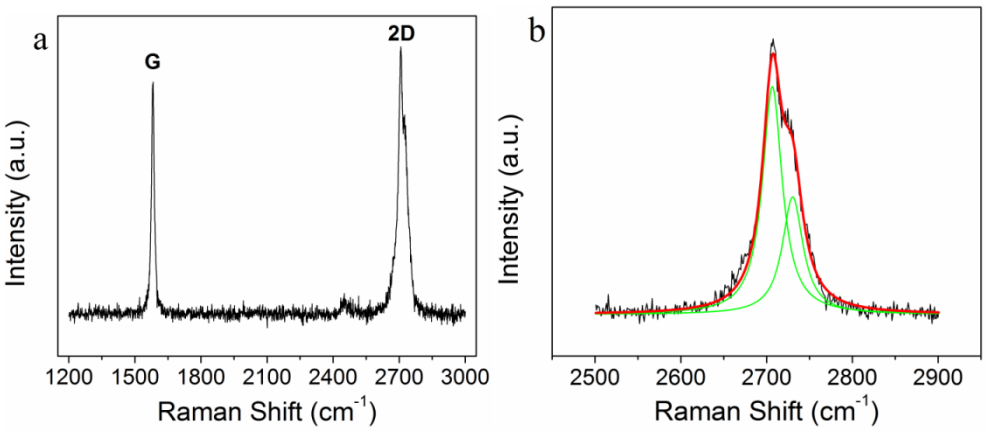

Figure 22. (**a**) Raman spectrum of an FLG, representative of samples after first annealing with H2. The D peak is not present. (**b**) A 2D detail is shown, which can be fitted again by two Lorentzians, but now the main peak is located at the lower wavenumber. This is indicative of FLG.

It is concluded from **Table 5** that the optimum temperature is T_2=450°C. In comparison, T_1=400°C is rather inefficient for etching and T_3=500°C offered no significant advantages, so the lower temperature which offers a lower thermal budget is preferable. The H2/Ar ratio of 15% was selected due to its optimum graphene etch rate. A ratio of 5% proved to be insufficient, whereas a 25% ratio does not greatly improve the etch rate. For the selected optimum conditions the statistics for the I_{2D}/I_G ratio, the $FWHM_{2D}$ and the X_{2D} are presented in **Table 6**.

	Mean	Std dev
I_{2D}/I_G	1.008	±34.7%
$FWHM_{2D}$	41.1 cm^{-1}	±17.4%
X_{2D}	2710 cm^{-1}	3.93 cm^{-1}

Table 6. Statistics of the I_{2D}/I_G ratio, $FWHM_{2D}$ and X_{2D} of Raman measurements for samples after etching at T_2=450°C with an H_2/Ar ratio of 15%. The value of the I_{2D}/I_G ratio is higher than before etching, the values for $FWHM_{2D}$ and X_{2D} are lower. These values indicate FLG at the majority of the surface.

These results are different to the ones obtained on as grown graphene (**Figure 17, Table 4**). All 2D peaks can still be fitted with two Lorentzians, but now in the majority of the spectra the two curves are reversed with respect to intensity, as seen in **Figure 17**. The band with the highest intensity has its peak located at a lower wavenumber, which indicates FLG structures as reported by Ying et al [**49**] and others [**47,50-52**]. So, in comparison with the previous characterizations, an overall reduction from MLG to FLG on the samples can be inferred from the spectra. While the previous measurements

performed in as-grown samples indicate MLG, now the samples after the etching have FLG in the majority of the samples' surface. This is evidence that top graphene layers were etched during the process. Based on the Raman measurements, we can estimate that of the total graphene area 5% is non-AB stacking grapheme, while 95% is AB stacking graphene, of which 81.5% is FLG and 18.5% is still MLG. A mapping of the I_{2D}/I_G intensity ratio is shown in **Figure 23**. The majority of the measurements have an I_{2D}/I_G that corresponds to FLG.

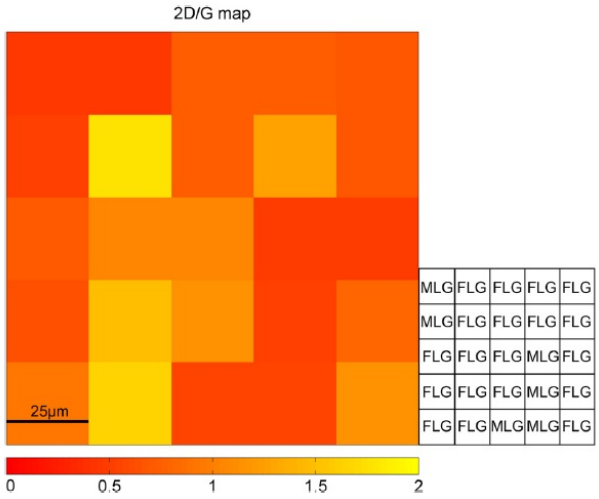

Figure 23. Mapping of the I_{2D}/I_G intensity ratio in an etched sample under optimum conditions for 10 min MLG and FLG denote multilayer graphene and few layer graphene, respectively.

Notably, the absence of the D peak in all Raman measurements indicates that there are no defects produced during the etching process, maintaining the high crystalline quality of the as-grown MLG graphene. To further confirm the fact that our method does not deteriorate the graphene quality, XPS measurements were taken before and after the etching process. The results shown in **Figure 24** confirm that no change occurs concerning the chemical composition of the crystals. No hydrogenation, oxidation or other alteration is evident after the etching. In situ XPS was performed using Mg-Kα radiation (1253.6 eV) at a take-off angle of 52°. Gaussian-Lorentzian shapes (Voigt functions) were used for deconvolution of the recorded spectra after standard Shirley background subtraction.

A three-peak fitting procedure was applied to the XPS C1s peaks for both the as-grown and etched samples. The dominant component at 284.5 eV indicates the high quality of the CVD-grown graphene layer. Only a minor, almost negligible, component is observed at 286 eV, which has been attributed to the presence of C–O bonds. In addition, the very close resemblance of the C1s peak before and after treatment implies that the process does not affect the graphene's quality and points to the exclusion of new C–H, C–O or

other bonds in the treated sample, meaning that no hydrogenation, oxidation or other chemical alteration has occurred.

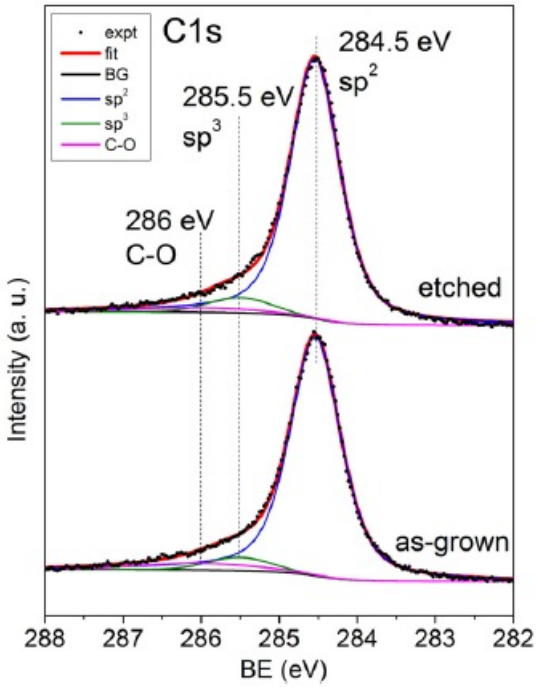

Figure 24. XPS measurements of the C1s region before and after etching. A dominant peak at 284.5 eV is indicative of the graphene's high quality. No changes are evident after etching, implying that graphene's quality remains unaffected.

As a final step, using the selected temperature and hydrogen/argon ratio (T=450°C, H_2/Ar: 15% at 200 sccm) we examine the graphene etching by varying a third parameter, the process time. A second series of samples, with a slightly longer etch duration of t=12 min, was processed and was subsequently characterized by Raman and STM. After the 12 min etching, the layers with AB stacking order are removed from the largest part of the sample. While some regions continue to have spectra indicative of FLG, the majority of the measurements have 2D peaks that are best fitted with a single Lorentzian, indicative of graphene with non-AB stacking order [**67**]. A typical spectrum is shown in **Figure 25**. Also, as expected from non-AB graphene, the I_{2D}/I_G ratio shows large variation across the measurements. This is characteristic of non-AB graphene, because, as reported by Kwanpyo et al [**52**], the I_{2D}/I_G ratio is strongly affected by the relative rotation angle between the layers. The rotation angle in non-AB graphene can vary a lot from site to site for polycrystalline graphene typically produced by CVD. The statistics for the samples etched for 12 min are shown in **Table 7**.

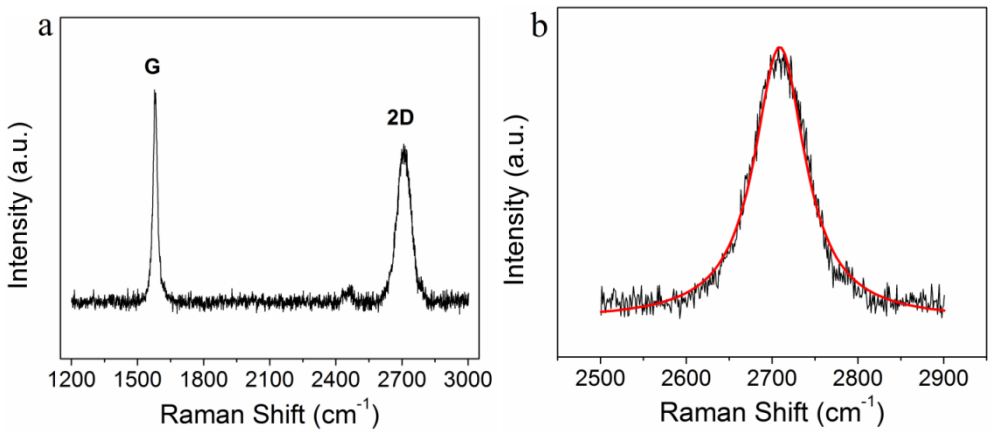

Figure 25. (**a**) A representative Raman spectrum of the sample with a further annealing process with H_2 is shown. Due to the absence of a D peak, it can be concluded that any defect has been induced after this further annealing. (**b**) The 2D peak detail shows that the peak can be fitted with only one Lorentzian, which is an indication of non-AB graphene.

	Mean	Std dev
I_{2D}/I_G	1.358333	±59.9%
$FWHM_{2D}$	43.2 cm^{-1}	±22.2%
X_{2D}	2711 cm^{-1}	4.94 cm^{-1}

Table 7. Statistics of the I_{2D}/I_G ratio, $FWHM_{2D}$ and X_{2D} of Raman measurements for samples after etching for 12 minutes. The value of the I_{2D}/I_G ratio is higher, the values for $FWHM_{2D}$ and X_{2D} have not changed significantly while all the standard deviations have increased significantly. Such a great variation in these values is indicative of non-AB stacked graphene.

A mapping of the I_{2D}/I_G intensity ratio is shown in **Figure 26**, from which it can be inferred that at this stage the sample is less uniform compared to the previous stage. In this case we can estimate that 81.25% of the total area is non-AB stacking graphene, while 18.75% is AB stacking graphene. The AB stacking graphene is divided into 85% FLG and 15% MLG.

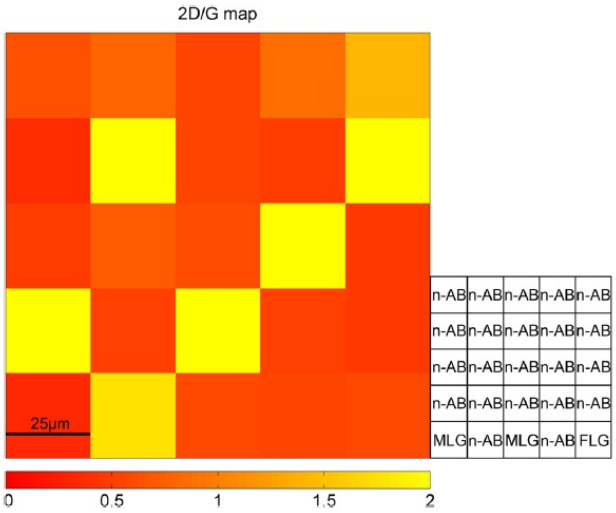

Figure 26. Mapping of I_{2D}/I_G intensity ratio in an etched sample under optimum conditions for 12 min.

This data indicate that the as-grown samples consist of AB-stacked graphene on top of non-AB-stacked layers. The co-existence of both stacking orders, with the AB being dominant, is in agreement with the SAED patterns shown previously in **Figure 19**. After etching, layers that have a non-AB stacking order are revealed. Again, the complete absence of the D peak shows that no defects have been produced, even after a longer etching process.

Further, STM images were acquired from the surface of the sample after the 12 min etching step. Whereas before the etching the sample surface showed AB stacking ordering in the form of the hexagonal pattern, the images obtained now, shown in **Figures 27 and 28**, are of two kinds in accordance with Raman evidence. A typical image from the 12 min etched samples showing AB stacking is shown in **Figure 27 (a)**. **Figure 27 (b)** shows a profile along the line in image (**a**) in which a lattice periodicity of 2.46 Å is measured in good agreement with graphene's lattice constant.

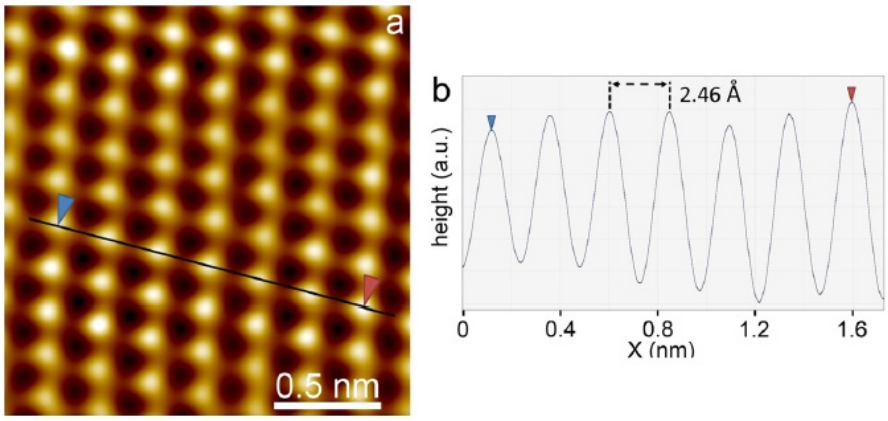

Figure 27. (**a**) A typical STM image of sample areas still showing AB stacking after 12 min of etching. $Size = 1.9\,nm \times 1.9\,nm$. (**b**) Profile along the line drawn on (a), showing the lattice periodicity which is measured at 2.46 Å.

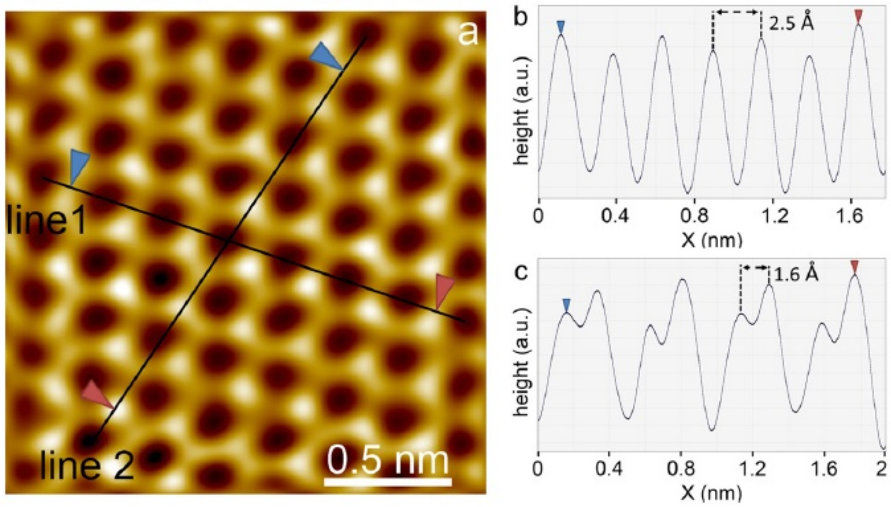

Figure 28. (**a**) A typical STM image of sample areas showing non-AB stacking (honeycomb lattice) after 12 min of etching. $Size = 1.9\,nm \times 1.9\,nm$. (**b**) Profile along line 1 drawn on (**a**) showing the lattice periodicity which is measured at 2.5 Å. (**c**) Profile along line 2 drawn on (**a**), showing the C–C bonds measured at 1.6 Å, close to the theoretical value of 1.42 Å.

However, many regions now show a honeycomb structure (**Figure 28 (a)**). This agrees with STM images of non-AB stacked graphene [**58-62**]. **Figure 28 (b)** shows a profile along line 1 drawn on image (**a**) in which a bond length of 1.6 Å is measured, which is close to the C–C sp2 bond length of 1.42 Å. In **Figure 28 (c)** we show a profile along line 2 of image (**a**), where a periodicity of 2.5 Å is again confirmed. It is worth noting that in the honeycomb structure a trigonal symmetry is also observed. At the three corners of each hexagon composed from carbon atoms the three spots are brighter and the other three are dimmer. This indicates that even though the top graphene layer is at a non-AB

stacking with the layer below it, there is still some interaction. This interaction, we believe, is responsible for the interference pattern that creates this particular symmetry in some of the STM images. It is an indication that the rotation of the top layer relative to the one below it is close to 60°, which is the case for AB stacking. The existence of this structure closely resembling the AB stacking in some cases was also indicated by the TEM–SAED image in **Figure 19 (c)**. We conclude that what is imaged is an overlap of patterns, with the honeycomb pattern being dominant.

An emergent point of interest in this study is the apparent layering of the graphene. The successful etching of a large number of AB-stacked layers revealed non-AB layers that are closer to the metal substrate. While many studies have reported the production of MLG on Ni with
various growth conditions, little work has been done to confirm that all the layers are indeed AB-stacked. Our results are in agreement with the growth mechanism proposed by Baraton et al [**41**]. The majority of the graphene layers are grown during the catalytic dissociation of the precursor, while some layers are grown by out-diffusing precipitation—probably during the cooling phase of the process. In the latter case, the layers produced are not AB stacked but are randomly oriented relative to each other. An explanation for this is that during the cooling stage there is insufficient energy for the carbon atoms to be arranged in the most energetically favorable configuration [**68**], i.e. the AB stacking. Because the cooling stage is a rapid process in which the metal substrate loses thermal energy, the atoms, and therefore the graphene layers, are 'frozen' in the positions and orientations in which they are out-diffused from the Ni surface. This has implications on the possible uses of graphene produced on Ni by CVD, as AB graphene has potentially very different properties from non-AB-stacked graphene.

We have shown that graphene can be etched by annealing in a H_2/Ar atmosphere at a low temperature (T=450°C) without introducing defects on the sample as proven by Raman spectra. We propose this method for post-growth control on the number of layers while graphene is still on the metal catalyst. This presents a methodology to obtain few layer and potentially single layer graphene on Ni by etching a thicker MLG, which is typically obtained by CVD on Ni. Our method, which is a relatively low-temperature procedure, could be combined with growth processes at low temperatures as well and be compatible with further use of the graphene in a possible multi-step process with a low thermal budget. Finally, we also present evidence that the top layers are arranged in an AB stacking order while the bottom layers close to the interface with Ni are grown in a random orientation with respect to each other, probably due to the out-diffusion of less energetic carbon atoms during the cooling down step.

References

[1] E. S. Polsen, D. Q. McNerny, B. Viswanath, S. W. Pattinson and A. J. Hart, Scientific Reports 5, Article number: 10257 (2015)
[2] W. Liu, H. Li, C. Xu, Y. Khatami, K. Banerjee, Carbon 49, 4122-4130 (2011)
[3] M. Losurdo, M. M. Giangregorio, P. Capezzuto and G. Bruno, Phys. Chem. Chem. Phys., 13, 20836–20843 (2011)
[4] J. K. Wassei, M. Mecklenburg, J. A. Torres, J. D. Fowler, B. C. Regan, R. B. Kaner and B. H. Weiller, Small 8, 9, 1415–1422 (2012)
[5] S. Bhaviripudi, X. Jia, M. S. Dresselhaus and J. Kong, Nano Lett., 10, 4128–4133 (2010)
[6] J. Coraux, A.T. N'Diaye, M. Engler, C. Busse, D. Wall, N. Buckanie, F.-J. Meyer zu Heringdorf, R. van Gastel, B. Poelsema and T. Michely, New J. Phys. 11 023006 (2009)
[7] M. Liu, Y. Gao, Y. Zhang, Y. Zhang, D. Ma, Q. Ji, T. Gao, Y. Chen, Z. Liu, Small 9, 8 1360-1366 (2013)
[8] E. Sutter, P. Albrecht and P. Sutter, Appl. Phys. Lett. 95, 133109 (2009)
[9] B. Hu, H. Ago, Y. Ito, K. Kawahara, M. Tsuji, E. Magome, K. Sumitani, N. Mizuta, K. Ikeda, S. Mizuno, Carbon 50, 1, 57-65 (2012)
[10] V. Patil, A. Capone, S. Strauf and E.-H. Yang, Scientific Reports 3, 2791 (2013)
[11] J. Yin, H. Wang, H. Peng, Z. Tan, L. Liao, L. Lin, X. Sun, A. L. Koh, Y. Chen, H. Peng and Z. Liu, Nature Communications 7, 10699 (2016)
[12] Q. Yu, J. Lian, S. Siriponglert, H. Li, Y. P. Chen and S.-S. Pei, Applied Physics Letters 93, 113103 (2008)
[13] Z. Sun, Z. Yan, J. Yao, E. Beitler, Y. Zhu and J. M. Tour, Nature 468, 549–552 (2010)
[14] J. Kwak, J. H. Chu, J.-K. Choi, S.-D. Park, H. Go, S. Y. Kim, K. Park, S.-D. Kim, Y.-W. Kim, E. Yoon, S. Kodambaka and S.-Y. Kwon, Nature Communications 3, 645 (2011)
[15] A. Guermoune, T. Chari, F. Popescu, S. S. Sabri, J. Guillemette, H. S. Skulason, T. Szkopek and M. Si, Carbon 49, 13, 4204-4210 (2011)
[16] X. Li, C. W. Magnuson, A. Venugopal, R. M. Tromp, J. B. Hannon, E. M. Vogel, L. Colombo and R. S. Ruoff, J. Am. Chem. Soc., 133 (9), 2816–2819 (2011)
[17] Y. Li, D. Datta, Z. Li, V. B. Shenoy, Computational Materials Science, 83, 212-216 (2014)
[18] I. Vlassiouk, M. Regmi, P. Fulvio, S. Dai, P. Datskos, G. Eres and S. Smirnov, ACS Nano, 5 (7), 6069–6076 (2011)
[19] X. Li, C. W. Magnuson, A. Venugopal, J. An, J. W. Suk, B. Han, M. Borysiak, W. Cai, A. Velamakanni, Y. Zhu, L. Fu, E. M. Vogel, E Voelkl, L. Colombo and R. S. Ruoff, Nano Lett., 10 (11), 4328–4334 (2010)

[20] G. H. Han, F. Günes, J. J. Bae, E. S. Kim, S. J. Chae, H.-J. Shin, J.-Y. Choi, D. Pribat and Y. H. Lee, Nano Lett., 11 (10), 4144–4148 (2011)
[21] X.-D. Chen, Z.-B. Liu, C.-Y. Zheng, F. Xing, X.-Q. Yan, Y. Chen, J.-G. Tian, Carbon 56, 271-278 (2013)
[22] J. A. Leon, N. C. Mamani, A. Rahim, L. E. Gomez, M. A. P. da Silva, G. M. Gusev, Graphene 3, 25-35 (2014)
[23] J. W. Suk, A. Kitt, C. W. Magnuson, Y. Hao, S. Ahmed, J. An, A. K. Swan, B. B. Goldberg and R. S. Ruoff, ACS Nano, 5 (9), 6916–6924 (2011)
[24] S. Vaziri, A.D. Smith, G. Lupina, M. C. Lemme, Solid State Device Research C, 309-312 (2014)
[25] J. Song, F.-Y. Kam, R.-Q. Png, W.-L. Seah, J.-M. Zhuo, G.-K. Lim, P. K. H. Ho and L.-L. Chua, Nature Nanotechnology 8, 356–362 (2013)
[26] T. Ohta, J. T. Robinson, P. J. Feibelman, A. Bostwick, E. Rotenberg, and T. E. Beechem, Phys. Rev. Lett. 109, 186807 (2012).
[27] T. Ohta, T. E. Beechem, J. T. Robinson, and G. L. Kellogg, Phys. Rev. B 85, 075415 (2012).
[28] M. Sprinkle, J. Hicks, A. Tejeda, A. Taleb-Ibrahimi, P. Le Fevre, F. Bertran, H. Tinkey, M. C. Clark, P. Soukiassian, D. Martinotti, J. Hass and E. H. Conrad, J. Phys. D: Appl. Phys. 43, 374006 (2010).
[29] M. Batzill, Surf. Sci. Rep. 67, 83–115 (2012)
[30] K. Kim, S. Coh, L. Z. Tan, W. Regan, J. M. Yuk, E. Chatterjee, M. F. Crommie, M. L. Cohen, S. G. Louie, and A. Zettl, Phys. Rev. Lett. 108, 246103 (2012).
[31] G. T. De Laissardiere, D. Mayou, and L. Magaud, Nano Lett. 10, 804 (2010).
[32] E. J. Mele, Phys. Rev. B 84, 235439 (2011).
[33] A. L. Walter, S. Nie, A. Bostwick, K. S. Kim, L. Moreschini, Y. J. Chang, D. Innocenti, K. Horn, K. F. McCarty, and E. Rotenberg, Phys. Rev. B 84, 195443 (2011).
[34] A. Varykhalov, M. R. Scholz, T. K. Kim, and O. Rader, Phys. Rev. B 82, 121101 (2010).
[35] J. Hicks, M. Sprinkle, K. Shepperd, F. Wang, A. Tejeda, A. Taleb- Ibrahimi, F. Bertran, P. Le Fevre, W. A. de Heer, C. Berger, and E. H. Conrad, Phys. Rev. B 83, 205403 (2011).
[36] C. J. Powell and A. Jablonski, NIST Electron Inelastic-Mean-Free-Path Database-Version 1.2, National Institute of Standards and Technology, Gaithersburg, MD, 2010
[37] J. J. Lee, F. T. Schmitt, R. G. Moore, S. Johnston, Y.-T. Cui, W. Li, M. Yi, Z. K. Liu, M. Hashimoto, Y. Zhang, D. H. Lu, T. P. Devereaux, D.-H. Lee and Z.-X. Shen, Nature 515, 245–248 (2014)

[38] I. Pletikosić, M. Kralj, P. Pervan, R. Brako, J. Coraux, A. T. N'Diaye, C. Busse, and T. Michely, Phys. Rev. Lett. 102, 056808 (2009)
[39] S. J.Chae et al.Adv. Mater. 21 2328–33 (2009)
[40] A. Reina et al. Nano Res. 2 509–16 (2009)
[41] L. Baraton et al. Europhys. Lett. 96 46003 (2011)
[42] Y. Zhang, Z Li, P Kim, L Zhang and C Zhou, ACS Nano 6 126–32
[43] W. Wu, Q Yu, P Peng, Z Liu, J Bao and S-S Pei, Nanotechnology 23, 035603 (2012)
[44] H J Park, J Meyer, S Roth and V Skakalova, Carbon 48 1088–94 (2010)
[45] Z HNi et al, J. Raman Spectrosc. 41 479–83 (2010)
[46] H-Y Nan, Z-H Ni, J Wang, Z Zafar, Z XiangShia and Y-Y Wang, J. Raman Spectrosc. 44 1018–21 (2013)
[47] A C Ferrari et al Phys. Rev. Lett. 97 187401
[48] A Dahal and M Batzill, Nanoscale 6, 2548–62 (2014)
[49] Y. Y. Wang et al J. Phys. Chem. C, 112, 10637–40 (2008)
[50] D Yoon, H Moon, H Cheong, J-S Choi, J A Choi and B H Park, J. Korean Phys. Soc. 55, 1299–303 (2009)
[51] I Calizo, A A Balandin, W Bao, F Miao and C N Lau, Nano Lett. 7, 2645–9 (2007)
[52] Y Hao et al Small 6, 195–200 (2010)
[53] K Kim et al Phys. Rev. Lett. 108 246103 (2012)
[54] F J Derbyshire, E B Preslandand and D L Trimm, Carbon 13, 111–3 (1975)
[55] H-K Jeong, Y. P. Lee, R J W E Lahaye, M-H Park, K H An, I J Kim, C W Yang, C Y Park, R S Ruoff and Y H Lee, J. Am. Chem. Soc. 130 1362–66 (2008)
[56] F J Derbyshire, E B Preslandand and D L Trimm, Carbon 10, 114–5 (1972)
[57] S Hembacher, F J Giessibl and J Mannhart, Phys. Rev. Lett. 94, 056101 (2005)
[58] W Yongfeng, Y Yingchun and W Kai, Surf. Sci. 600, 729–34 (2006)
[59] H S Wong, C Durkan and N Chandrasekhar, ACS Nano 3, 3455–62 (2009)
[60] B Lalmi et al Sci. Rep. 4, 4066 (2013)
[61] M Endo, K Oshida, K Kobori, K Takeuchi and K Takahashi, J. Mater. Res. 10, 1461–8 (1995)
[62] E Y Andrei, G Li and X Du, Rep. Prog. Phys. 75, 056501 (2012)
[63] A C Ferrari and D M Basko, Nat. Nanotechnology 8, 235–46 (2013)
[64] Z J Pan and R T Yang, J. Catalysis 123, 206–14 (1990)
[65] J I Martínez, J A Martín-Gago, J Cernicharo and P L de Andres, J. Phys. Chem. C 118, 26882–6 (2014)
[66] P Merino, M Svec, J I Martinez, P Jelinek, P Lacovig, M Dalmiglio, S Lizzit, P Soukiassian, J Chernicharo and J A Martin-Gago, Nat. Commun. 5, 3054 (2014)
[67] D R Lenski and M S Fuhrer, J. Appl. Phys. 110, 013720 (2011)
[68] A Masato and H Amawashi, Solid State Commun. 142, 123–7 (2007)

Chapter 4

Metal Insulator Semiconductor (MIS) Devices with Encapsulated Graphene in the Gate

4.1 Introduction

Despite the outstanding electronic properties of graphene [**1**], it has also a major drawback that prevents graphene of being used as a part of the channel in clasical field effect transistors (FET). The lack of an energy gap [**2**] does not allow to control the current along the channel with a gate voltage. Although many efforts have been done to open a gap, such as tailoring graphene nanoribbons [**3**] or functionalization [**4**,**5**], such actions significantly altered the graphene properties making it less interesting for electronic devices.

However, graphene could be implemented in electronic devices using a different architecture or in other parts of the clasical FET apart from the channel. Regarding a new device architecture, the control of tunneling current between two graphene layers through a thin dielectric has been succesfully reported by other teams [**6**,**7**]. In such devices it is possible to tune externally the fermi level and the aligment of both Dirac points which allows the control of a vertical current between the graphene layers. On the other hand, graphene can be used as a part of the gate by modifying the gate oxide. In this case, an enhacement of the capacitance has been reported using a stacking of graphene and other dielectircs [**8**,**9**] and it has been related with a negative quantum capacitace that graphene introduces in the gate.

In this chapter we managed to embed graphene in the oxide of a metal-insulator-semiconductor (MIS) device. The aim of this work was to study the behavior of a MIS device modified with graphene and to understand if its precence in this structure could improve the performance of the device, which is crucial for its future implementation as the gate of the FET.

4.2 Negative quantum capacitance

Quantum capacitance was first defined by S. Luryi in 1987 [**10]**. In a capacitor in which one of the metal plate has been sustitued by a 2DEG the capacitance measured is less than the geometric capacitance

$$C_{geom} = \frac{\varepsilon A}{4\pi d} \quad (4.1)$$

where ε is the dielectric constant of the material between the plates, A the area of the plates and d is the distance between them. The system behaves as if were a second capacitance in series with the geometric capacitance. This capacitance is called quantum capacitance and is related to the two-dimensional properties of the second plate. This quantum capacitance is given by

$$C_Q = \frac{g_v m e^2}{\pi \hbar^2} \quad (4.2)$$

where m is the effective electron mass in the direction perpendicular to the 2DEG, and g_v is the valley degeneracy factor [**11]**. For MIS structures on a Si (100) surface $g_v = 2$ and $m = 0.98m_0$, where m_0 is the mass of the electron, the quantum capacitance is larger than the geometric capacitance, so as they are serially added the contribution of the quantum capacitance to the total capacitance is negligible. For smaller values of m, this quantity becomes more important.

$$\frac{1}{C_{tot}} = \frac{1}{C_{geom}} + \frac{1}{C_Q} \quad (4.3)$$

More generally, the quantum capacitance can be defined as the second derivative of the ground state energy $E_g \approx E_{kin} + E_{exch}$ with respect to the carrier density per area *n* [**12]**:

$$C_Q^{-1} = \left(\frac{1}{e^2}\right)\frac{\partial^2 E_g}{\partial n^2} = C_{kin}^{-1} + C_{exch}^{-1} = \left[e^2 \rho_{E_F}^{(2D)}\right]^{-1} - \frac{\left[(2\pi)^{3/2}\varepsilon_0 \varepsilon_{eff}\right]^{-1}}{\sqrt{n}} \quad (4.4)$$

where $\rho_{E_F}^{(2D)}$ is the density of states near the Fermi energy, and n the carrier density per area. The first kinetic term in **Equation 4.4** is always positive, and in good approximation, independent of *n* as a consequence of constant 2D energy DOS $\rho_{EF}^{(2D)} = m^*/\pi\hbar^2$ (m* is the carrier effective mass). On the other hand, the second exchange interaction term in **Equation 4.4** gives a negative, *n*-dependent contribution which could become dominant over the kinetic term at low *n* values. The parameters ε_0 and ε_{eff} are the vacuum and effective dielectric constants of the 2D electron system.

It has been proposed that negative capacitance in the gate of FETs can produce an internal gate amplification and subthermoionic transport with subthreshold slopes smaller than thermal limit of 60 mV/dec. The application of the concept in devices such as FET was theoretically studied by S. Salahuddin et al. [**13**] and later experimentally evidenced in device with ferroelectric gate dielectrics [**14-17**]. Subsequently, the concept has been extended to different gate/channel configurations based on III-nitride materials [**18**,**19**] suggesting that alternative mechanisms can lead to a negative capacitance FET (NCFET), such as spontaneous polarization [**18**] and piezoelectricity [**19],** although the latter is currently under debate as possible origin of NC effect [**20**].

Recently, there has been progress in this field, Si NC FETs [**21**] and NC FinFETs [**22**] with ferroelectric gates have been demonstrated although there is still a concern about the speed of these devices due to slow ferroelectric switching times (typically~ 100-200 psec).

A good alternative to overcome these problems could be the use of two-dimensional (2D) metallic systems, which possess a quantum capacitance (QC) [**10**] comparable to the geometrical capacitance of ultrathin gate dielectrics for certain conditions. The use of 2D quantum metal with a finite QC has been theoretically proposed [**23**] in combination with ferroelectrics in order to stabilize the NC regime of ferroelectric gates. Also, it has been predicted [**12**] that in 2D metallic systems and in the regime of low density of states (DOS), strong electron correlation effects could become dominant and indeed give negative contributions to the QC. Graphene has a very low density of states and carrier density n when the Fermi energy (E_F) is located near the Dirac point. Moreover, predictions [**24**] and experimental evidence [**25**,**26**] of negative QC in graphene [**25**] and BN/graphene nanocapacitors [**26**] have been published. Additionally, negative electronic compressibility after all related to NC, has been reported in MoS_2 2D semiconductor in contact with graphene [**27**].

4.3 Experimental Results

To build the MIS divice with embed graphene such as the one shown in **Figure 1**, single layer graphene is grown on Cu foil by Chemical Vapor Deposition (CVD) method in a commercial 4-inch cold-wall reactor system [**28**] using methane as the carbon precursor. The graphene layer is transferred on thermal SiO_2/n and p-type, H_2-passivated Si wafers. Starting from basic transfer methodologies [**29]** we introduce some modifications that have been used lately [**30-32]** to improve the quality of the graphene transferred on SiO_2. That means using low molecular weight and low concentration resists as well as HCl residue removal. In order to minimize the resist residues, an ultrahigh vacuum (UHV) annealing of graphene at 300°C for one hour prior to Al_2O_3 deposition was performed as also seen in other works [**33**,**34]**.

To encapsulate graphene, a thin layer of Al_2O_3 is grown on graphene in UHV system by plasma assisted deposition in two steps at 200°C. First we perform a mild oxidation of Al in molecular O_2 at a pressure of $\sim 7\times10^{-6}$ Torr up to 2 nm of Al_2O_3 thickness to avoid reaction with graphene, followed by Al_2O_3 deposition using a remote RF plasma source (P_{rf}~210 Watt, $P_{O2}\sim 2\times10^{-5}$ Torr) which produces reactive atomic O beams to obtain 3 nm and 9 nm of good quality oxide (total Al_2O_3 thickness ~5 nm and 11 nm). The first mild Al oxidation step employed in this work is a variant of the methodolgy used previously [**35**,**36**] according to which an ultrathin Al nucleation layer is first deposited in UHV followed by oxidation either in ambient or oxygen atmosphere to form an initial seed layer. Then, Al_2O_3 growth continues by thermal ALD [**35**], O_2 plasma assisted ALD [**37**] or plasma assisted atomic oxygen deposition as in the present work. This initial oxidation is proven to be successful [**35-37**], resulting in good quality interfaces between graphene and Al_2O_3. The first step is critical to ensure a smooth oxidation of Al_2O_3 without harming the graphene layer and subsequently to protect graphene from the reactive atomic O beam used during the second oxidation step. This way, it is not needed to deal with the drawbacks that generate the atomic layer deposited (ALD) oxides on two dimensional materials (e.g HfO_2 on MoS_2), known from previous works [**38**].

Finally, capacitors with diameter of 300-1000μm are fabricated by Hf/Mo metal deposition followed by mild Ar ion milling for mesa isolation. The back ohmic contact is made using eutectic In-Ga alloy to improve the contact resistivity mitigating series resistance effects. Since the graphene layer covers only part of the substrate, control capacitor devices with Al_2O_3/SiO_2 gate dielectrics are defined in the same process sequence on the same wafer and are measured for comparison (**Figure 2**).

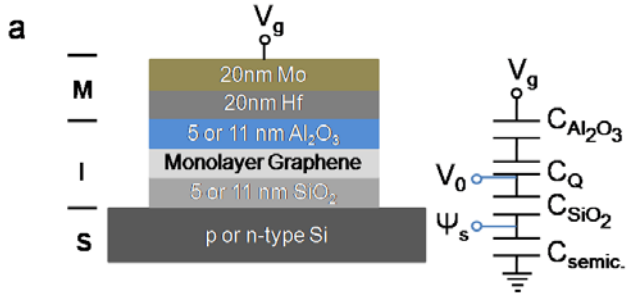

Figure 1.(**a**) Schematic of the complex MIS structure where graphene layer is encapsulated between two oxide layers and the equivalent electronic circuit. C_{Al2O3}, C_{SiO2} are the dielectric capacitances and C_Q, C_{semic} are the graphene quantum capacitance and the semiconductor capacitance, respectively. V_g, V_0 and Ψ_s are the gate bias, the graphene potential and the semiconductor surface potential respectively.

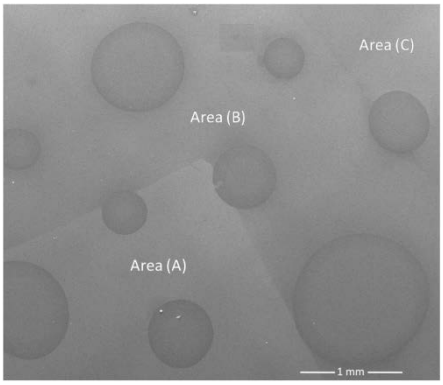

Figure 2. SEM picture of the device using secondary electron imaging. The circular structures are 300-1000μm diameter Mo/Hf metal contacts on top of the three areas. Area (A): 5nm Al_2O_3/SL graphene/5nm SiO_2/Si, Area (B): 5nm Al_2O_3 /5nm SiO_2/Si and Area (C): 5nm SiO_2/Si.

The build of the deviced was followed up in the different steps of the process. Firstly, after the graphene transfer on SiO_2 the sample was meassured by Raman spectroscopy to confirm that the single layer graphene was transferred with a minimum amount of defects [**39**,**40]** as it is shown in **Figure 3a.** Additional measurements with scanning transmision microscopy (STM) (Figure 3b) confirm a crack-free, continuous graphene layer with effectively no residues and minimum density of wrinkles similar to results already reported [**41**].

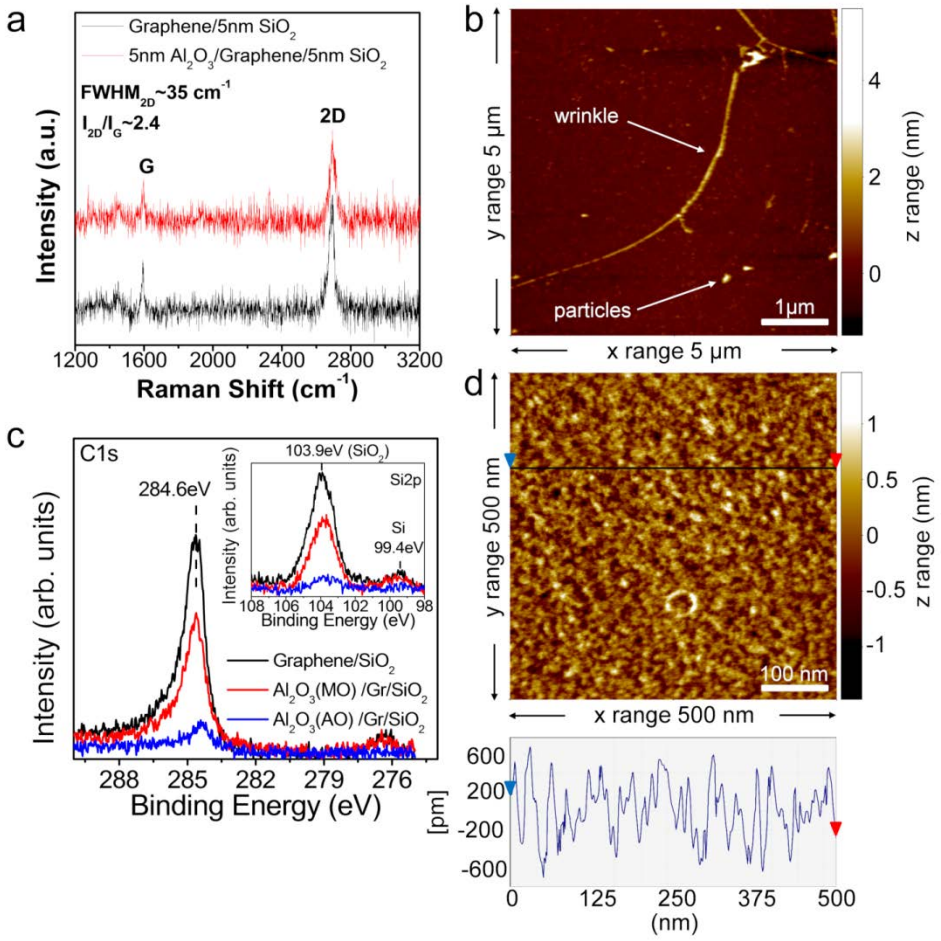

Figure 3.(**a**) Raman spectra of graphene layer transferred on SiO_2 film before (bottom) and after (top) Al_2O_3 deposition. This is characteristic of single layer graphene with I_{2D}/I_G~2.4 and $FWHM_{2D}$~35cm^{-1}. The poor signal to noise ratio is characteristic of Raman spectra on thin SiO_2. (**b**) STM 5μm×5μm image of the transferred graphene layer on the SiO_2 substrate. The particles are not resist residues; they are attributed to contamination due to air exposure. (**c**) C1s XPS spectra of gate stack prior to Al_2O_3 growth (black line), after Al_2O_3 (molecular O) growth (red line) and after Al_2O_3 (atomic O) growth (blue line) indicating that graphene layer remains intact during oxide growth process. The inset shows that Si (SiO_2) peak is reduced along with C peak indicating good coverage of graphene/SiO_2 by Al_2O_3 top dielectric. (**d**) STM 500nm×500nm image of the 5nm Al_2O_3 thin film on top of the single layer graphene and a line scan along the line shown between blue and red triangles. The rms roughness is about ~0.35 nm.

The Al oxidation was verified by in-situ X-ray photoelectron spectroscopy (XPS) as it is shown in **Figure 4**.

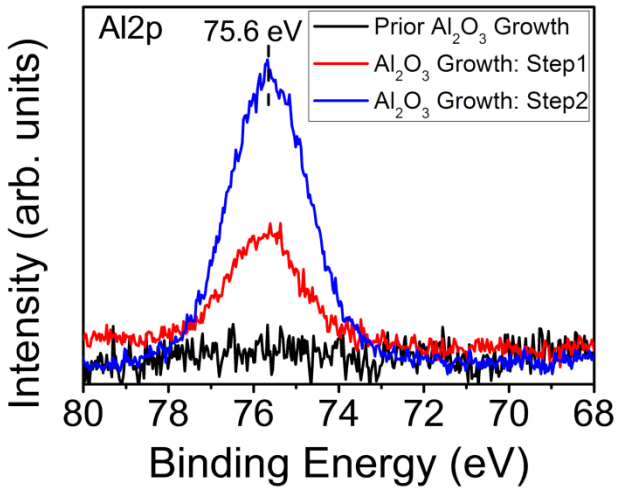

Figure 4. Al2p XPS spectra prior Al_2O_3 growth (black line), after Al oxidation in molecular O_2, (step 1, red line) and after Al_2O_3 growth using rf plasma source (step 2, blue line). Both steps are performed at 200°C.

The samples were measured again by Raman (**Figure 3a**) to verify that graphene remains intact after Al_2O_3 deposition. The process was monitored by in-situ XPS (**Figure 3c**) through all stages of Al_2O_3 deposition to verify that C1s and Si2p peaks are gradually reduced indicating full coverage by Al_2O_3 without harming graphene (the lineshape of the graphene peak (C1s) remains unaffected after successive Al_2O_3 films growth). The surface morphology of Al_2O_3 on graphene is examined by STM (**Figure 3d**) revealing an rms roughness of ~0.35nm, which compares favorably to the rougness of 0.52nm obtained by similar Al_2O_3 deposition methods [**42**].

The normalized Capacitance-Voltage (C-V) measurements of MIS devices for high frequency (1MHz) are shown in **Figure 5** for both n-type (**Figure5a**) and p-type (**Figure 5b**). The measurements present a peak enhancement above the geometrical capacitance C_{geom} which is defined by the dielectric layers. For n-type devices the peak is located between 0.45-0.70V in the accumulation while for p-type devices it is located at -0.35V. The enhancement is more pronounced for thinner gates reaching a 35% over the geometrical capacitance. When the substrate doping increases this effect becomes weaker or even disappears. Similar measurements were carried out in the control samples. In this case, as it can be seen in **Figure 5c**, no peak enhancement was observed, thus the effect is associated to the presence of graphene.

Similar enhancement of the capacitance above the geometrical one in the accumulation has been previously observed and related to negative compressibility originating from electron-electron interactions in the $LaAlO_3/SrTiO_3$ interface [**43**]. This work motivates

the analysis of the capacitance measurements in this chapter taking into consideration possible electron correlation effects in graphene.

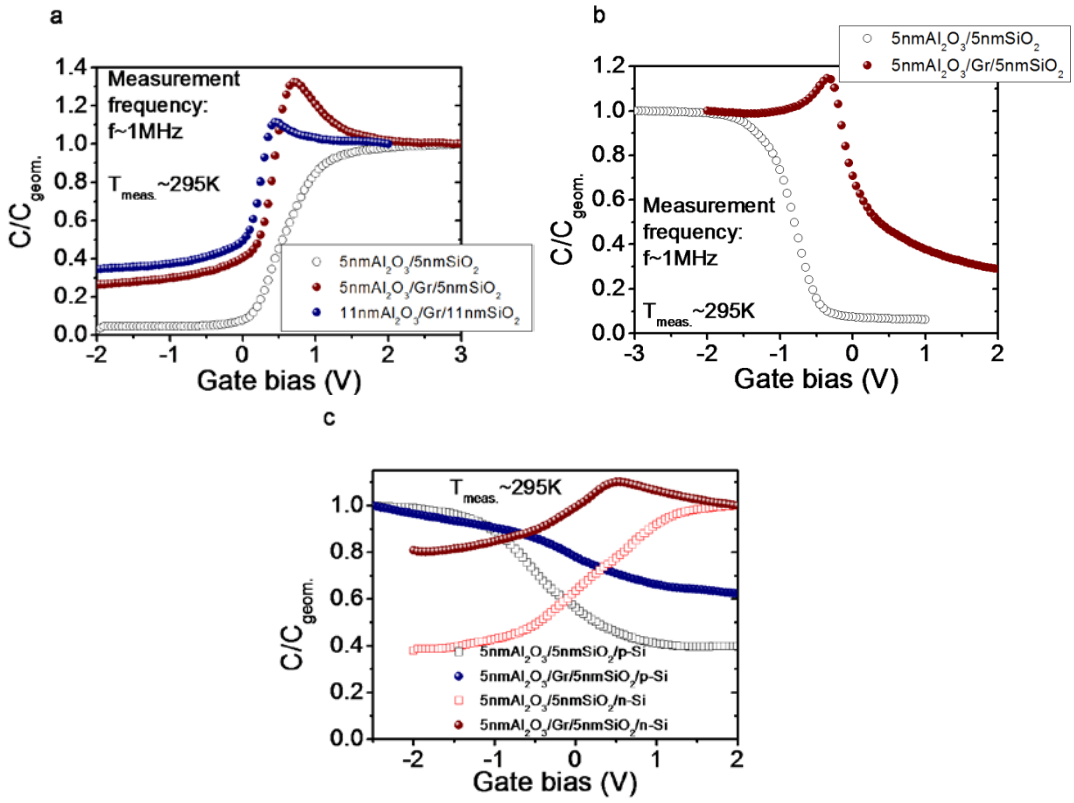

Figure 5.(**a**) Normalized experimental high frequency (1MHz) C-V characteristics for graphene-encapsulated and control MIS structures on n-type Si substrates of ρ=1-5 Ω-cm (~$9x10^{14}$ - $5x10^{15}cm^{-3}$). The graphene-encapsulated structures exhibit capacitance enhancement above the geometrical capacitance C_{geom}, occurring at ~0.45-0.7eV in accumulation. The enhancement peak is more pronounced in the thinner gate stack (brown dots) and reaches a value of 35%. (**b**) Normalized experimental C-V characteristics for graphene-encapsulated and control MIS structures on p-type Si substrates of ρ=1-5Ω-cm (~$3x10^{15}cm^{-3}$ - $2x10^{16}cm^{-3}$). The graphene-encapsulated structure exhibits capacitance enhancement of 15% above the geometrical capacitance C_{geom} occurring at ~ -0.35eV in accumulation. (**c**) Normalized experimental C-V characteristics for graphene-encapsulated and control MIS structures on n and p-type Si substrates of ρ=0.06-0.09Ω-cm (~ 1-$2x10^{17}cm^{-3}$) and ρ=0.08-0.10Ω-cm (~ 3-$4x10^{17}cm^{-3}$) respectively. The enhancement peaks in these higher doped MIS are less pronounced or not detectable.

Based on the equivalent circuit in **Figure 1a**, the total gate capacitance C_g per unit area is modeled as two capacitances in series, namely the geometrical capacitance C_{geom} $(C_{geom}^{-1} = C_{SiO2}^{-1} + C_{Al2O3}^{-1})$ and the quantum capacitance C_Q of graphene:

$$C_g^{-1} = C_{geom}^{-1} + C_Q^{-1} \quad (4.5)$$

where the quantum capacitance C_Q^{-1} was previously defined by equation 4.4. While the analysis of the quantum capacitance made in the section 4.2 pertains, in general, to conventional 2D electron systems [**12**], it could be applicable also, as a first approximation, to graphene/dielectric complexes to illustrate the NC effect and its possible relevance to the experimental observations in **Figure 5**. Nevertheless, for a more accurate analysis, adaptations in exchange interaction and kinetic terms may be required, especially in order to take into account the linear energy dispersion *E-k* in ideal graphene near the Dirac point which is different from the typical quadratic relation valid for conventional electrons systems.

Addressing a first approach, it can be assumed that n depends linearly on the potential V_0 at the graphene/oxide interface (**Figure 1a**) varying as $n = e\rho_{EF}^{(2D)}V_0$ [**23]** while from Gauss's law $V_0 = \Psi_s - (Q_s(\Psi_s)/C_{SiO2})$. These two equations relate n to the semiconductor charge Q_s controlled by the surface potential Ψ_s [**44**]. This result is a variable gate capacitance C_g which is coupled through through *n* to Q_s (or Ψ_s) (**Equation 4.5 and 4.4**). Application of Gauss's law once more gives the state equation

$$(V_g - \Psi_s)C_g(\Psi_s) = -Q_s(\Psi_s) \quad (4.6)$$

which can be solved numerically to obtain Ψ_s (and Q_s) as well as the total capacitance $C=dQ_s/dV_g$ as functions of V_g. These quantities are plotted in **Figure 6** for the case of n-type MIS. A steeper variation of Ψ_s near the conduction band and a corresponding differential gain $d\Psi_s/dV_g > 1$ in the inset (**Figure 6a**) signify internal gate amplification as a result of negative contributions in C_Q (**Equation 4.4**).

The calculated normalized C-V_g characteristics are plotted in **Figure 6b** showing a pronounced capacitance enhancement peak near 0.3V in accumulation, which is associated to the gain peak in the inset of **Figure 6a**. The calculated capacitance agrees qualitatively with the experimental results in **Figure 5a**. A discrepancy in the peak position between theory (0.23V) and experiment (0.7 V) is attributed to a small flatband voltage shift. From **Figure 5a**, the flat band voltage is estimated to be ~0.4V therefore, the peak is located 0.3V away from the flatband voltage which agrees reasonably well with the corresponding theoretical value of ~0.23V (**Figure 6b**).

A reduction of the peak enhancement, such as the ones previously meassured (**Figure 5a**), is also predicted by our model as it can be seen in **Figure 6b** when thicker oxides are used. That may occur due to the dominance of the geometrical capacitance in these cases. The disagreement between the experimental and theoretical C-V in the inversion region (negative gate bias in n-type MIS), is attributed to the well-known effect that minority carriers respond slowly so at high frequencies no inversion layer can be formed and the experimental capacitance is low.

Quantitative agreement also appears to be remarkably good.The model reproduces the 35% peak enhancement of the experiment by using m* =0.012m_0 [**45**] and setting ε_{eff} near unity, which is close to the value of 2.3 reported [**46**] for the dielectric constant of graphene on SiO_2. The small discrepancy may be attributed to the uncertainties in the doping concentration of the Si substrate and the graphene effective mass. The small deviation may also be due to the approximations used in our analysis. One such approximation is made in **Equation 4.4** where, for simplification purposes, the additional negative terms C_{el-el}^{-1} which could be originated from electron-electron interactions[**12**], are ignored. Inclusion of such terms enhance the negative contributions increasing ε_{eff} closer the expected value.

In principle, the presence of wrinkles (**Figure 3b**) could have an influence on C_Q and the total capacitance. But the proportion of areas with wrinkles are less than these free-wrinkle areas of graphene, so the capacitance originated in areas with wrinkles in paralle with the one originating from the other areas has to be small so their contribution to the total C_Q can be considered negligible in a first aproximation.

On the other hand, the presence of puddles of electrons and holes [**47-49**] originating from charged impurities in graphene could cause deviations from ideality modifying the carrier density n_s near the Dirac point in the $n_s \sim 0 - 8\times10^{11}cm^{-2}$ range [**48,49]**. However, at higher $n_s \sim 4\times10^{12}cm^{-2}$ where the NC effect (enhancement peak in **Figure 5**) occurs, carrier dynamics are least affected by puddles and the model, although not taking them into account, it is expected to describe accurately the C-V characteristics.

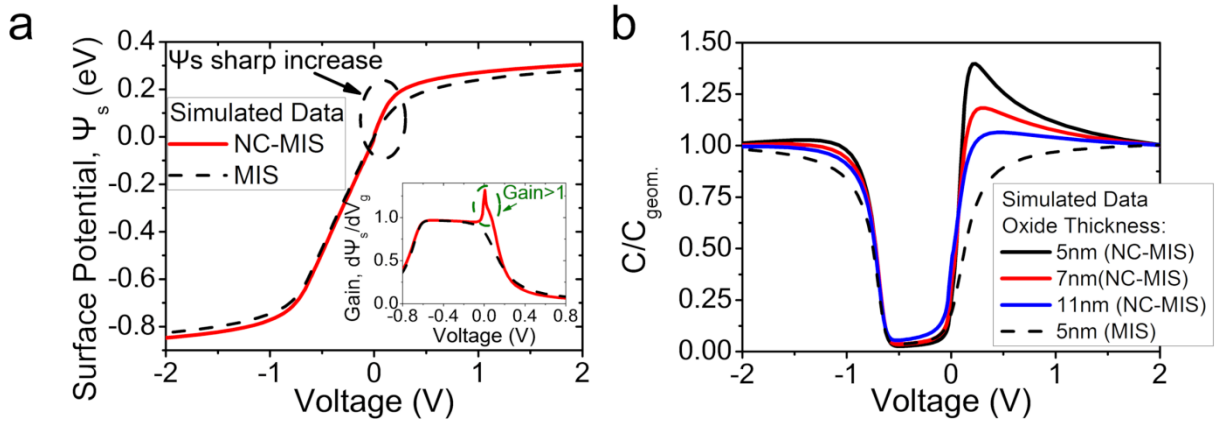

Figure 6.(**a**) Semiconductor surface potential Ψ_s versus applied gate bias according the simulation model described in the text for a conventional MIS (thin dotted black line) and the graphene-encapsulated (thick red line) MIS with the same geometrical capacitance. A steep slope of surface potential clearly appears (circled area) as a result of negative C_Q. Parameter values for simulation are chosen to be close to experimental parameters for a better comparison: N_D~10^{15}cm^{-3}, d_{Al2O3}~5nm, d_{SiO2}~5nm. Inset shows the differential gain versus bias plot for the same parameters where a gain greater than 1 is observed. (**b**) Simulated C-V curves showing capacitance enhancement above the geometrical capacitance C_{geom} for an n-type MIS (N_D = 10^{15}cm^{-3}) with graphene-encapsulated gate stacks of different total thickness. Dotted line represents a conventional MIS without graphene. The simulation shows capacitance enhancement peaks at around ~0.21-0.44V in accumulation, in qualitative agreement with the experiment.

The modeling results in the present work agree with previous simulation data on capacitors with ferroelectric gates [**50**] where a similar capacitance enhancement peak below 1V in accumulation was also predicted and associated with NC effects. The ability of our model to reproduce the main experimental characteristics, capturing their trend with respect to the gate thickness and the Si semiconductor doping variations suggests that the observed capacitance enhancement peak near accumulation in MIS devices could be regarded as a signature of NC. In our case, the negative capacitance stems from the fact that the additional charge stored in the gate capacitor reduces the electrostatic energy E due to exchange correlation effects in the graphene layer. This could lead to gain (**Figure 6a**) in the expense of the internal energy of the correlated electron system (graphene). For better illustration, $E = Q_s^2/2C_g$ is plotted (**Figure 7**) as a function of semiconductor charge Q_s. A minimum is obtained at finite negative values of Q_s in an n-type MIS, showing the reduction of the electrostatic energy below the expected value in a conventional capacitor.

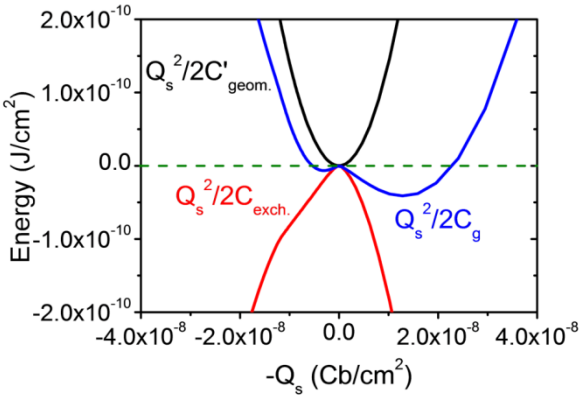

Figure 7. The electrostatic energy E built in the MIS as a function of the semiconductor charge $-Q_s$, broken down in the positive geometrical and negative exchange interaction components. In x-axis, $-Q_s$ is used instead of Q_s in order to have consistency with the capacitance enhancement phenomenon (see **Figure 6b**) which appears in the positive part of the voltage x-axis.

So graphene can be suggested as a candidate material for integration in the gate of NCFETs. The NC effect could be potentially enhanced by making the C_Q dominant in series with C_{geom} which can be achieved by either reducing the SiO_2 and/or Al_2O_3 thickness or by using higher k dielectrics such as HfO_2 in place of Al_2O_3 in order to increase C_{geom}. Other 2D electron systems such as the ones formed at $SrTiO_3/LaAlO_3$ crystalline interfaces [**44**] could present enhanced electron-correlation effects and are potential candidates for NC FET, provided that they show sufficient insulation as required for the gates of aggressively scaled advanced electronic devices.

Other 2D materials with similar properties could be also good candidates for NC FET. Materials such as ultrathin topological insulators (TI) [**51**], like Bi_2Se_3, possessing surface metallic states in the form of a Dirac cone similar to graphene could have a (negative) quantum capacitance that can be used in TI-encapsulated gate stacks similar to the graphene-based ones investigated in this chapter.

The device architecture studied is similar to Si MOSFET devices so it could be suitable for CMOS technology. The dielectrics proposed at the gate (SiO_2 and Al_2O_3) are known materials, scalable to large area wafers and are already used in advanced CMOS. Also, there has been considerable progress in using graphene in compatibility with advanced semiconductor processing.

4.4 Conclusions

This study has managed to encapsulate single layer graphene into the Si p-and n-type MIS capacitors structure, while exploring the possible influence of the quantum capacitance of graphene on the C-V characteristics. The capacitance enhancement peaks were measured at around 0.35-0.70V in accumulation, which reaches up to 35 % above the geometrical capacitance at room temperature. This effect is more pronounced for thin oxide films and low doped semiconductor substrates. Based on the MIS device modeling the peak enhancement is attributed to the negative quantum capacitance contributions due to exchange interaction effects in graphene.

References

[**1**] A. H. Castro Neto, F. Guinea, N. M. R. Peres, K. S. Novoselov, and A. K. Geim, Rev. Mod. Phys. 81, 109.
[**2**] D. P. DiVincenzo and E. J. Mele, PRB 29, 4 (1984)
[**3**] Y.-W. Son, M. L. Cohen and S. G. Louie, PRL 97, 216803 (2006)
[**4**] W. Wei and T. Jacob, PRB 87, 115431 (2013)
[**5**] J. T. Robinson, J. S. Burgess, C. E. Junkermeier, S. C. Badescu, T. L. Reinecke, F. K. Perkins, M. K. Zalalutdniov, J. W. Baldwin, J. C. Culbertson, P. E. Sheehan, and E. S. Snow, Nano Lett. 2010, 10, 3001–3005
[**6**] L. Britnell, R. V. Gorbachev, R. Jalil, B. D. Belle, F. Schedin, A. Mishchenko, T. Georgiou, M. I. Katsnelson, L. Eaves, S. V. Morozov, N. M. R. Peres, J. Leist, A. K. Geim, K. S. Novoselov, L. A. Ponomarenko, Science Vol 335, Issue 6071, pp 947-950 (2012)
[**7**] T. Georgiou, R. Jalil, B. D. Belle, L. Britnell, R. V. Gorbachev, S. V. Morozov, Y.-J. Kim, A. Gholinia, S. J. Haigh, O. Makarovsky, L. Eaves, L. A. Ponomarenko, A. K. Geim, K. S. Novoselov, A. Mishchenko, Nature Nanotechnology 8, 100–103 (2013)
[**8**] G. Shi, Y. Hanlumyuang, Z. Liu, Y. Gong, W. Gao, B. Li, J. Kono, J. Lou, R. Vajtai, P. Sharma, P. M. Ajayan, Nano Lett. 2014, 14, 1739−1744
[**9**] B. K. Min, S. K. Kim, S. J. Kim, S. H. Kim, M.-A Kang, C.-Y. Park, W. Song, S. Myung, J. Lim, K.-S. An, Scientific Reports 5, 16001 (2015)
[**10**] S. Luryi, *Appl. Phys. Lett*. **1988**, 52, 501
[**11**] T. Ando, A. B. Fowler and F. Stern, Rev. Mod. Phys. 54, 437 (1982)
[**12**] T. Kopp, J. Mannhart, *J. Appl. Phys.* **2009**, 106, 064504
[**13**] S. Salahuddin, S.Datta, *Nano Lett.* **2008**, 8, 405-410
[**14**] A. Rusu, G. A. Salvatore, D. Jiménez, A. M. Ionescu, *IEEE Int. Electron Devices Meet.* **2010**, 16.3.1-16.3.4
[**15**] D. J. R. Appleby, N. K. Ponon, K. S. K. Kwa, B. Zou, P. K. Petrov, T. Wang, N. M. Alford, A. O'Neill, *Nano Lett.* **2014**, 14, 3864-3868
[**16**] W. Gao, A. Khan, X. Marti, C. Nelson, C. Serrao, J. Ravichandran, R. Ramesh, S. Salahuddin, *Nano Lett.* **2014**, 14, 5814-5819
[**17**] A. I. Khan, K. Chatterjee, B. Wang, S. Drapcho, L. You, C. Serrao, S. R. Bakaul, R. Ramesh, S. Salahuddin, *Nat. Mater.* **2015**, 14, 182-186
[**18**] H. W. Then, S. Dasgupta, M. Radosavljevic, L. Chow, B. Chu-Kung, G. Dewey, S. Gardner, X. Gao, J. Kavalieros, N. Mukherjee, M. Metz, M. Oliver, R. Pillarisetty, V. Rao, S. H. Sung, G. Yang, R. Chau, *IEEE Int. Electron Devices Meet.* **2013**, 28.3.1-28.3.4
[**19**] R. K. Jana, A. Ajoy, G. Snider, D. Jena, *IEEE Int. Electron Devices Meet.* **2014**, 13.6.1-13.6.4

[**20**] J. C. Wong, S. Salahuddin, *IEEE Int. Electron Devices Meet.* **2014**, 13.5.1-13.5.4
[**21**] M. H. Lee, P. G. Chen, C. Liu, K. Y. Chu, C. C. Cheng, M. J. Xie, S. N. Liu, J. W. Lee, S. J. Huang, M. H. Liao, M. Tang, K. S. Li, M. C. Chen, *IEEE Int. Electron Devices Meet.* **2015**, 22.5.1-22.5.4
[**22**] K. S. Li, P. G. Chen, T. Y. Lai, C. H. Lin, C. C. Cheng, C. C. Chen, Y. J. Wei, Y. F. Hou, M. H. Liao, M. H. Lee, M. C. Chen, J. M. Sheih, W. K. Yeh, F. L. Yang, S. Salahuddin, C. Hu, *IEEE Int. Electron Devices Meet.* **2015**, 22.6.1-22.6.4
[**23**] D. J. Frank, P. M. Solomon, C. Dubourdieu, M. M. Frank, V. Narayanan, T. N. Theis, *IEEE Trans. Electron Dev.* **2014**, 61, 2145-2153
[**24**] R. Reiter, U. Derra, S. Birner, B. Terrés, F. Libisch, J. Burgdörfer, C. Stampfer, *Phys. Rev. B* **2014**, 89, 115406
[**25**] L. Wang, Y. Wang, X. Chen, W. Zhu, C. Zhu, Z. Wu, Y. Han, M. Zhang, W. Li, Y. He, W. Xiong, K. T. Law, D. Su, N. Wang, *Sci. Rep.* **2013**, 3, 02041
[**26**] G. Shi, Y. Hanlumyuang, Z. Liu, Y. Gong, W. Gao, B. Li, J. Kono, J. Lou, R. Vajtai, P. Sharma, P. M. Ajayan, *Nano Lett.* **2014**, 14, 1739-1744
[**27**] S. Larentis, J. R.Tolsma, B. Fallahazad, D. C. Dillen, K. Kim, A. H. Mac Donald, E.Tutuc, *Nano Lett*. **2014**, 14, 2039−2045
[**28**] J. Marquez-Velasco, N. Kelaidis, E. Xenogiannopoulou, Y. S. Raptis, D. Tsoutsou, P. Tsipas, Th. Speliotis, G. Pilatos, V. Likodimos, P. Falaras, A. Dimoulas, *Appl. Phys. Lett.* **2013**, 103, 213108
[**29**] X. Li, Y. Zhu, W. Cai, M. Borysiak, B. Han, D. Chen, R. D. Piner, L. Colombo, R. S. Ruoff, *Nano Lett.* **2009**, 9, 4359-4363
[**30**] G. B. Barin, Y. Song, I. F. Gimenez, A. G. S. Filho, L. S. Barreto, J. Kong, *Carbon* **2015**, 84, 82-90
[**31**] H. J. Jeong, H. Y. Kim, S. Y. Jeong, J. T. Han, K. J. Baeg, J. Y. Hwang, G. W. Lee, *Carbon* **2014**, 66, 612-618
[**32**] G. Deokar, J. Avila, I. Razado-Colambo, J. L. Codron, C. Boyaval, E. Galopin, M. C. Asensio, D. Vignaud, *Carbon* **2015**, 89, 82-92
[**33**] A. Pirkle, J. Chan, A. Venugopal, D. Hinojos, C. W. Magnuson, S. McDonnell, L. Colombo, E. M. Vogel, R. S. Ruoff, R. M. Wallace, *Appl. Phys. Lett.* **2011**, 99, 122108
[**34**] J. Chan, A. Venugopal, A. Pirkle, S. McDonnell, D. Hinojos, C. W. Magnuson, R. S. Ruoff, L. Colombo, R. M. Wallace, E. M. Vogel, *ACS Nano* **2012**, 6, 3224-3229
[**35**] S. Kim, J. Nah, I. Jo, D. Shahrjerdi, L. Colombo, Z. Yao, E. Tutuc, S. K. Banerjee, *Appl. Phys. Lett*. **2009**, 94, 062107
[**36**] A. Pirkle, R. M. Wallace, L. Colombo, *Appl. Phys. Lett*. **2009**, 95, 133106
[**37**] O.M. Nayfeh, T. Marr, M. Dubey, *IEEE. Electron. Dev. Lett*. **2010,** 32, 473
[**38**] S. McDonnell, B. Brennan, A. Azcatl, N. Lu, H. Dong, C. Buie, J. Kim, C. L. Hinkle, M. J. Kim, R. M. Wallace, *ACS Nano* **2013**, 7, 10354-10361
[**39**] Y. Y. Wang, Z. H. Ni, T. Yu, Z. X. Shen, H. M. Wang, Y. H. Wu, W. Chen, A. T. S. Wee, *J. Phys. Chem. C* **2008**, 112, 10637-10640

[**40**] Y. Hao, Y. Wang, L. Wang, Z. Ni, Z. Wang, R. Wang, C. K. Koo, Z. Shen, J. T. L Thong, *Small* **2010**, 6,195-200
[**41**] J. D. Wood, G. P. Doidge, E. A. Carrion, J. C. Koepke, J. A. Kaitz, I. Datye, A. Behnam, J. Hewaparakrama, B. Aruin, Y. Chen, H. Dong, R. T. Haasch, J. W. Lyding, E. Pop, *Nanotechnology* **2015**, 26, 055302
[**42**] B. Fallahazad, K. Lee, G. Lian, S. Kim, C. M. Corbet, D. A. Ferrer, L. Colombo, E. Tutuc, *Appl. Phys. Lett.* **2012**, 100, 093112
[**43**] L. Li, C. Richter, S. Paetel, T. Kopp, J. Mannhart, R. C. Ashoori, *Science* **2011**, 332, 825-828
[**44**] S. M. Sze, Physics of Semiconductor Devices, 2nd Ed., John Wiley & Sons, **1981**, p. 368
[**45**] E. Tiras, S. Ardali, T. Tiras, E. Arslan, S. Cakmakyapan, O. Kazar, J. Hassan, E. Janzen, E. Ozbay, *J. Appl. Phys.* **2013**, 113, 043708
[**46**] E. H. Hwang, S. Das Sarma, *Phys. Rev.B* **2007**, 75, 205418
[**47**] J. Martin, N. Akerman, G. Ulbricht, T. Lohmann, J. H. Smet, K. Von Klitzing, A. Yacoby, *Nat. Phys.* **2008**, 4, 144-148
[**48**] J. Xia, F. Chen, J. Li, N. Tao, *Nat. Nanotech.* **2009**, 4, 505-509
[**49**] L. A. Ponomarenko, R. Yang, R. V. Gorbachev, P. Blake, A. S. Mayorov, K. S. Novoselov, M. I. Katsnelson, A. K. Geim, *Phys. Rev. Lett.*, **2010**, 105, 136801
[**50**] D. Jiménez, E. Miranda, A. Godoy, *IEEE Trans. Electron Devices* **2010**, 57, 2405-2409
[**51**] P. Tsipas, E. Xenogiannopoulou, S. Kassavetis, D. Tsoutsou, E. Golias, C. Bazioti, G. P. Dimitrakopulos, P. Komninou, H. Liang, M. Caymax, A. Dimoulas, *ACS Nano* **2014**, 8, 6614-6619

Chapter 5

First-principles calculations

5.1 Introduction

Density functional theory (DFT) is one of the most efficient methods to study the ground state properties of many-electron systems [**1**]. As it has been explained in chapter 2, DFT simplifies the many-body interacting systems by describing the problem through the particle density. By providing some structural information and the exchange-correlation potential for the constituent atoms, many physical properties can be determined such as equilibrium lattice parameters, elastic moduli, relative stabilities of competing crystal structures or energies associated with defects or impurities. Additionally, DFT can obtain information about charge density, electronic densities of states and band structures.

In this manner, DFT is a powerful tool to study the properties of new materials before growing them or to give a theoretical explanation to experimental data that have been revealed lately with the study of 2D materials such as graphene [**2**,**3**], silicene [**4**] and Transition Metal Dichalcogenides (TMD) [**5**] or the study of other appealing systems such as topological insulators [**6**] or Weyl semimetals [**7**].

The aim of this chapter is to study structures involving graphene on different dielectrics and metal substrates, in order to understand how the different layers are stacked and to obtain the electronic properties of these systems. For this matter, 2D dielectrics were used (h-AlN, h-BN, $MoSe_2$ or $HfSe_2$) as well as different metals (Ag111, Ni111 and $TaSe_2$) during the DFT calculations. Lastly, this chapter addresses how DFT can be used to prove experimental results in systems such as $TaSe_2$ [**8**], $ZrSe_2$ [**9**] and $HfSe_2$ [**10**].

5.2 Experimental methods

The DFT calculations have been performed using the Vienna ab initio simulation package (VASP) [**11,12**] within generalized gradient approximation (GGA) using the Perdew-Burke-Ernzerhof function (PBE) [**13**]. Local Density Approximation potentials were also used [**14**]. Van der Waals corrections are implemented using the DFT-D2 method of Grimme [**15**]. The energy cutoff and the k-point grids used depends on the concrete systems, however, the k-points' grid are always within the Monkhorst-Pack method [**16**]. For relaxation calculations the convergence threshold was set as $5x10^{-4}$ eV in energy and $2x10^{-3}$ eV/Å in force. The positions of all the atoms in the supercell were fully relaxed during the geometry optimizations except for the first three metal layers when Ag(111) or Ni(111) slabs were used. In these cases, the bottom layers were fixed at their bulk positions.

5.3 Results

5.3.1 Graphene on h-AlN/Ag(111)

Firstly, the h-AlN/Ag(111) system was studied to understand how the h-AlN lays on the metal surface. The lattice constant of h-AlN was 3.11Å [**17**] and the lattice constant of the Ag(111) surfaces was 2.89 Å. Since large supercells do not improve the mismatch between both surfaces, a 1x1 h-AlN cell on a 1x1 Ag(111) cell was used. For the simulation of the Ag(111) it was used a slab of six layers. All of the calculations were performed using an energy cutoff of 300 eV and a 9x9x1 k-points grid.

Secondly, we studied the graphene on h-AlN. Since the lattice constant of graphene is 2.46 Å, a supercell was needed to reduce the mismatch. For this matter, a graphene 5x5 supercell on a h-AlN 4x4 supercell was used with the same energy cutoff and the k-points' grid as before and all the atoms were allowed to move during relaxation.

Furthermore, the way the h-AlN layers were stacked was examined. These calculations are important to know how the h-AlN layers are placed on top each other when the number of h-AlN thickness is increased. Finally, the stacking order of the h-AlN layers is determined after relaxation for different configurations.

Lastly, the whole system's structure was considered. Due to the mismatch between graphene and h-AlN it was necessary to use a supercell again. According to the results, the total system consists of a 5x5 single layer graphene (SLG) on a 4x4 h-AlN and 4x4 Ag(111). After that, the silver slab was simulated using three layers due to the limitations occurring from the large number of atoms used. Moreover, only the bottom one was fixed to the bulk positions during the relaxation, using the same energy cutoff and k-points' grid as previously.

In all these calculations a vacuum slab of 24 Å was used in order to avoid the interaction originating from the periodic conditions.

Studying the adsorption energy we are able to know the most favorable configuration of the system.

The adsorption energy is defined as follows

$$E_{ads} = E_0^{tot} - \left(E_0^{h-AlN} + E_0^{Ag(111)}\right) \quad (5.1)$$

where E_0^{tot} is the ground state energy of the total system and E_0^{film} and $E_0^{substrate}$ are the total energies of the isolated thin film layer and the substrate respectively. The adsorption energies (E_{ads}) of other possible positions such as the bridge, the hollow, the Al on-top

Ag or the N on-top Ag were also calculated following the same procedure. The results of these calculations are shown in **Table 1.**

position	**E_{ads}(meV)**
Al on bridge	-175
N on bridge	-83
Al on hollow	-92
N on hollow	-61
Al on-top Ag	-62
N on-top Ag	-195

Table 1. The E_{ads}(meV) per unit cell for the different relative positions between h-AlN and Ag(111)

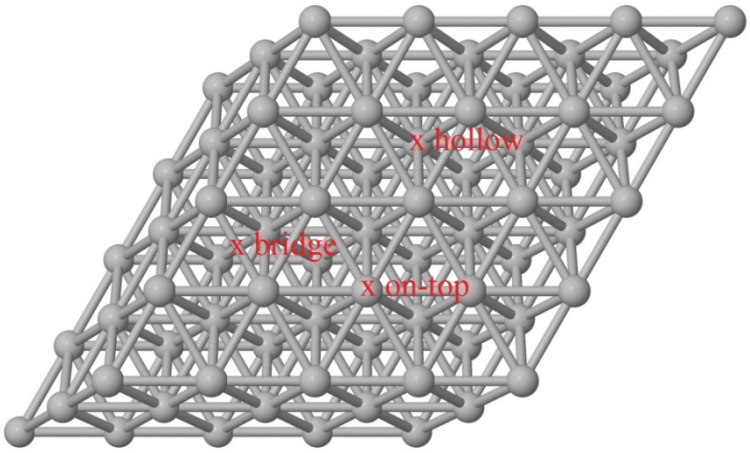

Figure 1. The different relative positions studied (on-top, bridge and hollow positions)

According to the data presented in **Table 1** the N on-top is the position with the highest adsorption energy, so it can be concluded that this is the most favorable of all.

Consecutively, the adsorption energies for the different fixed interlayer distances were considered using the following potentials, LDA, GGA and GGA+vdW. Plotting the adsorption energy versus the distance we were able to define which is the most favorable distance between both systems for each different potential, as there has to be a distance that minimizes the adsorption energy. The results for the GGA potential yield a minimum at 2.7 Å, for the LDA at 2.4 Å and for the GGA+vdW at 2.8 Å. The selected values were finally used as the initial position for the study of the h-AlN/Ag(111).

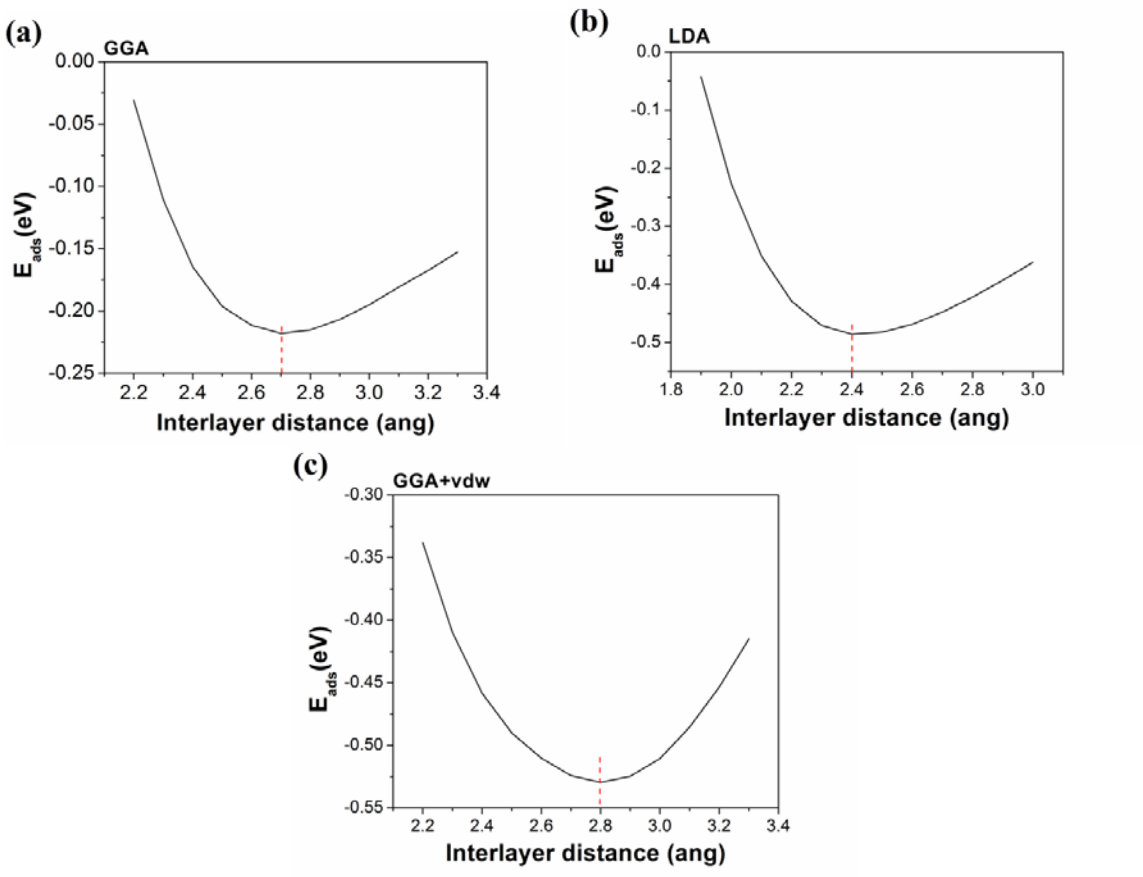

Figure 2 (**a**) GGA potential presents a minimum at 2.7 Å, (**b**) LDA at 2.4 Å, (**c**) GGA+vdW at 2.8 Å, for one layer h-AlN on six layers Ag(111).

Finally the system was fully relaxed, except for the three bottom silver layers of each potential. The interlayer distance between h-AlN and Ag(111) and the buckling (Δ_{AlN}) between N and Al atoms for each potential is shown in Table 2.

xc-functional	Δ_{AlN} (Å)	Interlayer dist.(Å)
GGA	0.1	2.71
LDA	0.13	2.45
GGA+vdW	0.082	2.8

Table 2. Main parameters of the relaxed system, for the h-AlN on Ag(111). Δ_{AlN} is defined as the buckling between the Al atoms and the N atoms.

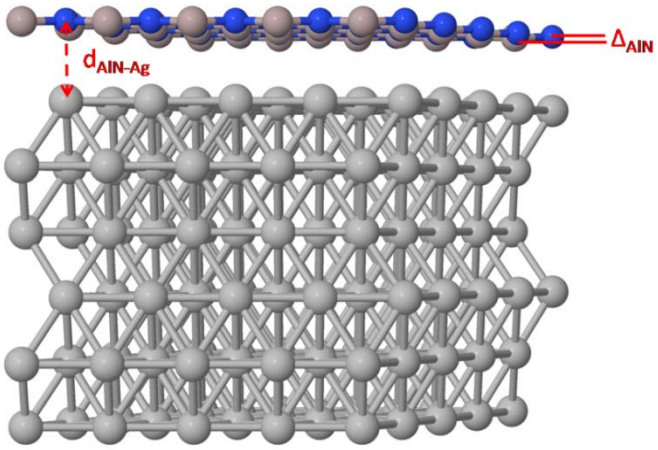

Figure 3. The h-AlN/Ag(111) system after full relaxation

A similar methodology was followed for the system graphene on h-AlN. The relative position of the carbon atoms with respect to the h-AlN was firstly studied. As shown in **Table 3**, the results were very similar between these positions making it impossible to choose a preferred position. That was expected since a large supercell was used in the study. Furthermore, due to the mismatch between graphene and h-AlN all possible positions were covered inside the supercell and for the study to be continued, the as-is position was chosen.

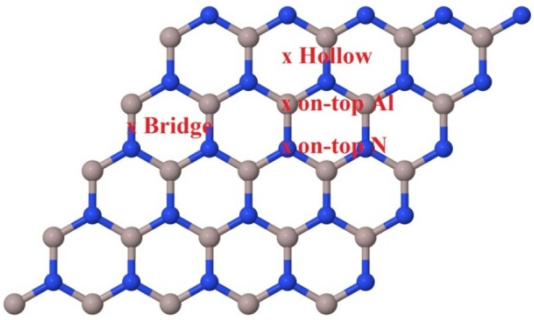

Figure 4. The different relative positions of the carbon atoms on the h-AlN lattice.

position	**E_{ads}(meV)**
As is	-30.04
bridge	-30.18
hollow	-26.3
C on Al	-30.23
C on N	-0.05957

Table 3. The E_{ads}(meV) per unit C atom, for different relative positions of graphene on h-AlN.

Like previously, the interlayer distance was studied. The calculations' results of each different potential are plotted in **Figure 5**. The minimum for the LDA and the GGA+vdW are clearly shown, with interlayer distance between graphene and h-AlN of 3.5 Å for LDA and 3.3 Å for GGA+vdW, and adsorption energies per unit cell of graphene of -0.05 eV and -0.105 eV for LDA and GGA+vdW, respectively. Thus, from this point forward only LDA and GGA+vdW were used in the study.

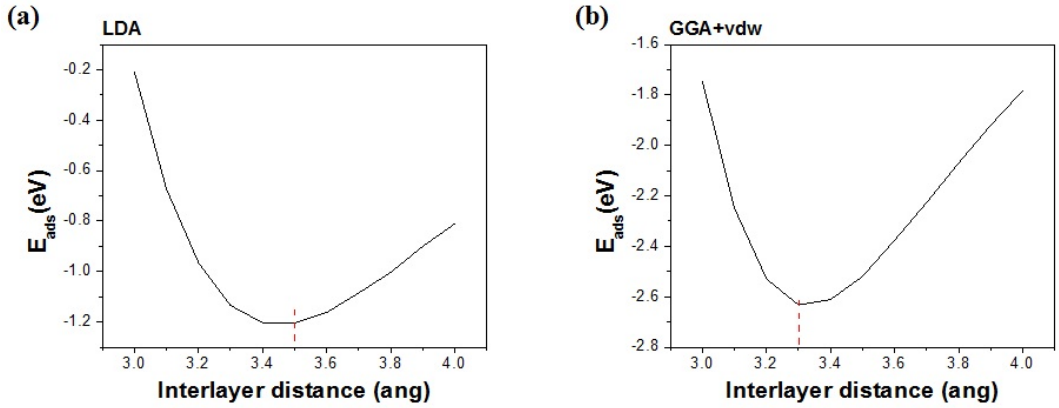

Figure 5. The E_{ads} vs interlayer distance for (a) LDA and (b) GGA+vdW, for the system single layer graphene on one layer of h-AlN. Once the full relaxation was completed, it was found an interlayer distance between graphene and h-AlN of 3.5 Å for LDA and 3.32 Å for GGA+vdW, with an adsorption energy per unit cell of graphene of -0.05 eV and -0.106 eV respectively.

To study the stacking order of h-AlN, two layers of a 1x1 cell of h-AlN were used. There are three different positions that can be distinguished by their symmetry. The first, called AA position, is where the top layer has its Al atoms on-top the Al atoms of the bottom layer and the top N atoms on-top of the N atoms of the bottom layer, respectively. The second, called AA' is where the top layer has the Al atoms on-top the N atoms of the bottom layer and the N atoms of the top layer on top the Al atoms of the bottom layer respectively. The third, called AB position (the Bernal stacking) has its top layer twisted 60° with respect to the bottom layer.

First of all, the adsorption energy of each configuration was studied and the results presented in **Table 4** show that the AA' stacking is the most favorable stacking in agreement with previous works [**18**], since it has the minimum E_{ads} (-0.389 eV). Additionally, the interlayer distance was calculated for the different stacking orders (**Table 4**).

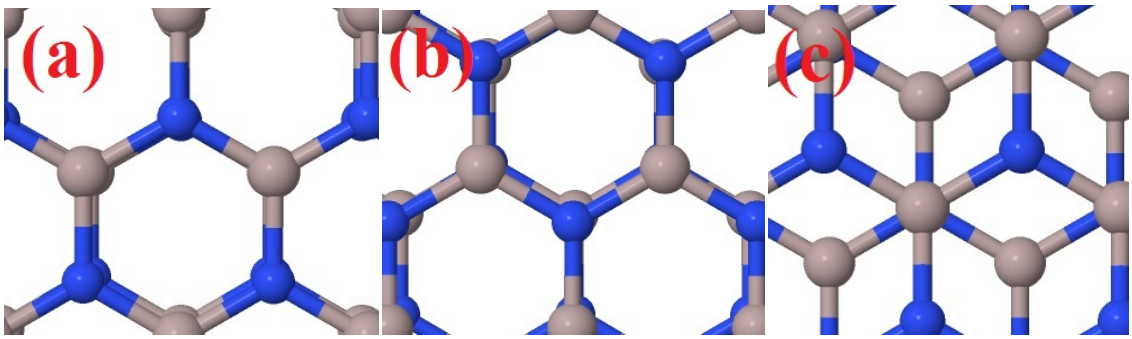

Figure 6. The different stacking orders studied. (**a**) AA, (**b**) AA' and (**c**) AB

	Eads (eV)	**Interlayer distance (Å)**
AA	-0.028	3.5
AA'	-0.389	2.9
AB	-0.203	3

Table 4. The E_{ads}(eV) per unit cell and the interlayer distance for each configuration

Finally, the graphene on h-AlN/Ag(111) system was studied using LDA and GGA+vdW potentials starting from the values so far obtained. As it was mentioned before, this time a three layer slab of silver is used with the bottom layer fixed. **Table 5** presents the main parameters of the system after full relaxation, for one h-AlN layer.

Due to the mismatch between the different layers, the lattice constant used for the h-AlN on Ag(111) is smaller (3.04 Å) than its experimental value (3.11 Å) whereas the graphene on the system has a lattice constant bigger (2.53 Å) than normally, in relation to its experimental value (2.46 Å). The buckling of AlN has decreased for both LDA (0.082 Å) and GGA+vdW (0.075 Å) in relation to the buckling of AlN on Ag(111) without graphene (0.13 Å and 0.082 Å respectively). The interlayer distance between graphene and AlN were found similar for both potentials (3.35 Å and 3.3 Å respectively). Finally, the distance between AlN and Ag(111) was found around 2.8 Å for both potentials in relation to the interlayer distance between AlN and Ag(111) of the AlN/Ag(111) system without graphene, however the distance was found bigger for the LDA potential (2.45 Å).

	a_{gr} (Å)	**a_{aln} (Å)**	**Δ_{AlN} (Å)**	**Gr-AlN (Å)**	**AlN-Ag (Å)**
LDA	2.53	3.04	0.082	3.35	2.79
GGA+vdW	2.53	3.04	0.075	3.3	2.81

Table 5. Main parameters of the system for an LDA and a GGA+vdW potential, for a single h-AlN layer. The graphene lattice constant (a_{gr}), the h-AlN lattice constant (a_{aln}), the buckling of the AlN layers (Δ_{AlN}), the distance between graphene and AlN (Gr-AlN **)** and the distance between AlN and Ag(111) (AlN-Ag).

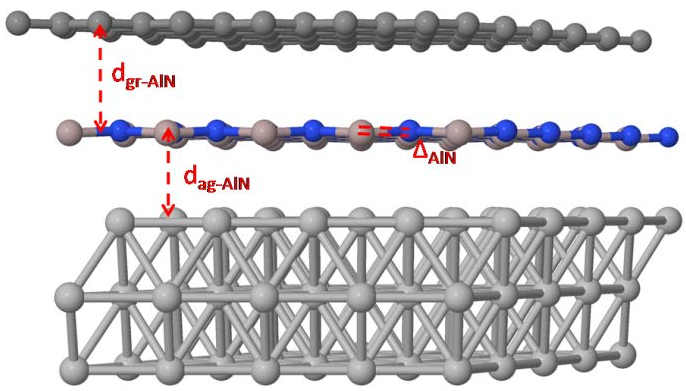

Figure 7. Total system after relaxation for a single layer h-AlN.

The electronic properties of the system for one layer of h-AlN were also studied. **Figure 8** shows the LDOS of graphene for (**a**) graphene on h-AlN and (**b**) graphene on h-AlN/Ag(111). The h-AlN has a band gap of 3.5 eV [**19**] and the graphene exhibits its Dirac cone at Fermi level. When Ag(111) is present the situation changes and the LDOS of graphene loses its linear behavior around Fermi level.

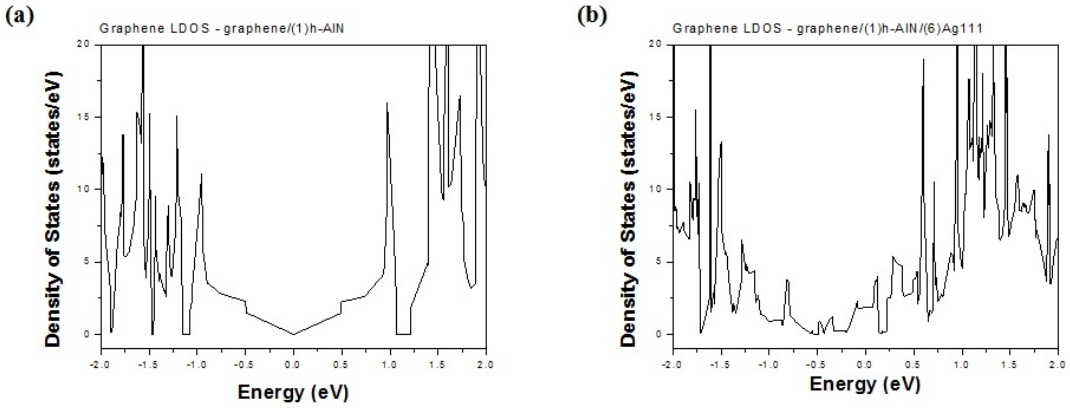

Figure 8. LDOS of graphene for (**a**) graphene-hAlN and (**b**) graphene on one layer of h-AlN on Ag(111)

5.3.2 Graphene on h-BN/Ni(111)

The strategy followed to study this system was the same as the previous one but in this case the values of the lattice constants are close to each other. h-BN has a lattice constant of 2.5 Å [**20**], Ni(111) of 2.49 Å and graphene of 2.46 Å. This allows us to use a stacking of unit cells of all the different materials involved to perform the calculations. To simulate the Ni(111) substrate we used a slab of six Ni layers. All the calculations were performed using an energy cutoff of 350 eV and a 27x27x1 k-points grid as well as a vacuum slab of 30 Å which was used in order to avoid the interaction originating from the periodic conditions.

As it was done for the graphene/h-AlN/Ag(111) system, the adsorption energy was used to determine the most stable configuration, the initial distances between the different layers and the stacking order of the h-BN layers. After these calculations a full-relaxed calculation was carried out to determine the final structure.

In this last case, it was found that we have the most favorable configuration when the B atoms lies on top Ni atom position and N atoms located on hollow positions with an initial distance between hBN and Ni(111) of 3.03 Å. It was also found that one of the carbon atoms in the unit cell prefers to be located on B atoms while the other one is located on hollow position of the hBN lattice. The equilibrium distance between graphene and hBN layer is 3.46 Å. The hBN layers have an AA' stacking which is the most stable stacking with the B atoms above the N atoms. No relevant buckling was observed either in graphene or the h-BN layers.

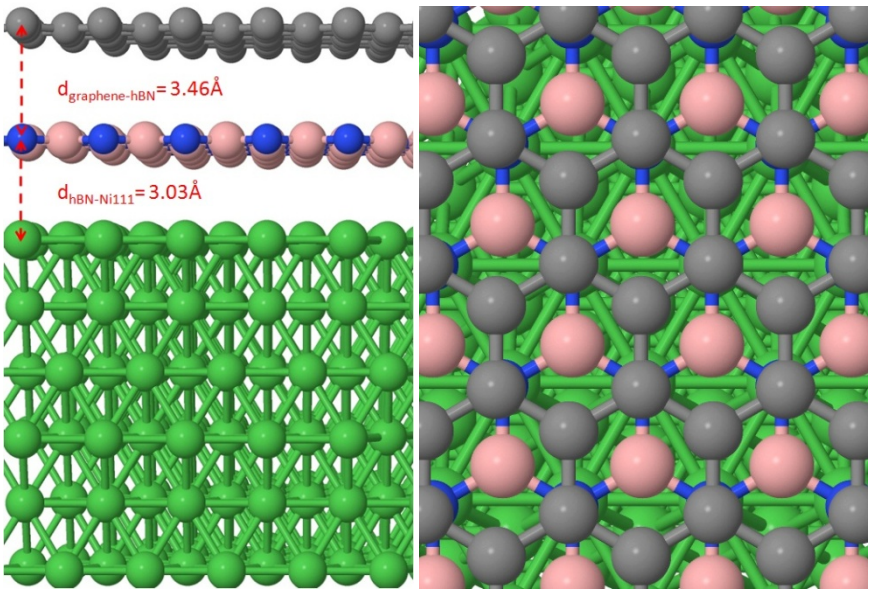

Figure 9. Total system after relaxation. GGA+vdW. Left, lteral view. Right, top view.

As far as the electronic properties of the system are concerned, it is well known that Ni is a magnetic material [**21**], thus, in order to obtain properly the electronic properties of the system we needed to perform spin-polarized calculations.

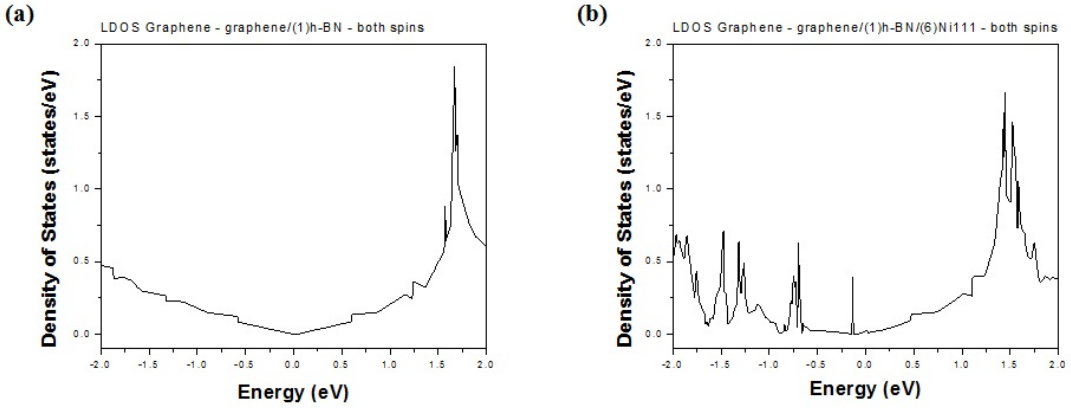

Figure 10. Graphene LDOS of the system **(a)** without Ni and **(b)** with Ni, with one layer of h-BN.

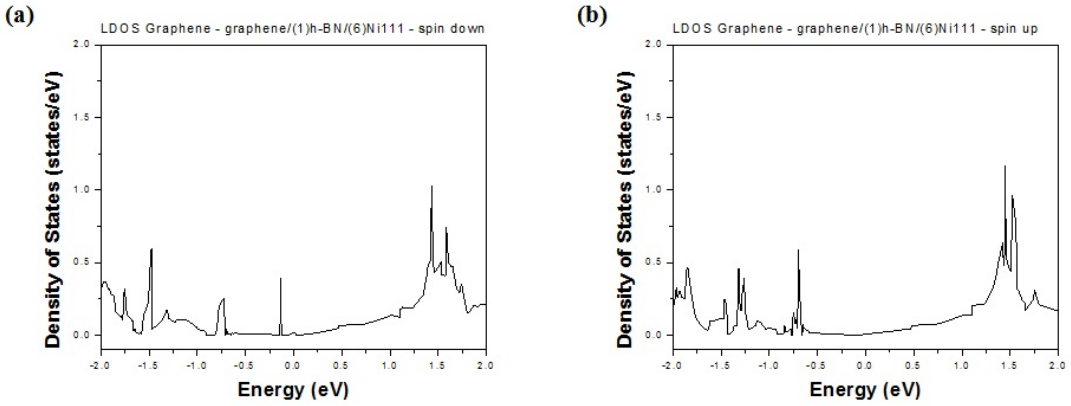

Figure 11. Graphene LDOS. **(a)** Spin down and **(b)** spin up projections for the total system with only one layer of h-BN.

As it is shown in **Figure 11** only the spin down projection has a significant contribution to the graphene LDOS close to the Fermi level. This contribution is expected to decrease or even be suppressed for a larger number of h-BN layers.

5.3.3 Graphene on $HfSe_2$/Ni(111)

$HfSe_2$ has a lattice constant of 3.74 Å [**22**], therefore a supercell was used to reduce the lattices' mismatch. The total system consists of a 3x3 graphene supercell, a 2x2 $HfSe_2$ supercell and a 3x3 Ni(111) supercell. The Ni(111) slab was simulated with six layers. To prevent interaction with the system itself, the calculation was performed with a vacuum slab of 24 Å.

Mostly relative positions between graphene and $HfSe_2$ are covered within the supercell, so the study of the adsorption energy for different positions does not specify a particular result. Something similar occurs between $HfSe_2$ and Ni(111). After full relaxation it was found that the equilibrium distance between $HfSe_2$ and Ni(111) is 3.41 Å and the distance between graphene and $HfSe_2$ is 3.43 Å. **Figure 12** shows the full relaxed graphene/$HfSe_2$/Ni(111) structure.

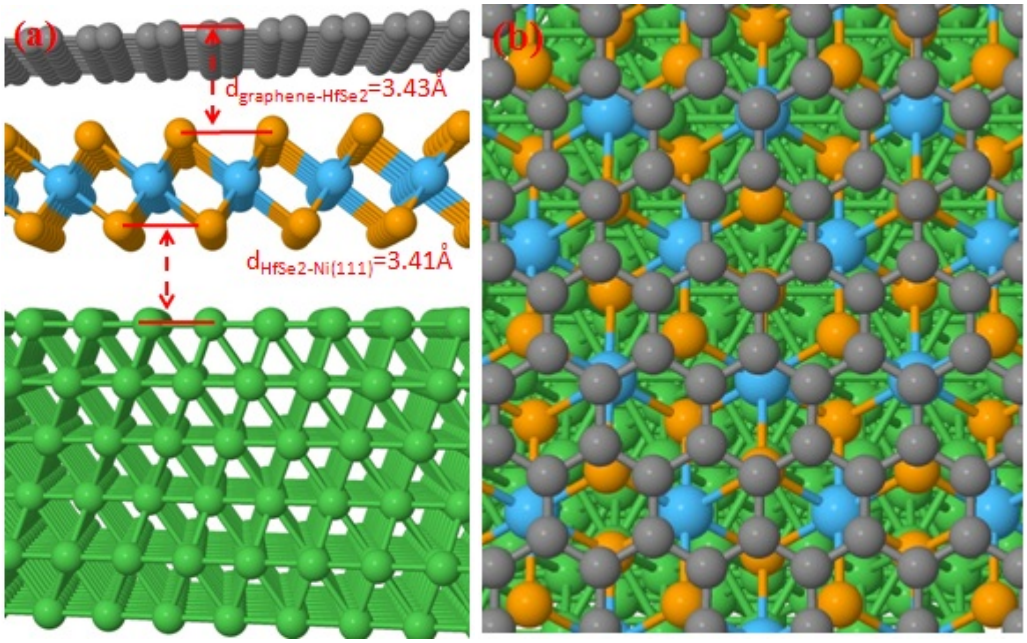

Figure 12. **(a)** Lateral view of the graphene/$HfSe_2$/Ni(111) supercell and **(b)** the top view of the supercell.

Spin-polarized calculations were performed to obtain the electronic properties correctly. As we can see in **Figure 13**, even without Ni(111), graphene seems to be perturbed by the presence of the dielectric. This would probably be due to the small energy gap of HfSe2, 1.1 eV.

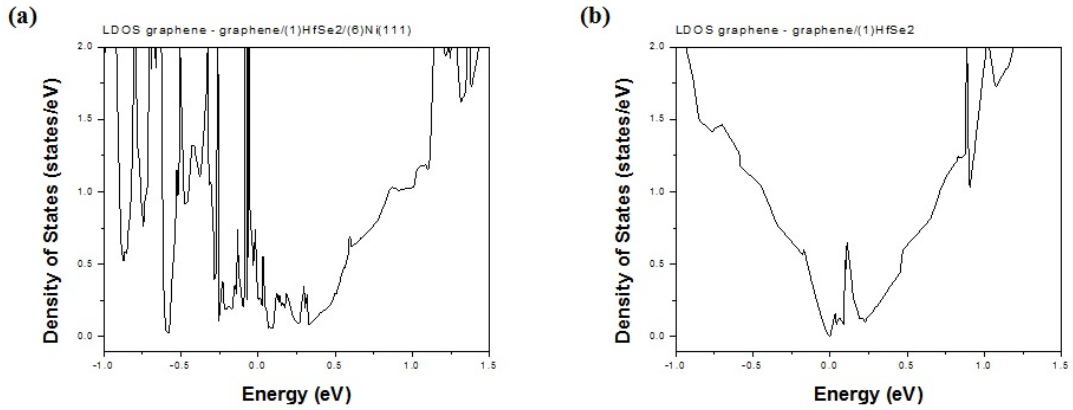

Figure 13. Graphene LDOS of the system **(a)** without Ni and **(b)** with Ni, with one layer of $HfSe_2$.

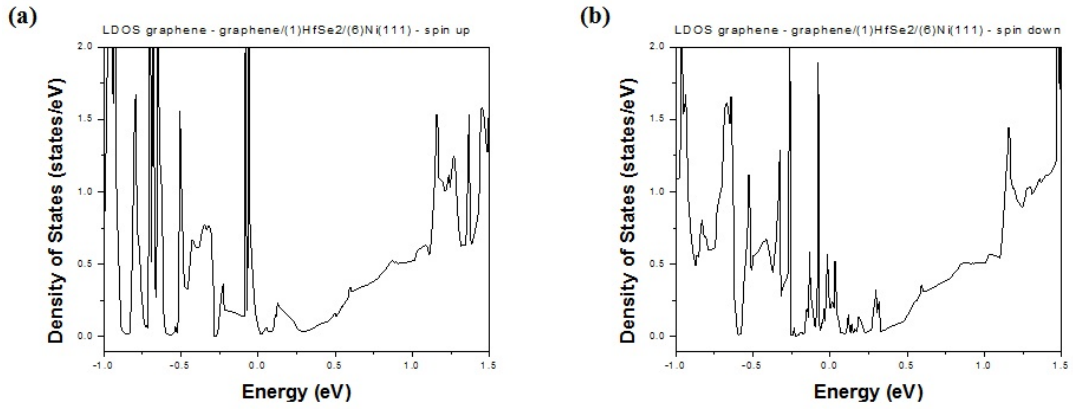

Figure 14. Graphene LDOS. **(a)** Spin up and **(b)** spin down projections for the total system with only one layer of $HfSe_2$.

5.3.4 Graphene on $MoSe_2/TaSe_2$.

Another interesting system to be studied is Graphene on $MoSe_2/TaSe_2$ and since $TaSe_2$ is a metallic TMD all the materials involved in this system are 2D materials. Since $MoSe_2$ has a lattice constant of 3.29 Å [**23**] and $TaSe_2$ of 3.43 Å [**24**] a supercell was needed to carry out the calculations and reduce the lattice mismatch between the layers. Therefore we used a 4x4 graphene supercell, a 3x3 $MoSe_2$ supercell and a 3x3 $TaSe_2$ supercell.

All of the calculations were performed using an energy cutoff of 350 eV and a 27x27x1 k-points grid. A vacuum slab of 28 Å was used in order to avoid the interaction originating from the periodic conditions.

Due to the mismatch between the different materials and the consequent use of supercells to simulate the system, all possible relative positions of carbon atoms on $MoSe_2$ are

covered. Thus, as in the case of graphene on h-AlN, any position is almost equally stable to the others. However, for the interface $MoSe_2/TaSe_2$ since it is used the same supercell for both of them, it is possible to define a preferable position. As it is shown in **Figure 15(a)**, it was found that $MoSe_2$ prefers to lay on $TaSe_2$ with a 2H structure which means that the Ta atom of a $TaSe_2$ unit cell have the same (x,y) coordinates with the Se atoms of the $MoSe_2$ unit cell. Similarly, the Mo atom of the $MoSe_2$ unit cell have the same (x,y) coordinates with the Se atoms of the $TaSe_2$ unit cell. The equilibrium distance between $TaSe_2$ and $MoSe_2$ was found at 3.01 Å while the distance between $MoSe_2$ and graphene was found at 3.5 Å.

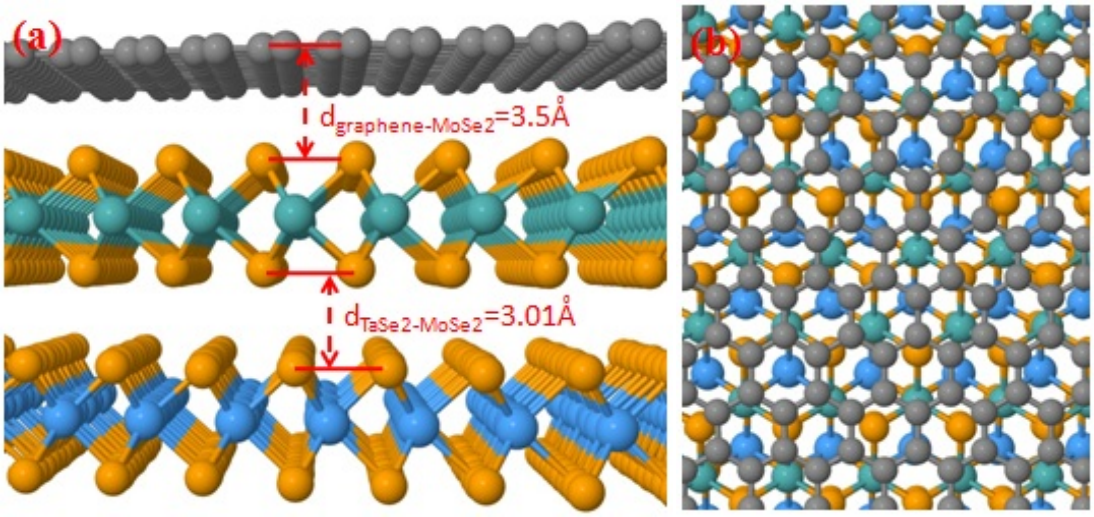

Figure 15. **(a)** Lateral view of the graphene/$MoSe_2/TaSe_2$ supercell and **(b)** the top view of the supercell.

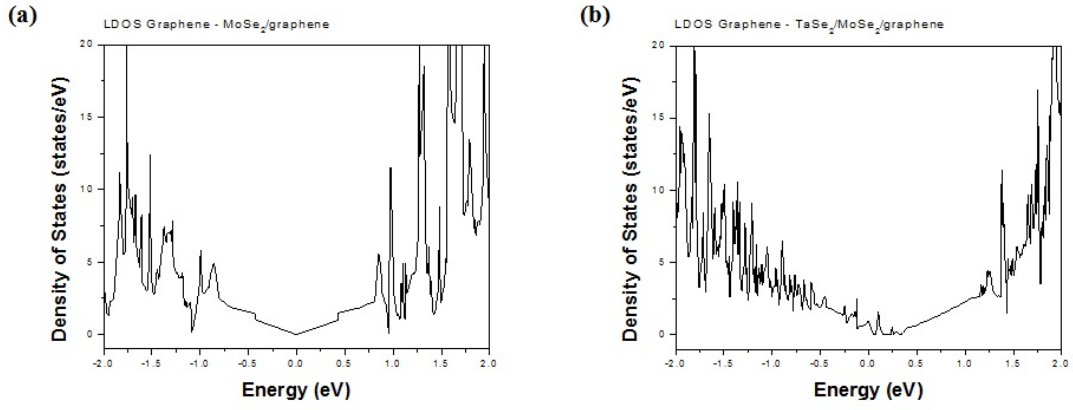

Figure 16. Graphene LDOS of the system **(a)** graphene/$MoSe_2$ without $TaSe_2$ and **(b)** with $TaSe_2$, both with one layer of $MoSe_2$.

Like in the previous cases we expected the graphene LDOS to be more similar to the graphene freestanding DOS as the number of layers of the dielectric is increased.

5.3.5 Band structure calculations. DFT calculations vs. ARPES measurements.

DFT calculations can be helpful to understand experimental results from ARPES measurements. The experimental ARPES image can be compared with band structures calculated by DFT in order to clarify the results.

$TaSe_2$ is a TMD that can be grown in different polytypes. **Figure 17** shows the structure of the two most common, the 2H and the 1T. The band structure calculations for both polytypes are shown in **Figure 18**. The $TaSe_2$ sample, which was grown in our MBE chamber [**8**], was characterized by ARPES method (see **Figure 18**). Comparing both results, it is seen that ARPES measurements reveal metallic bands which are in agreement with our DFT calculations assuming a stable 2H trigonal prismatic phase. A broad band attributed to Ta 5d orbitals [**24**] is seen to cross the Fermi level in the experimental valence band spectra. Immediately below this band exist bands due to the Se 4p contributions [**24**]. As seen in **Figure 18(c)**, for 1T-$TaSe_2$ the Se 4p orbital is predicted to disperse linearly very close to the Ta 5d orbitals crossing at the Γ-point near the Fermi level. In our experimental data, the Se and Ta orbitals are well separated, which is in agreement with the theoretical calculations of the 2H-$TaSe_2$ phase.

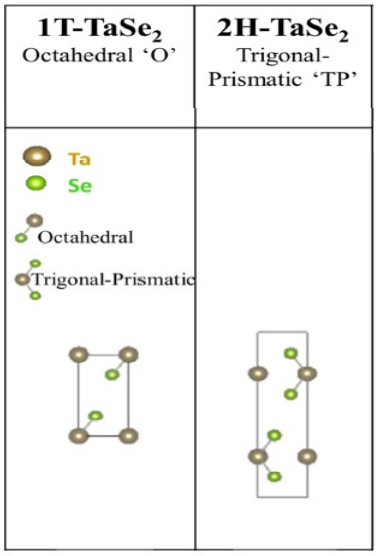

Figure 17. The Se-Ta-Se coordination is pure trigonal prismatic and pure octahedral in the 2H and 1T structures.

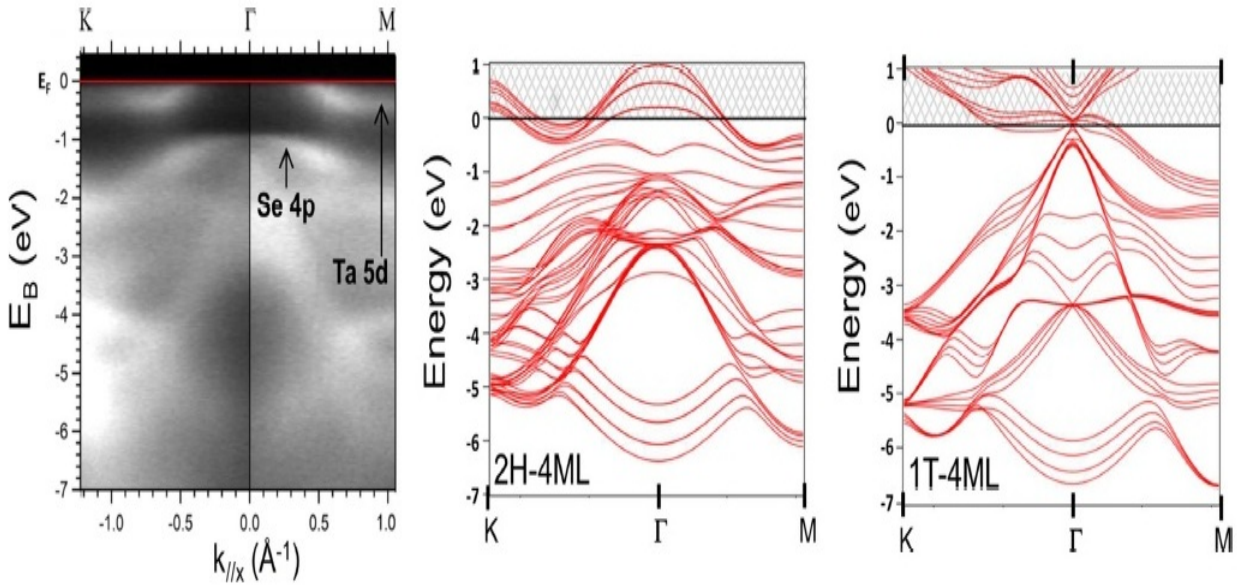

Figure 18. Band structure imaging by in-situ ARPES of 4 ML-$TaSe_2$/AlN (top) and DFT bandstructure calculations for 2H (middle) and 1T (bottom) $TaSe_2$ phases. Experimental data agree with the formation of the trigonal prismatic 2H-$TaSe_2$ phase.

Other examples are the 3ML $ZrSe_2$ [**9**] and the 6ML $HfSe_2$ grown on AlN [**10**]. In both cases, the electronic bands were well-predicted by DFT calculations as we can see at the following figures:

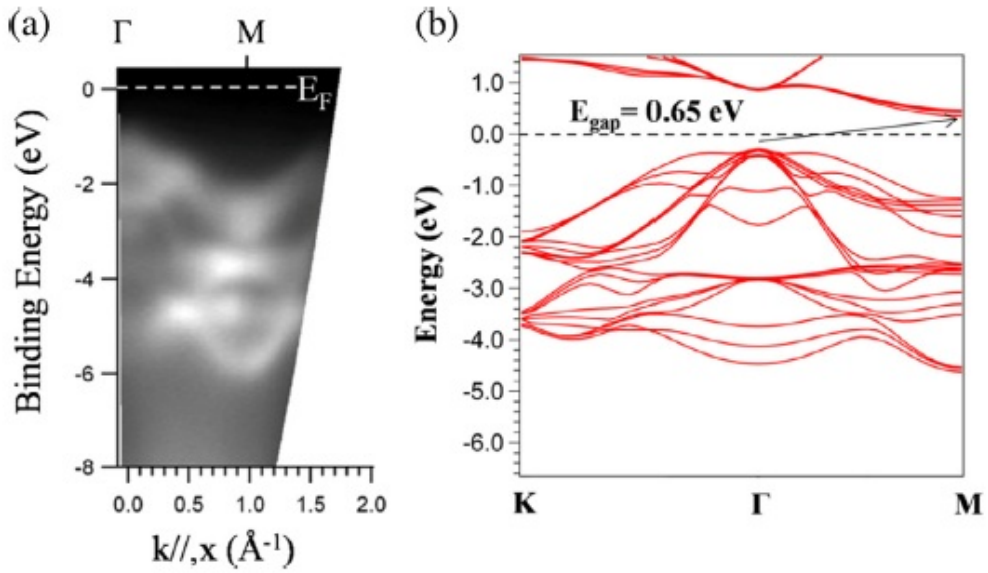

Figure 19. (a) Electronic band structure ARPES imaging of 3 ML $ZrSe_2$ along the CM direction of the surface Brillouin zone. (b) DFT band structure for a 3 ML $ZrSe_2$ film. VB maximum is at C point and CB minimum at M point yielding an indirect gap of 0.65 eV as indicated by the arrow. Dashed line is the E_F.

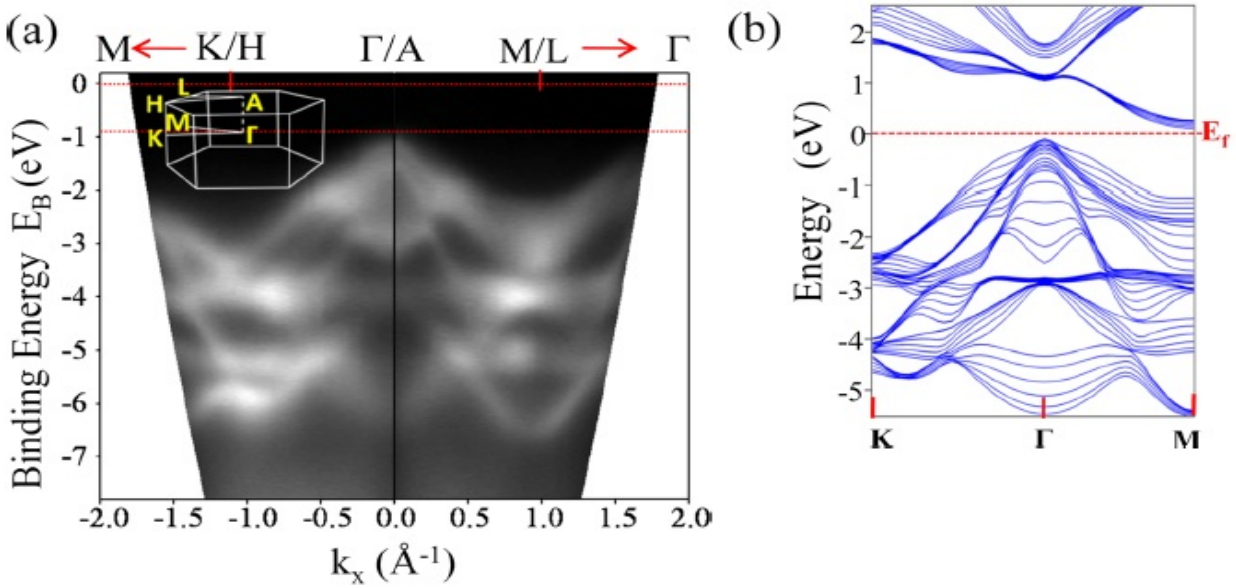

Figure 20. ARPES valence band imaging using He I excitation of 21.22 eV along the high symmetry directions K/H-C/A-M/L of the Brillouin zone for a 6 ML $HfSe_2$/AlN sample. (b) DFT band structure calculations of 6 ML HfSe2 free-standing slab with spin orbit coupling.

5.4 Conclusions

This study concluded that graphene is stable on different dielectrics such as h-AlN, h-BN, $MoSe_2$ or $HfSe_2$. The presence of different metals such as Ag(111), Ni(111) or $TaSe_2$ can clearly affect the electronic properties of graphene when a layer of these dielectrics is present.

Depending on the dielectric and the metal substrate the disruption of the LDOS of graphene is more pronounced. As it has been shown previously in the chapter, the dielectric with larger energy gaps: h-AlN, h-BN and $MoSe_2$ have no effect on the LDOS of graphene as expected, while the dielectric with smaller energy gap like $HfSe_2$, introduce some alterations in the LDOS. Additionally, it was shown that Ag(111) alters more significantly the LDOS of graphene than Ni(111) or $TaSe_2$. In any case, a decrease or suppression of such effects is expected whilst increasing the width of the dielectric layer.

Additionally, it has been demonstrated that DFT calculation can be useful in order to support experimental data from ARPES measurements of different 2D-TMD such as $TaSe_2$, $ZrSe_2$ and $HfSe_2$.

References

[1] R.M. Martin, Electronic Structure, Cambridge (2004)
[2] S. V. Eremeev, I. A. Nechaev, P. M. Echenique and E. V. Chulkov, Scientific Report 4, 6900 (2014)
[3] P. Lee, K.-H. Jin, S.J. Sung, J.G. Kim, M-T. Ryu, H-M. Park, S-H Jhi, N. Kim, Y. Kim, S. U. Yu, K. S. Kim, D. Y. Noh and J. Chung, ACS Nano, 9 (11), 10861–10866 (2015)
[4] S. Cahangirov, M. Audiffred, P. Tang, A. Iacomino, W. Duan, G. Merino and A. Rubio, PRB, 88, 035432 (2013)
[5] T. Heine, Acc. Chem. Res., 48 (1), pp 65–72 (2015)
[6] H. Zhang, C-X. Liu, X-L. Qi, X. Dai, Z. Fang and S-C. Zhang, Nature Physics 5, 438 - 442 (2009)
[7] S.-M. Huang, S.-Y. Xu, I. Belopolski, C.-C. Lee, G. Chang, B.K. Wang, N. Alidoust, G. Bian, M. Neupane, C. Zhang, S. Jia, A. Bansil, H. Lin and M. Z. Hasan, Nature Comm. 6, 7373 (2015)
[8] D. Tsoutsou, K. E. Aretouli, P. Tsipas, J. Marquez-Velasco, E. Xenogiannopoulou, N. Kelaidis, S. A. Giamini, and A. Dimoulas, ACS Appl. Mater. Interfaces, 8 (3), pp 1836–1841 (2016)
[9] P. Tsipas, D. Tsoutsou, J. Marquez-Velasco, K.E. Aretouli, E. Xenogiannopoulou, E. Vassalou, G. Kordas, A. Dimoulas, Microelectronic Engineering 147 269–272 (2015)
[10] K. E. Aretouli, P. Tsipas, D. Tsoutsou, J. Marquez-Velasco, E. Xenogiannopoulou, S. A. Giamini, E. Vassalou, N. Kelaidis, and A. Dimoulas, APL, 106, 143105 (2015)
[11] G. Kresse and J. Hafner, Phys. Rev. B 47, 558 (1993).
[12] G. Kresse and J. Furthmuller, Phys. Rev. B 54, 11169 (1996).
[13] J. P. Perdew, K. Burke and M. Ernzerhof, Phys. Rev. Lett. 78, 1396 (1997).
[14] J. P. Perdew and A. Zunger, Phys. Rev. B, 23, 5048, 1981.
[15] J. Harl, L. Schimka and G. Kresse, Phys. Rev. B 81, 115126 (2010).
[16] H. J. Monkhorst and J. D. Pack, Phys. Rev. B 13, 5188 (1976).
[17] E.F. de Almeida Junior, F. de Brito Mota, C.M.C. de Castilho, A. Kalanakova-Georgieva and G.K. Gueorguiev, Eur. Phys. J. B 85, 48 (2012)
[18] D. Wu, M. G. Lagally and F. Liu, PRL 107, 236101 (2011)
[19] C. Bacaksiz, H. Sahin, H. D. Ozaydin, S. Horzum, R. T. Senger, and F. M. Peeters, Phys. Rev. B 91, 085430 (2015)
[20] R. Koitz, A. P. Seitsonen, Iannuzzi and J. Hutter, Nanoscale, 5, 5589-5595 (2013)
[21] Jordan, L., and W. H. Swanger, J. Res. Nat. Bur. Stds. vol. 5 pp. 1291–1307 (1930)
[22] A. H. Reshak , S. Auluck, Physica B 363 (2005) 25–31
[23] Xenogiannopoulou, E.; Tsipas, P.; Aretouli, K. E.; Tsoutsou, D.; Giamini, S. A.;Bazioti, C.; Dimitrakopulos, G.P.; Komninou, Ph.; Brems, S.; Huyghebaert, C.; Radu, I. P., Nanoscale 2015, 7, 7896-7905.

[24] Sharma, S.; Auluck, S.; Khan, M. A. Optical Properties of 1T and 2H Phases of TaS2 and TaSe2. Pramana Journal of Physics 2000, 54, 431-440.

Chapter 6

Conclusions

The reach of all the useful conclusions deriving from the experimental and theoretical study of graphene and its interaction with other 2D materials, in order for them to be used together in the conduction of novel electronic devices, has been the common theme behind the results presented in this thesis. Four aspects were further examined in the course to achieve this purpose. The results for each of these aspects are summarized at the end of Chapters 3-5, of which a few key results will be highlighted once again.

Graphene growth by Chemical Vapor Deposition (CVD)

Large areas of single layer graphene can be achieved by reducing the duration of the second growth step of the procedure down to 2 minutes, along with the concurrent increase of the temperature of the annealing step, while maintaining the optimum atmospheric conditions which were specified previously to the optimization of the growth duration and are described in Chapter 3.

Few layer/ Single layer graphene growth on Ni from multilayer by etching

Graphene can be etched by annealing in a H_2/Ar atmosphere at a low temperature (T=450°C) resulting in a few layer or single layer material, without defects. The proposed method could be used for post-growth control on the number of layers while graphene is still on the metal catalyst, in this case Ni, by etching a thicker MLG which is typically obtained by CVD on Ni. Our method, which is a relatively low-temperature procedure, could be combined with growth processes at low temperatures as well and be compatible with further use of the graphene in a possible multi-step process with a low thermal budget.

Furthermore, in Chapter 3 it is shown that the top layers of the final material are arranged in an AB stacking order while the bottom layers close to the interface with Ni are grown in a random orientation with respect to each other, probably due to the out-diffusion of less energetic carbon atoms during the cooling down step.

Non AB-stacked graphene characterization

Graphene essentially grows polycrystalline with 2 preferential rotational domains, when it is grown on Cu(111) by CVD. These results were obtained when the electronic valence band structure of three layer CVD graphene on single crystal Cu(111) has been imaged by ARPES over a large area in k-space. Furthermore, three nearly perfect Dirac cones indicate that there is no interlayer interaction in such a way that the three layers behave as independent ones. More generally, our results suggest that ARPES can directly measure the number of layers, the stacking order, and the degree of interlayer interaction complementing Raman for a full characterization of FLG (Chapter 3).

Metal Insulator Semiconductor (MIS) Devices with Encapsulated Graphene in the Gate

MIS capacitors of Si p-and n-type were developed through the encapsulation of single layer graphene into the capacitor's structure, while the possible influence of the quantum capacitance of graphene on the C-V characteristics was also explored. The capacitance enhancement peaks were measured at around 0.35-0.70V in accumulation, which reaches up to 35 % above the geometrical capacitance at room temperature. This effect is more pronounced for thin oxide films and low doped semiconductor substrates. Based on the MIS device modeling the peak enhancement is attributed to the negative quantum capacitance contributions due to exchange interaction effects in graphene (Chapter 4).

First Principle calculations

The presence of different metals such as Ag(111), Ni(111) or $TaSe_2$ can clearly affect the electronic properties of graphene when a layer of these dielectrics is present. Additionally, this study has shown that graphene is stable on different dielectrics such as h-AlN, h-BN, $MoSe_2$ or $HfSe_2$. Depending on the dielectric and the metal substrate the disruption of the LDOS of graphene is more or less deep. As it has been shown in Chapter 5, the dielectric with larger energy gaps: h-AlN, h-BN and $MoSe_2$ have almost no effect on the LDOS of graphene as expected, while the dielectric with smaller energy gap like $HfSe_2$, introduce some changes in the LDOS. Furthermore, it was shown that Ag(111) modifies more significantly the LDOS of graphene than Ni(111) or $TaSe_2$. In any case, a decrease or suppression of such effects is expected whilst increasing the width of the dielectric layer. Moreover, it has been demonstrated that DFT calculation can be useful in order to support experimental data from ARPES measurements of different 2D-TMD such as $TaSe_2$, $ZrSe_2$ and $HfSe_2$.

Publications

1) “Electronic band structure imagining of three layer twisted graphene on single cristal Cu(111)” J. Marquez-Velasco, N. Kelaidis, E. Xenogiannopoulou, Y. S. Raptis, D. Tsoutsou, P. Tsipas, Th. Speliotis, G. Pilatos, V. Likodimos, P. Falaras, A. Dimoulas. APL 103, 213108 (2013)
2) “Reducing the layer number of AB stacked multilayer graphene grown on nickel by annealing at low temperature” J. Marquez-Velasco, S.A. Giamini, N. Kelaidis, P. Tsipas, D. Tsoutsou, G. Kordas, Y.S. Raptis, N. Boukos, A. Dimoulas. Nanotechnology 26, 405603 (2015)
3) “Negative Quantum Capacitance Effects in Metal–Insulator–Semiconductor Devices with Composite Graphene-Encapsulated Gates” P. Tsipas, S.A. Giamini, J. Marquez-Velasco, N. Kelaidis, D. Tsoutsou, K.E. Aretouli, E. Xenogiannopoulou, E.K. Evangelou, A. Dimoulas, Adv. Electron. Mater., 2: 1500297 (2016)
4) “Epitaxial 2D MoSe2 (HfSe2) Semiconductor/2D TaSe2 Metal van der Waals Heterostructure” D. Tsoutsou, K.E. Aretouli, P. Tsipas, J. Marquez-Velasco, E. Xenogiannopoulou, N. Kelaidis, S.A. Giamini, A. Dimoulas. ACS Appl. Mater. Interfaces, 8 (3), pp 1836–1841(2016)
5) “Epitaxial ZrSe2/MoSe2 semiconductor v.d. Waals heterostructures on wide band gap AlN substrates” P.Tsipas, D. Tsoutsou, J. Marquez-Velasco, K.E. Aretouli, E. Xenogiannopoulou, E. Vassalou, G. Kordas, A. Dimoulas. Microelectronic Engineering 147, 269-272 (2015)
6) “Two-dimensional semiconductor HfSe2 and MoSe2/HfSe2 van der Waals heterostructures by molecular beam epitaxy” K.E. Aretouli, P. Tsipas, D. Tsoutsou, J. Marquez-Velasco, E. Xenogiannopoulou, S.A. Giamini, E. Vassalou, N. Kelaidis, A. Dimoulas. APL 106, 143105 (2015)
7) “Experimental investigation of metallic thin film modification of nickel substrates for chemical vapor deposition growth of single layer graphene at low temperature” S.A. Giamini, J. Marquez-Velascoa, I. Sakellis, P. Tsipas, N. Kelaidis, D. Tsoutsou, N. Boukos, V. Kantarelou, E. Xenogiannopoulou, Th. Speliotis, K. Aretouli, G. Kordas, A. Dimoulas, App. Surf. Sci. 385, 554–561 (2016)
8) “AB stacked few layer graphene growth by chemical vapor depositionon single crystal Rh(1 1 1) and electronic structure characterization” A. Kordatos, N. Kelaidisa, S. A. Giamini,J. Marquez-Velasco, E. Xenogiannopoulou, P. Tsipas,G. Kordas, A. Dimoulas, App. Surf. Sci. 369, 251-256 (2016)
9) “Evidence for Germanene growth on epitaxial hexagonal (h)-AlN on Ag(111) ” by F. D'Acapito, S. Torre, E. Xenogiannopoulou, P. Tsipas, J. Marquez-Velasco, D. Tsoutsou, A. Dimoulas, J. Phys.: Condens. Matter 28, 045002 (2016)